# NUMERICAL SIMULATIONS AND LOW-ORDER MODELS OF THE TWO-WAY INTERACTION BETWEEN OCEAN CURRENT TURBINES AND THE BACKGROUND FLOW

by

Peyman Razi

A dissertation submitted to the faculty of
The University of North Carolina at Charlotte
in partial fulfillment of the requirements
for the degree of Doctor of Philosophy in
Mechanical Engineering

Charlotte

2021

Approved by:

_____
Dr. Praveen Ramaprabhu


_____
Dr. Michael Muglia


_____
Dr. Russell Keanini


_____
Dr. Matthew Whelan

ABSTRACT

PEYMAN RAZI. Numerical Simulations and Low-Order Models of the Two-Way Interaction between Ocean Current Turbines and the Background Flow. (Under the direction of DR. PRAVEEN RAMAPRABHU)

Ocean Current Turbines (OCTs), which function similarly to wind and tidal turbines, represent a promising technology for harnessing the energy from oceanic currents such as the Gulf Stream. In planning the deployment of arrays of OCT devices, it is critical to consider the two-way interactions between the turbines and the ocean environment: temporally and spatially nonuniform flow fields are expected in the dynamic flow environments of western boundary currents, and include the presence of upstream shear and turbulence. These nonuniform flow conditions will affect power extraction, and the efficiency of the turbines when operating in isolation or as part of an array. Furthermore, models that are used in a predictive capability to compute the levelized cost of energy obtainable from such devices, or to optimize the layout of an array of turbines must be modified to account for the effects of such spatially and temporally inhomogeneous conditions. Similarly, the operation of OCT arrays can in turn influence the background flow in two significant ways, namely by contributing to the production of turbulence and through the generation of internal gravity waves that are radiated away from the point of origin. In this thesis, we have studied using detailed numerical simulations, the above two-way interaction between arrays of OCTs and the ocean environment. Insights developed from the simulations have guided the development of low-order wake interaction models capable of describing the effects of inhomogeneous flow conditions on array performance.

A new, wake interaction modeling framework capable of capturing the detailed effects of turbulence and upstream shear on various performance parameters associated with OCTs arranged in any arbitrary configuration has been developed. The model accounts for the effects of turbulence and shear on the structure of the turbine wakes, specifically the extents of near- and far-wake regions. The analytical description for turbine wake is combined with an existing wake interaction model, the Unrestricted Wind Farm Layout Optimization model to predict the global power output from an array of OCTs. The resulting modelling framework accurately captures the effect of inlet turbulence and shear on the OCT farm power and efficiency, and can be applied to any array configuration. Results from the model were validated against both Large Eddy Simulations and Reynolds Averaged Navier-Stokes simulations, in which the OCTs were modeled using a Blade Element Momentum model. The dispersion of OCT wake turbulence through the background stratification of the ocean was investigated using Large Eddy Simulations for different levels of the density stratification. The effects of varying the strength of the stratification as well as the turbulent forcing were studied. Finally, the wake turbulence associated with OCT operation can drive the formation and radiation of internal gravity waves in the density-stratified background flow of ocean currents. Through detailed numerical simulations, the effect of the propagation of the internal waves on the background turbulent diffusivity was studied, and found to alter the transport properties of the ambient flow. The properties of the internal wave field, and its impact on background turbulent mixing was found to depend both on the Richardson number and the ambient, upstream turbulence.

ACKNOWLEDGMENTS

TABLE OF CONTENTS

LIST OF FIGURES

LIST OF TABLES

CHAPTER 1: INTRODUCTION

The use of renewable sources of energy has increased in the last several decades, coincident with an increasing societal awareness of environmental issues. As more renewable sources of energy are brought online, reducing the Levelized Cost of Energy (LCOE) is a significant consideration in the large-scale deployment of such alternate sources. While terrestrial and offshore wind farms have reached levels of technological maturity that enable their large-scale adoption, extracting energy from marine hydrokinetic devices (MHK) deployed in ocean currents is still in its infancy. This is despite the fact that wind turbines and OCTs operate at comparable levels of power density, while the longevity of tidal energy equipment is almost four times greater than other renewable energy resources such as wind or solar power [1]. Furthermore, OCTs in western boundary currents such as the gulf stream (GS) [2] will operate under velocity conditions that are predictable, and can be modeled using ocean circulation models [2].

The GS represents a perennial energy source with reliable current speeds ranging from 1.5 – 3 m/s, and has been estimated in recent studies [2, 3] to transport upwards of 70 GW of power. OCTs have been proposed [2, 4] as an efficient means to extract energy from western boundary currents like the GS, becoming a component in the global trend towards a renewable energy portfolio. For instance, Bane et al. [2] discussed the economic feasibility of deploying OCTs in the GS and other western boundary currents, based on a census of ocean circulation models. It was shown that the power density in the GS could reach $500 – 1000 \text{ W/m}^2$, but the location of peak power densities was susceptible to higher-frequency meanders and lower-frequency GS path shifts. To evaluate the feasibility of

deploying such MHK devices for operation in the GS current, and to aid in the design and optimization of arrays of OCTs [5, 6], low-order models that accurately describe single-turbine wake dynamics and wake interactions between multiple devices are necessary.

In this dissertation, we have investigated the two-way interaction between OCTs and the background flow of the ocean environment. We classify these interactions into the (i) effect of flow conditions on OCT performance and (ii) the corresponding impact of OCT wakes on the background flow. Through extensive and detailed simulations and by developing theoretical models, we have characterized the nature of these interactions. Insights from these models can be used in planning and developing deployment strategies for OCTs, and in estimating their potential environmental impact. In the following sections, we briefly introduce and discuss the four topics studied in this dissertation: (i) Effect of ambient turbulence on OCT wake development and performance; (ii) OCT performance under spatially non-uniform flow conditions; (iii) Evolution of OCT wakes through the turbulent background stratification; and (iv) internal wave generation from OCT operation.

## 1.1 Background

### 1.1.1. Effect of ambient turbulence on OCT wake development and performance

While OCT operation principles are broadly similar to wind turbines and based on Betz law, certain key differences in the operating environment, and farm layout must be considered. Compared to wind turbines, OCTs generally operate in a lower turbulence environment [7, 8], which impacts the observed wake structure. At the lower levels of turbulence intensity in the marine environment, the recovery of the wake of a single-turbine is delayed by the lower entrainment and turbulent diffusion, so that near-wake effects can no longer be ignored. Simultaneously, downstream turbines operating in the turbulent

wakes of upstream devices are likely to operate in a high turbulence environment, and are expected to recover faster. Thus, wake interaction models for OCTs must be capable of capturing both these limits, and account for the complex wake behaviors in the intervening parameter space. Similarly, turbines in offshore wind farms are exposed to lower levels of turbulence intensities as observed in [9] and [10], which could extend the near-wake region. Near-wake effects are also significant in co-axial turbine designs under consideration [11], in which counter-rotating turbines are employed to create a device with nearly net zero torque to avoid twisting of the turbine tethers [12]. Surface roughness and boundary layer effects, which are significant considerations in wind turbine siting, are less significant in OCT operation, which will likely be moored in the deep waters using tethers. The tethered configuration [13, 14] will allow for placement of OCT turbines in a farm layout [2, 15] in which the turbines are staggered in all three dimensions, responsive to optimization around the total farm power as the objective function.

While Computational Fluid Dynamics (CFD) simulations [15] have led to significant insights into the behavior of wind turbines and MHK devices, the computational workload is prohibitive for large arrays of turbines or extensive parametric studies [6]. In particular, tethered OCT deployment in the GS or other western boundary currents [4] may rely on active, real-time repositioning based on optimization strategies [5, 6] to account for varying properties of the free-stream or the meander of the current [4]. In such scenarios, efficient and reliable low-order wake interaction models that account for the unique wake characteristics of OCTs including the persistence of the near-wake regions, are required to ensure fast convergence of the coupled layout optimization techniques [5]. Several wake models originally developed for wind turbines are valid in the limit of vanishing near-wake

regions, and hence cannot be applied to the OCT application. In this work, we propose a wake turbulence model that describes OCT wake properties over a wide range of turbulence intensities in the incoming flow, and the corresponding variations in wake structures. This single-turbine wake model is then implemented in a recently published [16] modeling framework for wake interaction effects that will be present in a dense OCT farm layout. Both the single-turbine model and the wake interaction model for multiple turbines are validated using detailed three-dimensional, Large Eddy Simulation (LES) with a commercial CFD solver.

*1.1.2. OCT performance under spatially non-uniform flow conditions*

Unlike wind turbines which operate in the strong-shear environment of the lower atmospheric boundary layer, tethered OCTs will in general, experience low shear conditions associated with the background, oceanic flow. For typical values of freestream mean velocities ($\sim 1 - 2$ m/s) and turbine diameters of $\sim$ 50m, the strength of the local shear rate $\gamma \equiv \frac{\partial U}{\partial y}$ ($s^{-1}$) can be quantified in terms of the non-dimensional parameter $\gamma \frac{D_t}{U}$, where $D_t$ is the turbine rotor diameter and $U$ is the mean flow velocity. We expect OCTs to operate under conditions satisfying $\gamma \frac{D_t}{U} \ll 1$, indicating a low-shear environment. While this is generally true, due to the meander of the GS currents, turbines could be exposed to strong shear conditions locally, and over short periods of time.

In addition, when multiple devices are deployed constituting an 'OCT farm', individual turbines will be trapped in the wakes of their immediate neighbors, which are characterized by strong velocity gradients. Similarly, offshore wind turbines will experience strong shear conditions, since they are embedded in the 'near-wall' region of the atmospheric boundary layer. Thus, a modeling framework to estimate the dependence of turbine performance on

shear in the upstream flow is required, before evaluating the economic feasibility of OCT operation and power extraction. We have modified the low-order model of [16], developed for shear effects on wind turbine performance, to account for wake interaction of multiple OCTs operating in a spatially non-uniform flow environment. Our model has been validated using Reynolds-Averaged Navier-Stokes (RANS) simulations, and is applicable to both the weak and strong shear regimes.

*1.1.3. Evolution of OCT wakes through the turbulent background stratification*

Understanding the potential footprint of wake turbulence is critical in estimating the environmental impact of large-scale arrays of OCTs. From a detailed energy balance in which turbines were modeled as drag elements, it was estimated [2, 3] in a recent survey, that large-scale deployment of OCTs would result in significant energy dissipation up to several gigawatts, thereby potentially affecting the resource. However, the interaction between the turbine elements and the background resource is complicated by several factors, including the details of the background stratification and shear flow, and the locations and numbers of turbines. For instance, turbines deployed in the surface boundary layer would operate in a region of the ocean that is well mixed by wind shear stress as well as diurnal surface temperature variations. In addition, internal waves have been observed in the current velocity field from vessel transects  and glider current measurements [17] that significantly enhance shear in at least the upper 200 m of the water column. The temporal persistence of these internal waves has not been quantified, but consideration for their influence on the shear and mixing of stratification will be necessary. In contrast, the maximum current speeds exist in the upper 100m of the water column, often referred to as

the GS jet. Shear in the jet region is often lower than that beneath it, and within the cyclonic and anticyclonic shear zones.

The local competition between the shear flow and density stratification determines the stability of the background flow to large perturbations in the form of turbulence created by OCTs. This competition is captured by the gradient $Ri$ number,

$$Ri \equiv \frac{N^2}{\left(\frac{dU}{dy}\right)^2 + \left(\frac{dV}{dy}\right)^2} \tag{1.1}$$

where $N^2 = -\frac{g}{\rho}\frac{d\rho}{dy}$, is the buoyancy frequency, $\frac{d\rho}{dy}$ is the density gradient in the direction of ocean depth, and $\frac{dU}{dy}$ and $\frac{dV}{dy}$ represent the shear in cross-stream and downstream velocities with depth, respectively. From linear analysis [18, 19], it was shown that $Ri > 1/4$ ensures stability of the stratified fluid to velocity perturbations; however, the consolidated wake generated by an OCT array could represent a *nonlinear* perturbation. While there have been theoretical studies suggesting the $Ri$ number cutoff should be higher [20, 21] ($Ri > 1$) for such nonlinear perturbations, there have not been detailed experimental or simulation studies to investigate this critical limit under conditions relevant to OCT operation.

While the general problem of turbulent mixing in stratified fluids has been extensively studied [22], the development of localized turbulence according to an oceanic background stratification has received relatively little attention. The authors of [20] performed a nonlinear analysis for the stability of a shear layer subjected to finite-amplitude perturbations while embedded in a background stratification. They found that in contrast to the linear case, when nonlinear perturbations are imposed, the shear layer is stable only for $Ri > 1$. Early experimental results included ADCP and Rapid Sampling Vertical Profiler

(RSVP) measurements reported in [23] at the site of the South Equatorial Current (SEC). These measurements included vertical profiles of velocity (shear), salinity, temperature, and density obtained within the top 150 m of the ocean surface. The $Ri$ number computed from these measurements varied from ~0.2 near the surface to values approaching unity at depths of 150 m. The authors [23] concluded that "the quest for a simple $Ri$ parametrization of turbulent mixing is doomed because it does not address the necessary physics of the problem."

Laboratory-scale studies were reported in [24] of a mixing tank experiment in which a lighter turbulent layer was above a density stratified quiescent layer. However, the authors of [24] were focused on interfacial instabilities between the layers (and not transport within the bulk fluid), and found that Kelvin–Helmholtz instabilities at the interface were suppressed for $Ri > 1$. A similar setup was examined using Direct Numerical Simulations (DNS) in [25], and investigated the development of turbulent patches in a stratified shear layer. Vortices associated with the turbulent patches were found to be stabilized when the stratification was such that $Ri > 0.25$. There has been some ambiguity [25] in the value of the critical $Ri$ for turbulent forcing of a stratified flow. Other studies [26] have taken issue with the centrality of $Ri$ as a predictor of turbulent diffusivities, arguing that flow outcomes should also depend on the turbulent intensity. In [27], it was shown that to accurately reproduce LES data, the parameterization of the turbulent diffusivity must also include a shear length scale and the kinetic energy of the background turbulence (in addition to the background $Ri$ number). The explanation for this dependence is that while the $Ri$ number governs stability, it is the turbulent intensity that determines the overall turbulent transport, and so must be included.

Similarly, the authors of [28] suggest framing the problem in terms of separate shear and buoyancy parameters, with lines of constant $Ri$ dividing the parameter map into shear-dominated, buoyancy-dominated, and unforced regions. Progress in this area has been limited by the scarcity of high-resolution data from the GS. We have performed detailed LES to investigate the growth of locally generated turbulence, through a stratification field similar to the conditions present in the ocean. To accomplish this, a new unit problem was first defined in which the density and velocity profiles are such that the Richardson number is constant throughout. This removes the possibility of an artificial lengthscale associated with the $Ri$ profile, that could interfere with the development of the turbulent patch. LES, in which a turbulent spot was refracted through the above stratification profile at different values of $Ri$ were performed. The spatial footprint of turbulence was measured for each case, and expressed in terms of a power law, in which the coefficients were functions of $Ri$. The power law for the turbulence footprint was then applied to actual data from the Gulf Stream [4] to provide rough estimates for the extent of turbulent spreading from OCT wakes. We have taken advantage of recent advances through the ADCP and Conductivity Temperature Depth (CTD) cast measurements by [4], across different transects of the GS (density and shear profiles), which were directly used to drive our numerical simulations.

### 1.1.4. Internal wave generation from OCT operation

Internal Gravity Waves (IGWs) are generated in the ocean, when isopycnals in a continuously stratified fluid are perturbed, so that the gravity-induced restoring forces create oscillatory motion and engender wave propagation. IGWs explain a significant portion of the energy flux budget in the ocean, while the breaking of such waves resulting in turbulent bursts is responsible for much of the observed mixing (the nutrient exchange

rate has been observed to increase by tenfold in the presence of IGWs when compared with a quiescent ocean [29]).
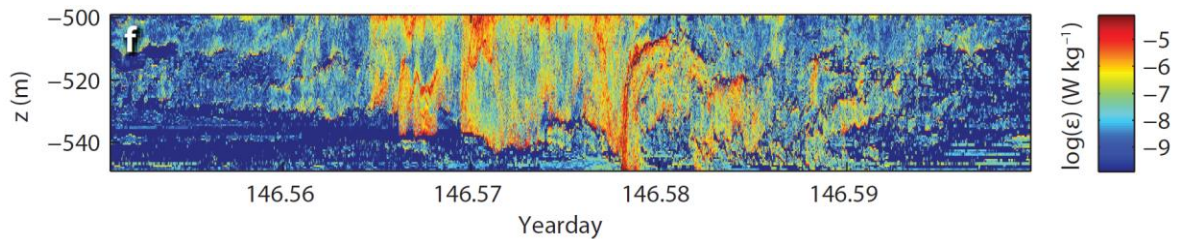


Figure 1.1: Time-depth image of the turbulent dissipation rate of a breaking internal wave [30].

Since IGWs may also be generated from artificial sources, such as ocean current turbines operating in the pycnocline, we refer to the two sources to distinguish between wave generations. Internal waves from submerged objects can be referred to as *point source waves*, since the wake of an OCT may be treated as a string of point sources generating momentum that propagates as wave motion. IGWs generated naturally in the ocean from the interaction of ocean tides with the ocean floor topography will be referred to as *internal tides* (waves generated due to sharp density gradients at the ocean surface are not considered since their propagation is restricted to the horizontal plane). Point source waves may then interact with the (longer wavelength) internal tides, resulting in the premature breakup of the latter objects through nonlinear triadic interactions [29]. The implications for such a scenario could be wide ranging and include modifications to the large-scale transport of nutrients in the ocean.

Point sources such as OCTs generate internal waves through three distinct mechanisms [31-33]. Internal waves generated as a result of flow deformation around the shape of an object are Lee waves, and deterministic in nature. The rotation of turbine blades will result in swirling wake flow, characterized by helical vortices that lead to formation of transient

waves that are expected to be short-lived. Finally, the turbulent wake behind OCTs will collapse under the influence of the stable background stratification, resulting in the formation of gravity waves from the 'bubble collapse' event. Such waves are random and bear the broad, spectral signature of the turbulent wake, and hence cannot be predicted using linear wave theories, and are the subject of our numerical investigation.

Previous studies of towed objects in stratified flows [31-33] have shown that Lee waves dominate when $Fr < 2.5 - 4$, and the random, turbulent, wake-induced waves dominate for $Fr \geq 4$, where the Froude number (the ratio of the buoyancy time scale to the turbulence time scale) is defined as $Fr = \frac{U_0}{NR_t}$ with $U_0$, $N$, and $R_t$ representing the mean flow velocity, buoyancy frequency, and radius of the turbine, respectively. Assuming typical values for the buoyancy frequency from recent observational measurements in the GS [4], $U_0 \sim 1$ m/s and $R_t \sim 25$ m, the $Fr$ number for typical conditions of operation may be estimated as $Fr \geq 4.5$. Thus, internal wave generation from OCTs is expected to be dominated by random waves that cannot be addressed by linear wave theory, and will require detailed numerical simulations.

Waves from OCTs will influence energy extraction and the ocean ecosystem in three ways:

(1) *Energy extraction:* Internal waves radiating upstream from the collapsed wakes of OCTs may adversely influence energy extraction by decelerating the mean flow. Such an effect has been observed in wind farms [34, 35], and has been estimated to be significant. In wind turbine farms, unfavorable pressure gradients associated with the gravity waves have been shown to result in a deceleration (and deviation) of the upstream flow, along with a corresponding decrease in total farm efficiency by 18% [34, 35]. The deployment of tethered OCTs (as proposed in [5, 36]) in the ocean must

consider the potential for internal wave generation that may negatively impact the energy extraction efficiency.

(2) *Interactions with internal tides:* Point source waves from OCTs may interact with the background internal tides through nonlinear wave–wave interactions called *triadic interactions*. A scenario where two short-wavelength waves (from the OCTs) interact nonlinearly with a long-wavelength internal tide will result in the redistribution of energy among the wavenumbers in the triad. The corresponding induced diffusion of energy among the wavenumbers will have the potential to cause internal tides to break prematurely, thereby affecting the turbulent mixing in the photic zone.

(3) *Turbulent diffusivity and mixing:* When the amplitudes of the point source waves reach a threshold value, the waves will break in a highly turbulent process. The strength of the resulting turbulent diffusivity will depend on the amplitudes of the waves, and the nature of the instability processes that trigger the wave breaking. The breaking of point source waves may result in significant modification to the ocean's turbulent diffusivity and mixing efficiency, as well as the mean temperature and salinity profiles.

We have performed detailed LES of internal waves generated from the transport of a turbulent wake through a stratified layer. The properties of the wave field were carefully studied including the phase angle at which the IGWs propagated at different value of $Ri$. We found the IGW generation meaningfully affected the properties of the background flow, including the mean streamwise velocity, turbulent kinetic energy, and other turbulent correlations. The IGWs were also found to decrease the mean velocity, thus potentially impacting energy extraction by downstream turbines.

The rest of the dissertation is organized as follows: In Chapter 2, we propose a low-order model for the structure of OCT wakes at different turbulence intensities. The model is combined with an Unrestricted Wind Farm Layout Optimization (UWFLO) model to predict the total power generated from an OCT farm at different turbulence intensities, while the results are validated using detailed companion simulations. In Chapter 3, a similar approach is taken to describe the effects of spatial nonuniformities in the upstream flow (shear) on the performance of individual OCTs and OCT farms. Once again, the low-order wake interaction model for shear conditions is validated using RANS simulations. Chapter 4 includes a discussion of the evolution of localized turbulence through the background stratification. Using insights from LES, we develop power law expressions for the downstream evolution of locally generated turbulent perturbations. The expressions are valid for different $Ri$, and are applied to velocity and density measurements obtained from the GS resource [4], to develop estimates for the turbulent footprint under realistic conditions. Internal wave generation from OCT wake turbulence developing into a stratified background flow is discussed in Chapter 5. Specifically, we describe the effect of IGWs generated from an OCT wake, on both mean and fluctuating quantities associated with the background flow. Concluding thoughts are presented in Chapter 6.

CHAPTER 2: A LOW-ORDER WAKE INTERACTION MODELING FRAMEWORK
FOR THE PERFORMANCE OF OCEAN CURRENT TURBINES UNDER
TURBULENT CONDITIONS

Understanding the effects of ambient turbulence (expressed often in terms of the turbulence intensity $I_t$) is critical to the development of predictive models for the performance of OCTs. This chapter describes a new, wake interaction modeling framework capable of capturing the detailed effects of turbulence on various performance parameters associated with OCTs that may be arranged in any arbitrary configuration. The model accounts for the effects of turbulence on the structure of the turbine wakes, specifically the extents of near- and far-wake regions, and the dependence of the transition point between the two regions on $I_t$. The analytical description for turbine wake is combined with an existing wake interaction model, the UWFLO model to predict the global power output from an array of OCTs. The resulting modelling framework accurately captures the effect of inlet turbulence on the OCT farm power and efficiency, and can be applied to any array configuration. Results from the model are validated against LES in which the OCTs are modelled using the Blade Element Momentum (BEM) model, while the inlet flow is superposed with a synthetic turbulence field designed to approximate turbulence properties obtained from observational measurements of the Gulf Stream. The simulations show that OCT wakes recover faster at higher levels of inlet turbulence due to the enhanced entrainment and mixing between ambient flow and the wake, an effect that is captured by the proposed UWFLO model.

The chapter is organized as follows: In § 2.1.1, we briefly review previous models for turbine wakes, before introducing our model for both near-wake and far-wake regions in § 2.1.2. Using the wake interaction model framework for multiple turbines introduced in

[16], we extend our model to OCT farm layouts in § 2.1.3. Our simulation strategy is described in § 2.2, along with an outline of the different cases examined. Single turbine wakes are analyzed in detail in § 2.3, where we examine the role of the upstream turbulence intensity in determining the length of the near-wake region and wake growth rates. Here, we validate our wake model against simulation data and previously proposed models. Our modeling framework for multiple OCTs is validated in § 2.4 using LES data, and includes (a) two-turbine configuration, (b) staggered OCT arrangements, and (c) a square array of turbines. A summary and concluding remarks are presented in § 2.5.

## 2.1 Models for OCT wakes and array performance

### 2.1.1. Models for turbulence effects on single-turbine performance

Several analytic models have been proposed to describe the evolution of wind turbine wakes, and to account for the interactions between multiple wakes in a wind farm. The Jensen [37] wake model represents one of the earliest efforts, and describes the development of the downstream velocity field in the wake of a turbine. The model is derived from applying conservation of mass between the upstream and downstream regions, and assuming a top-hat velocity profile for the wake, while the near-wake region is neglected:

$$\frac{\Delta U}{U_0} = \frac{\left(1 - \sqrt{1 - C_T}\right)}{\left(1 + \frac{2\alpha x}{D_t}\right)^2} \tag{2.1.1}$$

In eq. (2.1.1), $U_0$ is the free-stream velocity, $\Delta U(x) \equiv U_0 - U(x)$ is the wake deficit at the streamwise location $x$, $C_T$ is the thrust coefficient of the turbine, $\alpha$ is the growth rate of the linearly expanding wake, and $D_t$ represents the diameter of the turbine. In several studies [38, 39], a linear wake assumption is coupled with a constant expansion factor $\alpha$ taken as

a function of the surface roughness (recommended values of $\alpha$ based on surface roughness from [40, 41] are 0.075 for onshore and 0.05 for offshore applications respectively). Frandsen et al. [38] proposed a wake model valid in the far wake by assuming a top-hat velocity profile and enforcing momentum conservation:

$$\frac{\Delta U}{U_0} = \frac{1}{2}\left(1 - \sqrt{1 - 2\frac{A_t}{A(x)}C_T}\right). \tag{2.1.2}$$

In the above equation, $A_t$ is the turbine swept area and $A(x)$ is the wake area at $x$. Eq. (2.1.2) is compatible with the general form of the wake expansion given by $D(x) = D_t\left(\beta^{k/2} + \alpha\frac{x}{D_t}\right)^{1/k}$ with $\beta = \frac{1}{2}\frac{1+\sqrt{1-C_T}}{\sqrt{1-C_T}}$, while the specific case of $k = 2$ was considered in [42].

The above models were derived to conserve either mass [37] or momentum [38]. To constrain both the mass and momentum fluxes, a second wake velocity parameter is required in addition to the amplitude of the peak (or the average). By assuming self-similarity in the far-wake, a Gaussian profile for the wake velocity deficit could be introduced with the width of the profile constrained to yield a particular mass flux. Bastankhah and Porte-Agel [42] took this approach and derived new analytic models by constraining mass and momentum fluxes, while assuming a Gaussian profile for the wake velocity deficit. In solving the momentum equations, viscous and pressure terms were neglected, while the width of the self-similar function was determined from matching the mass flux with that of the Frandsen model [38] to give

$$\frac{\Delta U}{U_0} = \left(1 - \sqrt{1 - \frac{C_T}{8\sigma^2}}\right)exp(-\frac{r^2}{2\sigma^2}) \tag{2.1.3}$$

where $\sigma = \frac{\alpha x}{D_t} + 0.25\sqrt{\beta}$ is a lengthscale associated with the expanding wake and $r$ is the radial coordinate. Niayifar and Porté-Agel [43] suggested the following empirical dependence of the wake growth rate on the turbulence intensity, based on LES data and valid in the range $0.065 < I_t < 0.15$:

$$\alpha = 0.38 I_t + 0.004 \tag{2.1.4}$$

Similarly, based on a wind-turbine field study, Fuertes et al. [44] recommend for the wake growth rate the expression $\alpha = 0.35 I_t$. Finally, [45] observe the above model when extended to the near-wake region can lead to the term within the square root $1 - \frac{C_T}{8\sigma^2}$ becoming negative.

The above self-similar model (referred to hereafter as the BP model) for the wake deficit given in eq. (2.1.3) may be expressed in the general form $\frac{\Delta U}{U_0} = C(x) f\left(\frac{r}{\sigma}\right)$, where $C(x) = 1 - \sqrt{1 - \frac{C_T}{8\sigma^2}}$ expresses the decay of the centerline velocity deficit, and $f$ is the similarity solution. In the lower ambient turbulence environment of the ocean, wake recovery will be delayed resulting in a finite near-wake region, which must be accounted for in low-order models for OCTs. In [45], the authors suggest a modification to $C(x)$ in the BP model to capture the effects of ambient turbulence, turbine properties through the coefficient of thrust $C_T$, and the near wake region. The modified expression for the velocity deficit function proposed by [45] is:

$$\frac{\Delta U}{U_0} = \frac{1}{\left\{a + b\left(x/D_t\right) + c\left(1 + x/D_t\right)^{-2}\right\}^2} exp\left(-\frac{r^2}{2\sigma^2}\right) \tag{2.1.5}$$

In eq. (2.1.5), the $c\left(1 + x/D_t\right)^{-2}$ term in the denominator represents the 'virtual origin' effect when the near-wake region is considered, and $(a, b, c, \alpha, \beta)$ are taken as functions of

the coefficient of thrust $C_T$ and the upstream ambient turbulence intensity $I_t$, with corresponding coefficients and exponents obtained by fitting to a suite of LES simulation data.

*2.1.2. Proposed model for turbine wake*

In this section, we propose a simple analytic formulation for the dependence of turbine wake parameters on the intensity of turbulence in the flow. Our model accounts for both near- and far-wake regions, and we have found this is important in describing the complete dependence of wake properties on turbulence for OCTs. In the far-wake, our model assumes the form of the Jensen model [37], but with the growth rate and transition location between near- and far-wake regions dependent on the turbulence intensity. The model for turbine wake dependence on turbulence is described in this sub-section, while the extension to a turbine array is presented in § 2.1.3. The turbine wake model is obtained through the following steps:

1) The diameter of the wake is taken to be a linear function of the axial coordinate in the near-wake region, and in accordance with the Jensen framework [37]:

$$D(x) = D_t + 2\alpha x \qquad (2.1.6)$$

2) From applying continuity to the near-wake region at the turbine plane (fig. 2.1) and at the plane containing the transition point $x_0$, $D_{x_0}$ the diameter of the turbine wake at $x_0$ can be obtained as a function of the induction factor $a$ [46]

$$A_t U_t = A_{x0} U_{x0} \implies (1-a)U_0 D_t{}^2 = (1-2a)U_0 D_{x0}{}^2 \qquad (2.1.7)$$

$$D_{x_0} = D_t \sqrt{\frac{1-a}{1-2a}} \qquad (2.1.8)$$

where $U_t$ is the velocity at the rotor plane and $a \equiv (U_0 - U_t)/U_0$ is the induction factor (the above standard definition of the velocity at the rotor plane in terms of the induction factor ensures the change in momentum across the turbine plane balances the thrust extracted; however, similar to the other models discussed in § 2.1.1, we ignore changes to the pressure as well as viscous effects). In eq. (2.1.8), we have made use of the expression for the minimum streamwise velocity occurring at $x_0$, $U_{x0} = (1 - 2a)U_0$ proposed by [47] and others.
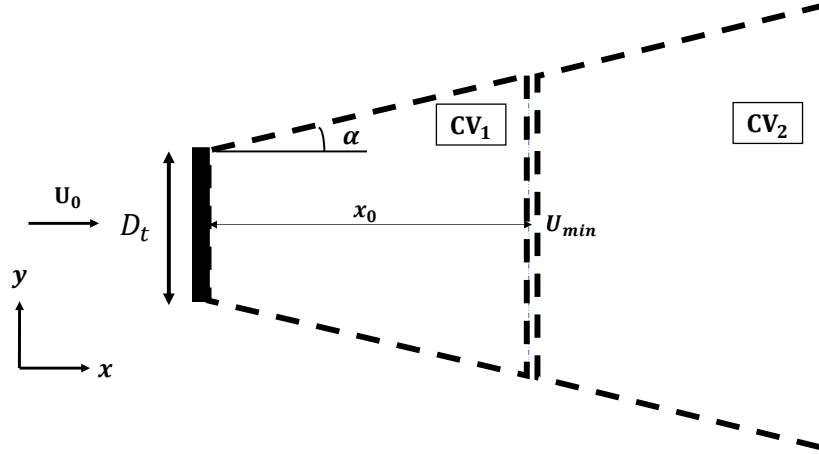


Figure 2.1: Control volume downstream of a turbine showing near-wake $(x < x_0)$ and far-wake $(x > x_0)$ regions.

3) From dimensional arguments, we take $D(x) \sim u't$, where $u'$ represents the characteristic turbulent velocity scale associated with the dominant coherent structures in the wake. Writing $u' \sim I_t U_0$, so that

$$D(x) \sim I_t U_0 t \sim C I_t x \qquad (2.1.9)$$

where $C$ is a coefficient that will be determined by fitting to LES simulations of single-turbine wakes, and we have taken advantage of Taylor's hypothesis to suggest $x \sim U_0 t$. Combining eq. (2.1.6) with eq. (2.1.9), the wake growth rate $\alpha$ as a function of the turbulence intensity is written as

$$\alpha = \frac{1}{2}\frac{dD}{dx} \sim CI_t. \tag{2.1.10}$$

The corresponding location of the transition between near-wake and far wake regions as a function of the turbulent intensity is obtained by plugging in $x = x_0$ into eq. (2.1.6) and combining with (2.1.10) to give

$$x_0(I_t) = \left(\frac{D_{x_0}}{D_t} - 1\right)\frac{D_t}{2\alpha} = \left(\frac{D_{x_0}}{D_t} - 1\right)\frac{D_t}{2CI_t}, \tag{2.1.11}$$

while $D_{x_0}$ in the above equation is computed from eq. (2.1.8). Also note that from the above analysis (and as we will show with LES data), the product of the location of the transition point and the wake expansion rate is also a constant $(x_0(I_t) \times \alpha(I_t) = C')$.

Finally, note that as suggested in [9, 42, 48], the wake expansion factor can be influenced by not only the ambient turbulent intensity $I_{t,0}$, but also turbine-induced turbulence. In particular, when the added effect of turbine-induced turbulence was considered, enhanced mixing, faster wake recovery and higher wake expansion factors have been observed [49]. In [46, 50], the wake expansion modified by these effects was modeled as $\alpha_{wake} = \alpha\frac{I_{t,wake}}{I_{t,0}}$, although this effect is not considered in the current work. In evaluating our model eq. (2.1.11) for upstream turbines, we take $I_t = I_{t,0}$ the ambient turbulent intensity. However, the turbulent intensity approaching the downstream turbines includes the effects of both the ambient free-stream turbulence (through entrainment) and the machine turbulence shed by an upstream turbine $I_+$, and must be computed from $I_t = \sqrt{{I_{t,0}}^2 + {I_+}^2}$ as suggested by [46, 48, 51]. In computing $I_t$ for downstream turbines, we use the expression for the added wake turbulence

$$I_+ = 5.7 C_T^{0.7} I_{t,0}^{0.68} \left(\frac{x}{x_0}\right)^{-0.96} \tag{2.1.12}$$

suggested by [52]. The above expressions for the added wake turbulence $I_+$ and the total turbulence $I_t$ were independently verified by computing the wake turbulence intensity approaching a downstream turbine directly from the LES results by averaging over a rectangular window of dimensions $2D_t \times D_t \times D_t$ upstream of that device.

### 2.1.3. A wake interaction model for turbulence effects

We modify the UWFLO model [16] to incorporate the above turbulence and wake structural effects on the total array flow field and power performance. The UWFLO model [16] computes the total power of an array of wind turbines or OCTs, by accounting for the cumulative momentum shadowing of upstream wakes. In the original UWFLO model, a linearly expanding wake is assumed, while the near-wake region was neglected. We briefly describe the UWFLO model, before discussing the modifications proposed here. The effect of an upstream turbine '$i$' on a downstream turbine '$j$' is computed in the UWFLO framework as follows:

1. First, an influence matrix $M_{ij}$ is defined which categorizes turbine pairs $(i,j)$ according to:

$$M_{ij} = \begin{cases} +1 & if\ turbine\ i\ influences\ turbine\ j \\ -1 & if\ turbine\ j\ influences\ turbine\ i \\ 0 & if\ there\ is\ no\ mutual\ influence \end{cases} \quad (2.1.13)$$

Turbine $j$ is affected by the wake of turbine $i$, if and only if:

$$x_{ij} < 0, and\ d_{ij} - \frac{D_{t,j}}{2} < \frac{D_{ij}}{2} \quad (2.1.14)$$

where $D_{t,j}$ is the rotor diameter of turbine $j$, $D_{ij}$ is the diameter of the wake from upstream turbine $i$ reaching the downstream turbine $j$, and

$$x_{ij} = x_i - x_j, \qquad y_{ij} = y_i - y_j, \qquad d_{ij} = \sqrt{x_{ij}^2 + y_{ij}^2} \quad (2.1.15)$$

2. Turbines are rank ordered according to their influence number, which is based on their location along the streamwise coordinate $x$.

3. In the UWFLO framework, the velocity deficit associated with downstream turbines is obtained by consistently accounting for the momentum shadowing due to upstream devices by adding the velocity deficits in quadrature:

$$U_j = U_0 - \sqrt{\sum_{i=1}^{N} \frac{A_{ij}}{A_j} \left(U_0 - U_{i,j}\right)^2} \qquad (2.1.16)$$

where $U_0$ is the upstream inlet velocity approaching the first turbine, $U_{i,j}$ is the velocity of wake from turbine $i$ reaching a downstream turbine $j$, $A_{ij}$ is the overlap area between the wake of turbine $i$ and the blade swept area of $j$ (figure 2.2) and can be computed using the geometrical principles in [16].
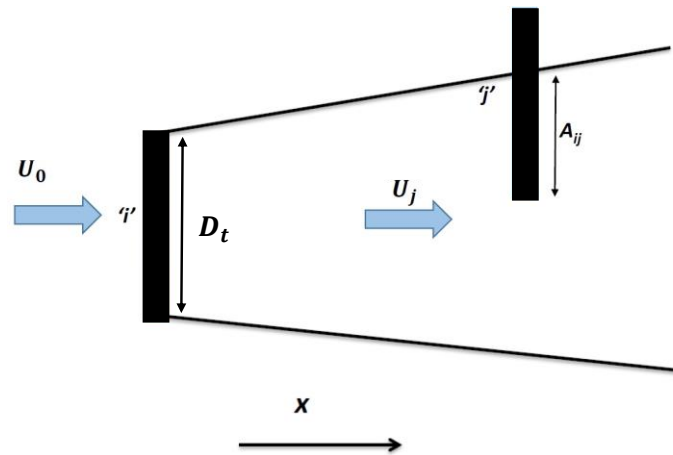


Figure 2.2: Schematic for UWFLO [16] model showing multiple OCT turbines with wake interaction.

4. In the original UWFLO [16] model, a *Jensen* [37] wake was assumed with a wake diameter that is a linear function of the downstream distance $x$. From applying mass

conservation over the control volume $CV_2$ in figure 2.1, and neglecting the near-wake region $(CV_1 \rightarrow 0)$,

$$U_{i,j} = U_j(1 - \frac{2a}{(1 + \frac{2\alpha x}{D_t})}) \tag{2.1.17}$$

The velocities $U_{i,j}$ are then substituted in eq. (2.1.16) to compute the average upstream velocity approaching each downstream turbine '$j$' and accounting for the velocity deficits of all upstream turbines '$i$' that satisfy eq. (2.1.14).

5. Finally, the corresponding power produced by turbine '$j$' is computed from

$$P_j = C_p \frac{1}{2} \rho A U_j^3 \tag{2.1.18}$$

where $C_p$ is the power coefficient defined as $C_p = 4a(1 - a)^2$, and the total array power for $N$ turbines is obtained as $P_{total} = \sum_{j=1}^{N} P_j$.

The above framework is modified by first applying a modified control volume analysis that allows for separate near-wake $CV_1 \neq 0$ and recovery regions. First, enforcing continuity between the turbine plane and a downstream plane within $CV_1$ (figure 2.1), and assuming a linear expansion of the wake in between, an expression for the velocity at the downstream location may be obtained as:

$$U_t A_t = U(x) A_x \Longrightarrow U_0(1 - a) R_t^2 = U(x)(R_t + \alpha x)^2 \tag{2.1.19}$$

$$\frac{U(x)}{U_0} = \frac{(1 - a)}{\left(1 + \frac{2\alpha x_{ij}}{D_t}\right)^2} \tag{2.1.20}$$

From a similar analysis and applying continuity to the planes containing the transition point $x_0$ and a point $x$ in the far wake (control volume $CV_2$ shown in Figure 2.1), the velocity in the far wake is then obtained as:

$$U_{x0}A_{x0} + U_0(A_x - A_{x0}) = U(x)A_x \tag{2.1.21}$$

$$(1 - 2a)U_0(R_t + \alpha x_0)^2 + U_0((R_t + \alpha x)^2 - (R_t + \alpha x_0)^2) = U(x)((R_t + \alpha x)^2) \tag{2.1.22}$$

$$\frac{U(x)}{U_0} = 1 - \frac{2a}{\left(1 + \frac{2\alpha(x_{ij} - x_0)}{D_{x_0}}\right)^2} \tag{2.1.23}$$

In rewriting eq. (2.1.23) from eq. (2.1.22), we have replaced $x$ with $x_{ij}$ to represent the development of the wake originating from turbine $i$ and reaching turbine $j$. When $x_0 \to 0$ (neglecting the near-wake region), the expression for the Jensen wake eq. (2.1.1), is recovered, while the near- and far-wake solutions are matched for finite $x_0$ as $x \to x_0$. The solution for the streamwise velocities in the near- and far-wake regions are then given by:

$$\begin{cases} U_{i,j} = \dfrac{U_j(1 - a)}{\left(1 + \dfrac{2\alpha x_{ij}}{D_t}\right)^2} & x_{ij} < x_0 \\[4em] U_{i,j} = U_j\left(1 - \dfrac{2a}{\left(1 + \dfrac{2\alpha(x_{ij} - x_0)}{D_{x_0}}\right)^2}\right) & x_{ij} > x_0 \end{cases} \tag{2.1.24}$$

In practice, the main steps for calculating the modified wake interaction model by incorporating the effects of turbulent intensity and near-wake region are:

1)  Compute UWFLO wake model equation (2.1.16) using $U_{i,j}$ obtained from equation (2.1.24).

2)  The wake growth rate $\alpha$ and the location of the wake transition $x_0$ for upstream turbines used in eq. (2.1.24), are computed from eq. (2.1.11), where $C$ is obtained from fitting to LES data.

3) For downstream turbines, we compute $\alpha$ used in eq. (2.1.24) based on the total turbulence intensity including both ambient and wake effects as suggested in § 2.1.2.

## 2.2. Numerical Simulations

The simulations reported in this article were performed using the STAR-CCM software and employed the LES methodology. The filtered Navier-Stokes equations were solved using a finite-volume discretization given by

$$\frac{\partial \bar{u}_i}{\partial x_i} = 0 \tag{2.2.1}$$

$$\frac{\partial \bar{u}_\iota}{\partial t} + \bar{u}_j \frac{\partial \bar{u}_\iota}{\partial x_j} = -\frac{1}{\rho}\frac{\partial \bar{p}}{\partial x_i} + \frac{1}{\rho}\frac{\partial \tau_{ij}}{\partial x_j} + \frac{\partial}{\partial x_j}\left(\nu \frac{\partial \bar{u}_\iota}{\partial x_j}\right) + f_i \tag{2.2.2}$$

where the overbars represent quantities that survive the filtering process, $\bar{u}_\iota$ and $\bar{p}$ are the filtered velocities and pressure, $\tau_{ij}$ is the modeled stress and $f_i$ is the body force term. Sub-grid contributions to eqs. (2.2.1) – (2.2.2) are represented using a subgrid scale (SGS) model [53] with a Smagorinsky model constant value of 0.1.

Figure 2.3 shows a schematic of the simulation domain employed in the LES simulations of a single turbine. The simulation domain was extended with an appropriate scaling factor to accommodate multiple turbines. The 3D computational domain is comprised of three meshing zones, representing a hierarchical meshing strategy: the turbine is located in zone 1 which spans a distance $2D_t$, with a mesh spacing $\Delta_1 \sim 0.025D_t$. Similarly, zones 2 and 3 are concentric with $\Delta_2 = 2\Delta_1$ and $\Delta_4 = 4\Delta_1$. In all the simulations, the mesh resolution across the turbine, and the scaling relationship between the three zones was maintained. Simulations were performed with total mesh sizes of $10^6$, $10^7$ and $2\times10^7$ to demonstrate convergence of first- and second-order quantities of interest. The lateral boundaries were

treated as periodic surfaces, while an outflow boundary condition was enforced at the outlet boundary to ensure flow features exit without generating spurious reflections. The simulation domain had dimensions of $20D_t$ in the axial direction and a cross-section of $8D_t$ x $8D_t$, while the turbine was located at a distance of $4D_t$ from the inlet plane to allow for upstream effects (due to the turbine potential flow) to develop.
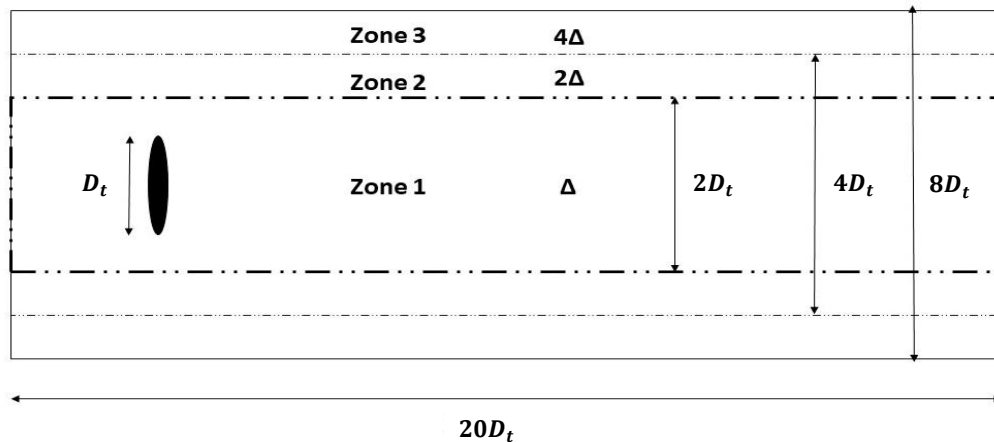


Figure 2.3: Schematic of the LES simulation domain with different meshing zones displayed.

The turbine was modeled in our simulations using the BEM [39]. In this approach, the turbine airfoils are discretized radially into blade elements whose lift and drag forces are computed in response to the local incident effective velocity. The performance of the OCT is then obtained by numerically integrating the forces along the blade span [39], while the turbine blades were taken to have the aerodynamic properties of a Gottingen 804 airfoil [52]. The properties of the airfoils including the drag and lift coefficients, thickness, chord length and twist angle were all obtained as functions of the radius from published experimental data [54]. The complete list of LES simulations reported in this study is given in Table 2.1.

Table 2.1: Summary of LES simulations of single-turbine and array configurations.

| Case number | Configuration | Turbulence intensity |
|:---:|:---:|:---:|
| 1 | Single turbine | 0.03 |
| 2 | Single turbine | 0.05 |
| 3 | Single turbine | 0.12 |
| 4 | Single turbine | 0.2 |
| 5-8 | Two turbine tandem | 0.2 |
| 9 | OCT array (scattered) | 0.2 |
| 10 | OCT array (scattered) | 0.2 |
| 11 | OCT array (scattered) | 0.05 |
| 12 | OCT array (periodic 4x4) | 0.2 |

*2.2.1. Inlet turbulence flow field*

We briefly describe the methodology developed in [55, 56] to generate the turbulent spatiotemporal velocity field that constitutes the inlet boundary condition in our simulations. The flow conditions at the inlet plane were generated as a function of time, that were then fed in to the LES computational domain. Following [57] and Acoustic Doppler Current Profiler (ADCP) current measurements reported in [3], the ocean turbulence velocity fluctuation spectrum $G^{(i)}$ along direction $(i)$, was modeled as containing an inertial range $(f^{-5/3})$ with maximum and minimum frequencies of $f_{max} = 1$ Hz and $f_{min} = 0.01$ Hz respectively, and a freestream turbulence intensity in the streamwise direction that was varied in our simulations. Spatial coherence over the inlet

plane was introduced through a coherence parameter $\xi$, which was then used to compute a coherence function. Larger values of the coherence parameter $\xi$ correspond to smaller-scale coherent structures in the inlet flow field and vice versa. Simulations with $\xi = 10$ were performed in this study. The velocities were then generated in time by summing over the frequencies but randomized by introducing a random phase angle. The cross-axial components were generated using a similar approach, while an anisotropy ratio of one was assumed between the axial and lateral velocities. The relationship between the turbulence spectrum, standard deviation in each velocity direction, and the turbulence intensity can be summarized through the following equations [55, 56]:

$$\epsilon_{(i)}^2 = \int_{f_{min}}^{f_{max}} G^{(i)} \, df \tag{2.2.3}$$

$$I_{t,0} = \frac{|\epsilon|}{|U|} \tag{2.2.4}$$

In eqs. (2.2.3) – (2.2.4), $\epsilon_{(i)}$ represents the standard deviation of velocity fluctuations along the $(i)$ direction, and $|\epsilon| = \sqrt{\sum_i \epsilon_{(i)}^2}$. Figure 2.4 (a) is a comparison of the power spectral density associated with the synthetic turbulent field at the inlet plane, and the corresponding ADCP measurements in the GS. The current measurements were collected using a 150 KHz ADCP moored in the GS, off the coast of Cape Hatteras, North Carolina [4], but only a 400 s window was analyzed for figure 2.4 (a).

A convective turbulent flow field ($\mathbf{u}$(y,z,t), where (y,z) are directions perpendicular to the mean streamwise flow) spanning a total time window of 400 s was generated using the above approach with an average axial velocity of 1 m/s, anisotropy ratios of 1 between the principal and lateral directions (to match ADCP measurements from [4]), while the turbulence intensity was varied. The 2D time-dependent snapshots were then fed into the

inlet plane of the LES computational domain, where they were interpolated into the simulation mesh and in time to correspond to the local timestep. Figure 2.4 (b) shows such a snapshot of contours of the instantaneous, streamwise velocity field $u(y,z)$ corresponding to $I_{t,0} = 0.2$, and $\xi = 10$. The simulations were run for a total time of *400 s*, of which the first 200 s were used to clear the transients out from the computational domain. This startup time for data collection was chosen to be the time taken for coherent structures to traverse the entire length of the simulation domain at the mean convective velocity: i.e. $\frac{L}{U_0} \sim 200$ s). The turbulent statistics and data analysis were then computed during the $200 - 400$ s simulation window, corresponding to $\sim 20$ turnover times for eddies with turnover times of $\frac{D_t}{U_0}$. Our simulation results were validated by comparing them with other published LES data using both actuator disk and BEM models [49]. Table 2.2 summarizes the input parameters that define the turbulent flow at the inlet boundary.
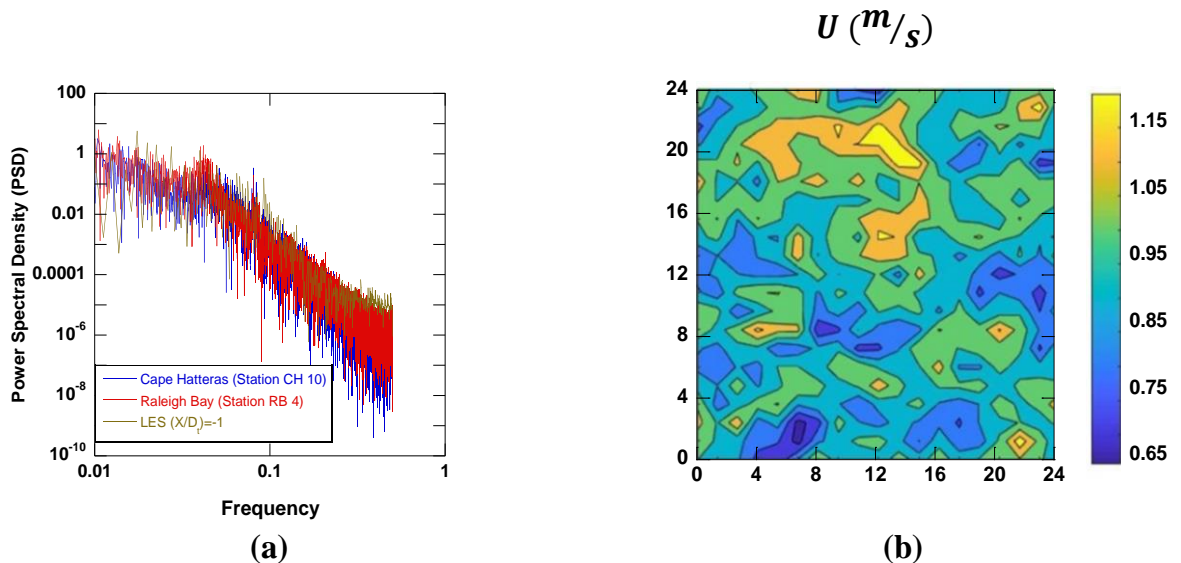


Figure 2.4: a) Comparison of power spectral densities from synthetic turbulence field and ADCP measurements from the Gulf Stream reported in [4]. b) Streamwise instantaneous velocity contours on the inlet plane generated using the approach discussed: $\xi = 10$, $It, 0 = 0.2$.

## 2.3. Single turbine results

In this section, we discuss results from LES simulations of a single turbine operating under turbulent conditions, while a comparison of the simulation data for array conditions with the modified UWFLO model is presented in § 2.4. The single-turbine results serve to validate our model for the wake structure in eqs. (2.1.11) and (2.1.24), for different levels of $I_{t,0}$. The spatial and temporal characteristics were analyzed to clarify the behavior of the turbulent wake in the near- and far-wake regions. The wake recovery models of [42] and [38] are also compared with our LES results. A comparison of model results with the single-turbine LES data of [10] is also presented in this section.

Table 2.2: Flow parameters for turbulent inlet flow.

| Parameter | |
| --- | --- |
| Average Streamwise Velocity | 1 m/s |
| Minimum Frequency | 0.01Hz |
| Maximum Frequency | 1 Hz |
| Tip Speed Ratio | 7.2 |
| Turbulence Intensity | 0.05 – 0.2 |

Qualitative results in the form of iso-surfaces of the vorticity and the second eigenvalue of the strain rate tensor ($\lambda_2$) [58] are shown in figures 2.5 (a) – (b) corresponding to $I_{t,0} = 0.2$ at t = 400 s. In the absence of tip vortices which are not captured in our LES, the wake turbulence is dominated by coherent longitudinal structures that contribute significantly to the entrainment of ambient fluid outside the wake. The $\lambda_2$ field is more compact than the vorticity magnitude field, since it represents persistent coherent structures [58]. These structures persist for several diameters downstream, while the finer-scale structures are

rapidly dissipated by the wake shear in our simulations (figure 2.5 (b)). From figure 2.5 (b), a clear demarcation between a near-wake region dominated by wake turbulence, and a far-wake recovery region in which significant entrainment of ambient fluid leading to dissipation of coherent structures is visible.
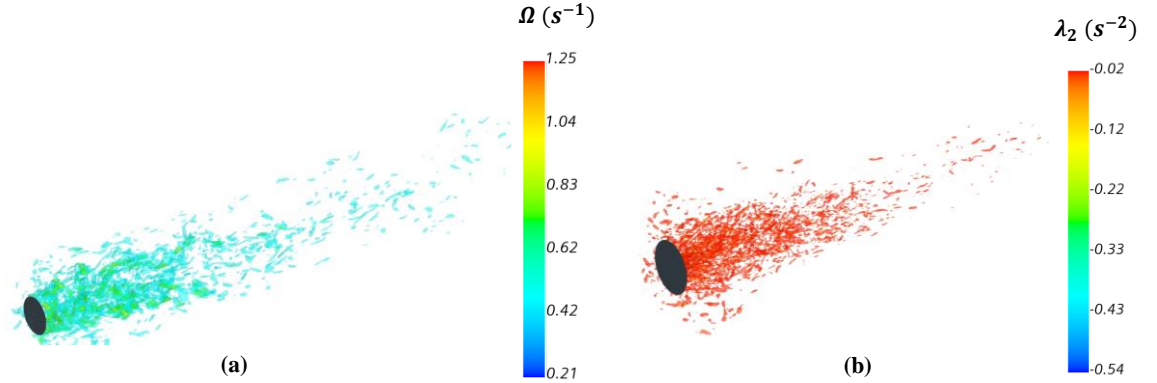


Figure 2.5: Iso-surfaces of the vorticity (a) and $\lambda_2$ (b) magnitude from single-turbine LES at t = 400 s (case 4).

In figure 2.6 (a), we plot the downstream evolution of the local turbulence intensity $I_t(x) = \dfrac{\sqrt{\frac{1}{3}(u'^2 + v'^2 + w'^2)}}{\sqrt{U^2 + V^2 + W^2}}$ from simulations with inlet turbulence levels $I_{t,0} = 0.05$ (case 2) and 0.2 (case 4). The streamwise variation plots in figure 2.6 were generated by first averaging over the data collection time window, and then averaging over the wake diameter. The turbine is located at $x/D_t = 0$ and adds significant turbulence to the incident flow, as observed in the contours of figure 2.5, and figure 2.6 (a). At the transition point $x_0$ between the near- and far-wake regions, the downstream turbulence intensities in both simulations reach a peak value of ~ 0.26 due to significant turbulent kinetic energy (TKE) production for $x < x_0$. Previous studies [51, 59] have shown the onset of turbulence decay at $x_0$ coincides with the instability-driven breakdown of tip vortices. Since the BEM employed in our simulations does not account for rotational effects, the wake dynamics in our

simulations are statistically axisymmetric and dominated by longitudinal vortices (similar to the wake structures observed in the LES of [49]). The induced velocities from these vortex structures entrain ambient fluid into the wake, leading to the observed decay in wake turbulence intensity for $x > x_0$.

The evolution of the corresponding averaged streamwise velocity profiles are shown in figure 2.6 (b). The near-wake region is evident in the decrease of $U(x)$ for $x < x_0$, as a result of momentum removal by the turbine. Momentum recovery is observed for $x > x_0$, although the transition location $x_0$ itself can depend on the inlet turbulence intensity. This is shown in figure 2.6 (c), by plotting the scaled mean streamwise velocity $\frac{U(x)-U_{x_0}}{U_0-U_{x_0}}$ against the streamwise coordinate $x/D_t$. As the inlet turbulence intensity is increased from $I_{t,0} = 0.05$ to $0.2$, wake recovery occurs earlier, consistent with the enhanced entrainment observed at higher levels of inlet turbulence.
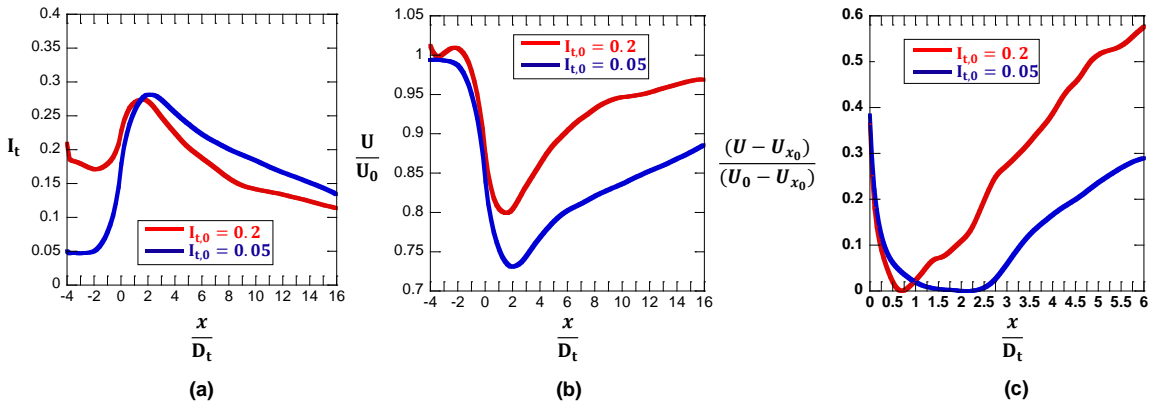


Figure 2.6: Variation of spanwise-averaged a) turbulence intensity $I_t$, b) scaled mean streamwise velocity $U/U_0$, c) scaled velocity $(U - U_{x_0})\big/(U_0 - U_{x_0})$ along streamwise distance $x/D_t$ (cases 2 and 4).

In figure 2.7, we plot the development of the mean non-dimensional velocity deficit $\frac{\Delta U}{U_0}$ at different downstream locations $\frac{x}{D_t}$ from simulations with $I_{t,0} = 0.05$ and $0.2$. As reported in previous studies, a pronounced wake deficit is observed in the near-wake region $\frac{x}{D_t} = 2$, which is completely overcome by entrainment by $\frac{x}{D_t} = 8$. The velocity profile downstream has two peaks in the near-wake region due to the presence of the turbine shear layer, that creates a 'potential core' region [60, 61] at the center occupied by relatively quiescent fluid. As the wake recovers, the velocity deficit assumes a unimodal shape resulting from the merging of the shear layer streams, which consume the potential core region. The Gaussian shape of the scaled velocity deficit within the far-wake region represents the assumption of a self-similar wake behavior for $x > x_0$. As the turbulence intensity is increased, every aspect of wake recovery is accelerated as shown in figs.2.7 - 9. For $I_{t,0} = 0.2$, the collapse of the potential core occurs as early as $\frac{x}{D_t} = 4$ as seen in the unimodal velocity deficit profile, while by $\frac{x}{D_t} = 8$ turbulence-driven entrainment has resulted in a significant wake recovery.
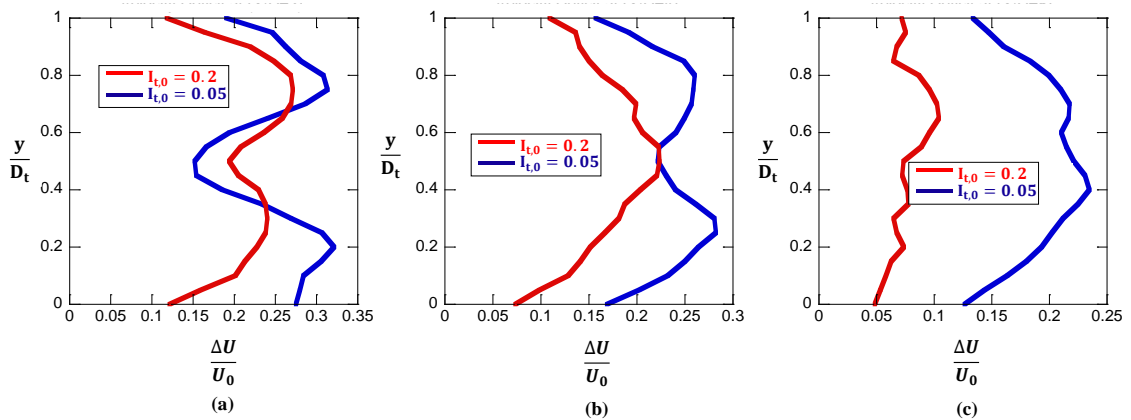


Figure 2.7: Cross-stream profiles of the mean velocity deficit $\Delta U / U_0$ at $x/D_t = 2$ (a), 4 (b), and 8 (c) for cases 2 and 4.

Components of the kinematic shear stress associated with the turbulent wake are plotted at several planes downstream of the turbine in figures 2.8 – 2.9. Figure 2.8 shows the evolution of the streamwise velocity fluctuation term $\frac{\langle u'^2 \rangle}{U_0^2}$ (where $\langle \ \rangle$ indicates time-averaging as outlined before) at $x/D_t = 2$, 4, 8, and follows the same trend as previous results from [49, 62-64]. At $\frac{x}{D_t} = 2$, significant turbulence production is observed within the shear layer regions of the wake, as the vortical structures in this region are strengthened by the local shear. The local valley in $\frac{\langle u'^2 \rangle}{U_0^2}$ near the wake centerline ($\frac{y}{D_t} = 0.5$) in fig. 2.8 (a) is consistent with the presence of a potential core in the near-wake region. As the shear layers merge overcoming the potential core, a single-peak is observed at the centerline, while the edges of the shear-layer show very low turbulence activity. By $\frac{x}{D_t} = 8$, the $I_{t,0} = 0.2$ case has entrained significant ambient fluid returning a nearly flat, quiescent profile for $\frac{\langle u'^2 \rangle}{U_0^2}$. This observed laminarization of the wake appears earlier in the $I_{t,0} = 0.2$ simulation, once again suggesting high levels of upstream turbulence lead to a faster wake recovery.



(a)  (b)  (c)
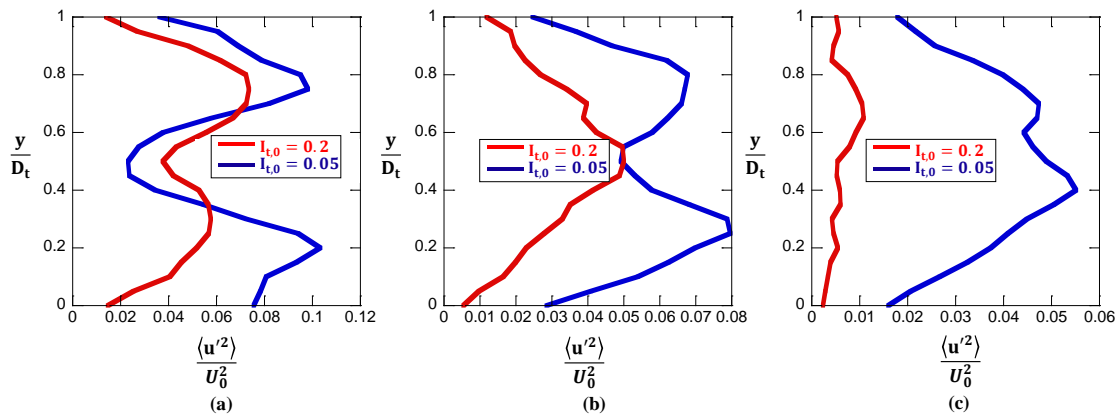
Figure 2.8: Cross-stream profiles of $\langle u'^2 \rangle / U_0^2$ at $x/D_t = 2$ (a), 4 (b), and 8 (c) for cases 2 and 4.

Cross-stream profiles of the Reynolds stress component $\frac{\langle u'w' \rangle}{U_0^2}$ are shown in figure 2.9, where $u'$ and $w'$ represent fluctuating components of the streamwise and vertical velocities respectively. In contrast to the $\frac{\langle u'^2 \rangle}{U_0^2}$ profiles, plots of $\frac{\langle u'w' \rangle}{U_0^2}$ in figs. 2.9 (a-c) show an anti-symmetric behavior with positive and negative peaks corresponding to the bottom and top shear layers respectively, while absolute values around the blade tips are maximum. Once again, the peaks are gradually attenuated as the flow emerges from the near-wake region, while the rate at which this happens is governed by the upstream turbulence intensity as described earlier.
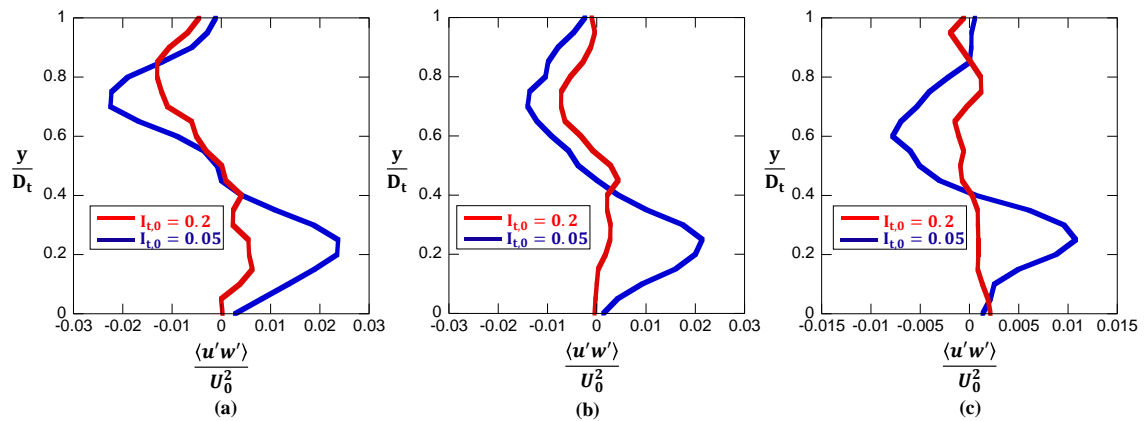


Figure 2.9: Cross-stream profiles of $\langle u'w' \rangle / U_0^2$ at $x/D_t = 2$ (a), 4 (b), and 8 (c) for cases 2 and 4.

In figure 2.10 (a), the locations of the transition point separating the near- and far- wake regions are plotted from simulations at different turbulent intensities - $x_0$ for each case in

fig. 2.10 (a) is computed as the streamwise location at which $\frac{U(x)-U_{x_0}}{U_0-U_{x_0}}$ reaches its minimum

in fig. 2.6 (c). The LES data are compared with the models of [45, 60] and the expression

in eq. (2.1.11). For the Ishihara model [45], $x_0$ is determined as the $x$-location where eq.

(2.1.5) reaches a maximum value. The transition point between the near- and far-wake

regions can also be obtained from the semi-empirical model of Vermeulen [60], which is

based on including the effects of wake growth from (i) ambient turbulence, (ii) turbulence

induced from the shear between the wake flow and the ambient flow, and (iii) machine-

induced turbulence. All models in fig. 10 provide good agreement with simulation data for

large values of $I_{t,0}$. For low values of $I_{t,0}$, the model of [45] underpredicts our LES data.

Furthermore, note that the model of [60] predicts a finite value for $x_0$ as the flow

approaches the laminar limit ($I_{t,0} \to 0$), which is incorrect. Thus, from figure 10, eq.

(2.1.11) captures the behavior of the wake structure for all values of $I_{t,0}$, including the

nearly laminar limit. This prescription forms the basis of our turbine array model described

in § 2. Finally, eq. (2.1.11) does not account for the mechanical properties of the turbine

and its operation parameters, which are typically captured through the number of turbine

blades, tip speed ratio and the thrust coefficient [60]. These aspects of the wake transition

will be taken up in future studies. Note that from combining eqs. (2.1.10) and (2.1.11), $\alpha x_0$

should be a constant in our study, independent of $I_{t,0}$ (since the induction factor was not

varied in our simulations). In fig. 2.10 (b), we verify this by plotting $\alpha x_0$ from the LES

against $I_{t,0}$. The wake growth rate $\alpha$ was computed by fitting eq. (2.1.6) to the wake

envelope from our simulations, identified as the radial location where the averaged

streamwise velocity reached 99% of its upstream value [65].
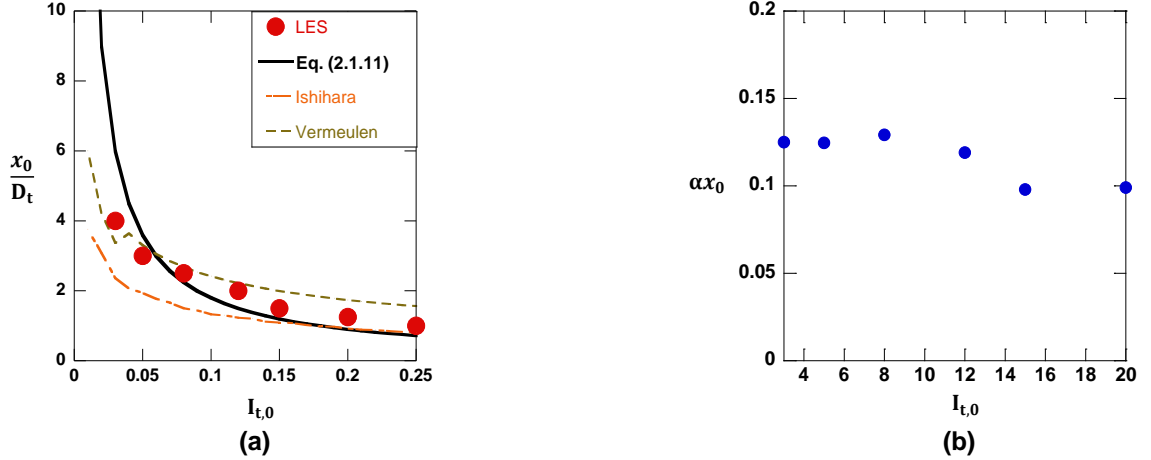
Figure 2.10: (a) Variation of the locations of the transition point $x_0$ between the near- and far- wake regions with the turbulence intensity $I_{t,0}$ : Comparison between LES data and models. (b) plot of $\alpha x_0$ vs. the turbulence intensity $I_{t,0}$ from LES data.

In fig. 2.11 (a) – (d), we plot the streamwise evolution of the mean scaled velocity deficit $\langle\Delta U\rangle/U_0$ against $x/D_t$ from the LES data, and compared with several models discussed earlier. To enable a direct comparison with the models of [37] and [38] and eq. (2.1.24), all of which assume a tophat profile for the wake streamwise velocity, $\langle\Delta U\rangle$ is obtained from LES by first time-averaging, followed by spanwise-averaging over the extent of the local wake diameter $D(x)$. The models of [37], [38] and [42] are valid in the limit $x_0 \to 0$, and hence are plotted only for the region $x' = x - x_0 \geq 0$ in fig. 11. Our model eq. (2.1.24) describes both the near- and far-wake regions, and is plotted for all $x > 0$ in fig. 11, and shows good agreement with LES data for all the turbulence intensities investigated in this study. At low values of $I_{t,0}$ (figs. 2.11 (a) – (b)), an extended near-wake region is observed in the LES data, which adversely affects the comparison with the models of [37] and [38]. As the upstream turbulence intensity $I_{t,0}$ is increased in figs. 2.11 (c) – (d), the near-wake is shortened so that the models of [37, 38, 42], and our eq. (2.1.24) converge in agreement

with the simulation data. The model of Ishihara [45] incorporates near-wake effects through a virtual origin term (eq. (2.1.5)), and is in good agreement with LES data for cases $1-3$, while case 4 ($I_{t,0} = 0.2$) is overpredicted by their model.
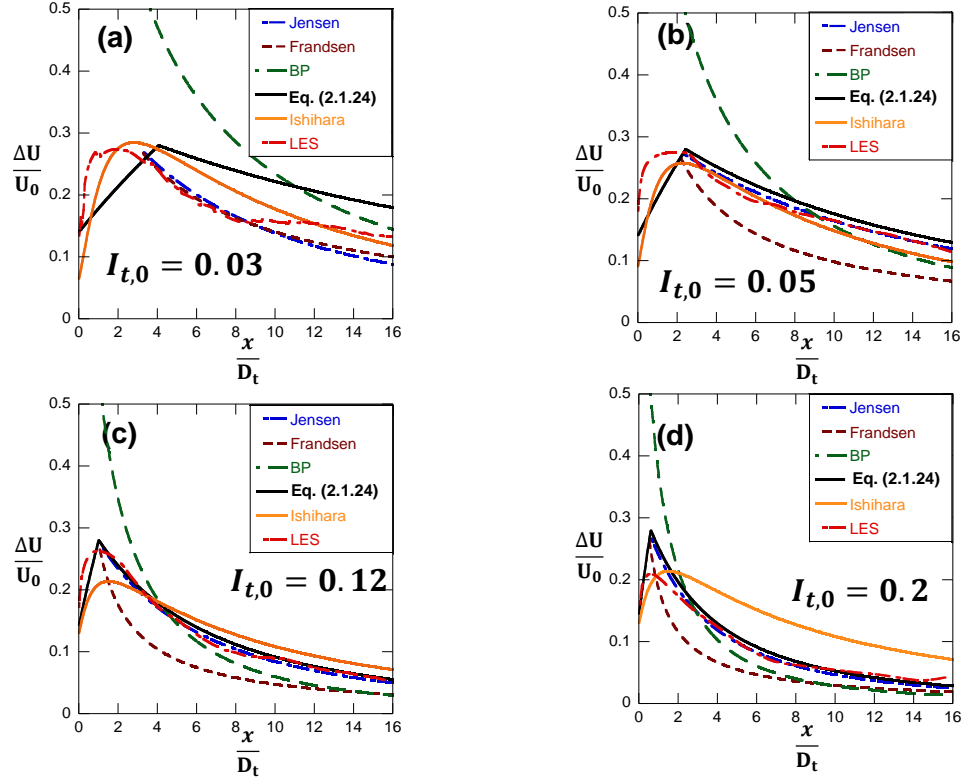


Figure 2.11: Variation of mean velocity deficit $\Delta U / U_0$ with $x/D_t$ from LES, eq. (2.1.24) and models of [37], [38], [42] and [45] for $I_{t,0}$ = (a) 0.03, (b) 0.05, (c) 0.12 and (d) 0.2.

In fig. 2.12 (a) – (b), we plot the radially integrated total mass flow deficit rate, $\int \frac{\Delta U}{U_0} dA$ derived from eq. (2.1.24) and the models of [37, 38] and [42], and compared with the LES data. For the control volumes $CV_1$ and $CV_2$ shown in fig. 2.1, a constant value of $\int \frac{\Delta U}{U_0} dA$ implies conservation of mass at every $x$-location in the wake, since it accounts for both the wake mass flux and the entrainment flux. For the LES calculations at $I_{t,0} = 0.05$ and $0.12$ in figs. 2.12 (a) – (b), the total mass flow deficit rate was computed by integrating radially

to the edge of the domain. For our model eq. (2.1.24) and the model of Jensen [37] in the fully-recovered wake $(x > x_0)$, radially integrating the deficit mass flow for a linear wake profile yields

$$\int_0^{\frac{D_{w,x}}{2}} \frac{2a}{\left(1 + \frac{2\alpha x}{D_{w,x_0}}\right)^2} 2\pi r \, dr = 2a A_{w,x_0} \tag{2.3.1}$$

where $A_{w,x_0}$ represents the area of the wake at $x = x_0$. Thus, the $rhs$ of the above eq. (2.3.1) is independent of $x$, and suggests our model maintains a constant mass flux in the far wake region, in agreement with observations from LES (figure 2.12). For the model of [38], (eq. (2.1.2)) is derived from applying momentum conservation to a control volume bounded by an inlet plane far upstream of the turbine, and an outlet plane in the far-wake region where the pressure has fully recovered. Once again integrating the model equation (2.1.2) for the velocity deficit in the radial direction yields for the total mass flow deficit rate

$$\int_0^{\frac{D_{w,x}}{2}} \frac{1}{2}\left\{1 - \sqrt{1 - \frac{2A_0}{A(x)} C_T}\right\} 2\pi r \, dr = \pi \left\{1 - \sqrt{1 - \frac{2A_0}{A(x)} C_T}\right\} \frac{D(x)^2}{4}, \tag{2.3.2}$$

which retains an x-dependence for the wake form $D(x) = D_t \left(\beta^{1/2} + \alpha \frac{x}{D_t}\right)^{1/2}$ assumed in [38], and seen in figs. 2.12 (a) – (b). Similarly, applying the above analysis to the model of [42] gives for the deficit mass flow rate,

$$\int_0^\infty \left\{1 - \sqrt{1 - \frac{C_T}{8\left(\frac{\sigma}{D_{x_0}}\right)^2}}\right\} e^{-\frac{r^2}{2\sigma^2}} 2\pi r \, dr = 2\pi \left\{1 - \sqrt{1 - \frac{C_T}{8\left(\frac{\sigma}{D_{x_0}}\right)^2}}\right\} \sigma^2 \tag{2.3.3}$$

where we take advantage of the Gaussian form of $\Delta U(x, r)$ to extend the integration to $r \to \infty$. Eq. (2.3.3) is also plotted in fig. (2.12), and shows a dependence of the deficit mass flow rate on the streamwise coordinate for the model of [42]. Finally, integrating eq. (2.1.5) from the model of [45] in a similar manner will yield

$$\int_0^\infty rhs|_{eq.(2.5)} 2\pi r\, dr = \frac{2\pi\sigma^2}{\left\{ a + b\,{}^x/_{D_t} + c\left(1 + {}^x/_{D_t}\right)^{-2}\right\}^2}. \qquad (2.3.4)$$

Outside the near-wake region, the rhs of eq. (2.3.4) is only weakly dependent on $x$, as seen in the plots in figs. 2.12, thus indicating fidelity to total mass flux conservation. For $x < x_0$, our model and eq. (2.3.4) derived from the model of [45] show mass flux increasing with streamwise distance in agreement with the trend from LES data, and consistent with the positive entrainment flux in the near-wake region.
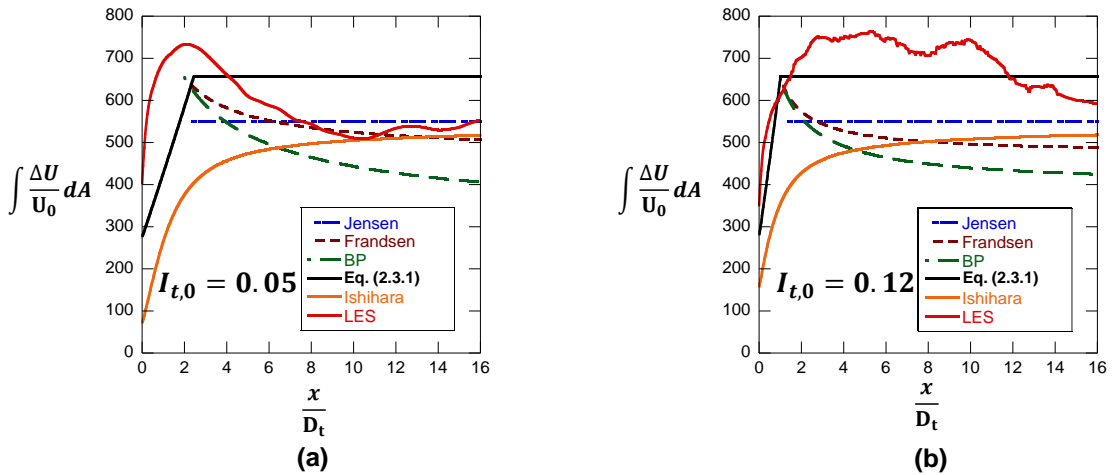


Figure 2.12: Variation of the deficit mass flux $\int \frac{\Delta U}{U_0} dA$ with $x/D_t$ from LES, proposed model eq. (2.3.1), and the wake models of [37], [38], [42] and [45] for $I_{t,0}$ = (a) 0.05, and (b) 0.12.

A comparison of the models with the LES data of [10] is presented in figure 2.13 (a) – (b) for $I_{t,0} = 0.13$ and 0.048 respectively. The two cases correspond to case 2 and 5 in the wind

turbine study of [42], which also differed in the extent of roughness effects representing the surface terrain – case 2 (fig.2.13 (a)) had a roughness of $5 \times 10^{-1}$, while case 5 (fig. 2.13 (b) was simulated with a roughness parameter of $5 \times 10^{-5}$ m). The roughness effects are not captured in any of the models discussed here, but the authors of [42] adjust the wake growth rate $\alpha$ and the wake width at $x_0$ to fit the simulation results. In contrast, our model eq. (2.1.24) and the models of [37] – [38], [45] are evaluated in fig. 2.13, for a value of $\alpha$ independent of the surface roughness, that is only determined by the upstream turbulence intensity described earlier. From figs. 2.13 (a) – (b), our model and the models of [37] and [42] are in very good agreement with the LES data presented in [10], while [38] underpredicts the simulation results. The model of Ishihara [45] captures the far-wake decay of the velocity deficit, but overpredicts the maximum value at the transition plane $x_0$. Finally, note that in [42], the LES data from [10] is plotted under the assumption of negligible near-wake distance $x_0 \rightarrow 0$, but figs. 2.17 (a) – (b) of the latter study show a finite near-wake region. In generating figure 2.13, we included the near-wake region by estimating it from the data presented in [10], and plotted the models of [37, 38, 42] by displacing them by $x_0$ since they are only valid for $x' > 0$.



(a)

(b)
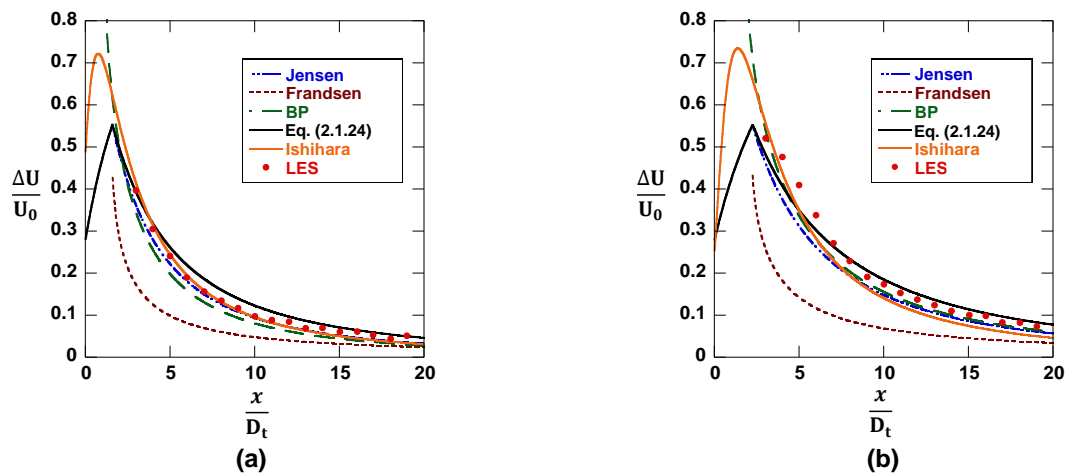
Figure 2.13: Variation of mean velocity deficit $\Delta U/U_0$ with $x/D_t$ plotted from eq. (2.24) and the wake models of [37], [38], [42] and [45], compared with the LES data from [10].

## 2.4 OCT array results

The OCT array modeling framework presented in § 2.1 is validated here against LES data over a wide range of configurations that are presented in the order of increasing complexity of wake interactions.

### 2.4.1. Two-turbine configuration:

The purpose of the simulations presented in this section is to isolate the wake interaction between an upstream and downstream turbine tandem, where the devices are colinear and aligned with the flow as shown in figure 2.14 (a). Hence, these cases allow us to examine wake interactions, but without the complicating effects of partial shadowing of overlapping wakes. We present results from cases 5 - 8, corresponding to separation distances between the turbines of $\frac{x_{12}}{D_t} = 4, 6, 8$ and 10 - the indices '1' and '2' are used to label the upstream and downstream turbines respectively. Contours of the time-averaged streamwise velocity ($U$) are presented in fig. 2.14 (a) from case 5 ($\frac{x_{12}}{D_t} = 4$). The simulations were performed with an upstream turbulence intensity of $I_{t,0} = 0.2$. As seen in fig. 2.14 (a), at this separation distance, the downstream turbine interrupts the wake recovery of the upstream OCT, and hence is operating in an environment of a significant momentum deficit. At larger separation distances, the wake recovery is allowed to proceed to a greater extent, and the downstream turbine operates in conditions that approach the freestream. In fig. 2.14 (b), we plot the relative power of the downstream turbine $P_2$ scaled by the upstream turbine power $P_1$ for different separation distances. Results from the LES data are

compared with turbine power computed from the wake velocity predicted by our model eq. (2.1.24), and show excellent agreement (rms error 1.73 %). Note that since the downstream turbines were completely obstructed by the upstream devices in these simulations, the turbine power can be computed directly by combining eqs. (2.1.24) and (2.1.18), and without accounting for the partial momentum shadowing using the UWFLO model.
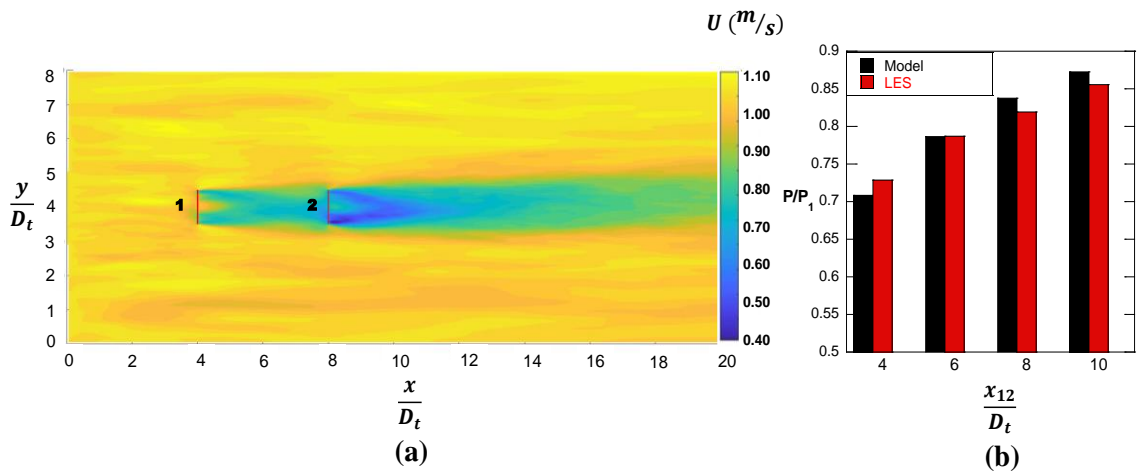


Figure 2.14: (a) Contours of time-averaged streamwise velocity, and (b) averaged relative power for each turbine from cases 5 - 8 with turbulent intensity of 0.2 (model comparison with LES).

*2.4.2. Staggered arrangement of OCTs:*

In this section, the proposed analytic model for array power as a function of ambient turbulence intensity has been validated using LES results for different layouts and conditions. In case 9, turbines were arrayed as shown in figure 2.15 (a), with the downstream turbines likely to experience significant wake shadowing effects. Furthermore, the spacing between the turbines was such that near-wake effects would play an important role in the power generation of the downstream devices. The configuration

shown in fig. 2.15 (a) also combines partial and complete shadowing effects, while all the turbines are located at the same $z$-plane. This configuration is instructive, and the significant wake interactions present a demanding validation case for the model proposed here. The instantaneous streamwise velocity contours are also shown in figure 2.15 (a), while the time dependence of the instantaneous power from each turbine are plotted in figure 2.15 (b). The time-averaged relative power output from each turbine in the simulation is compared with the prediction from the modified UWFLO model with velocity computed from eq. (2.1.24), and plotted in figure 2.16 (b). For each turbine, the upstream turbulence intensity used to drive our model equations was computed using two methods which gave similar values: from the empirical equation (2.1.12) and by averaging over a region $2D_t$ upstream of that device. For all turbines, the model prediction for relative power output is in good agreement with the simulation results which were averaged over the time window of 200 - 400 seconds with an rms error of 8.61%.
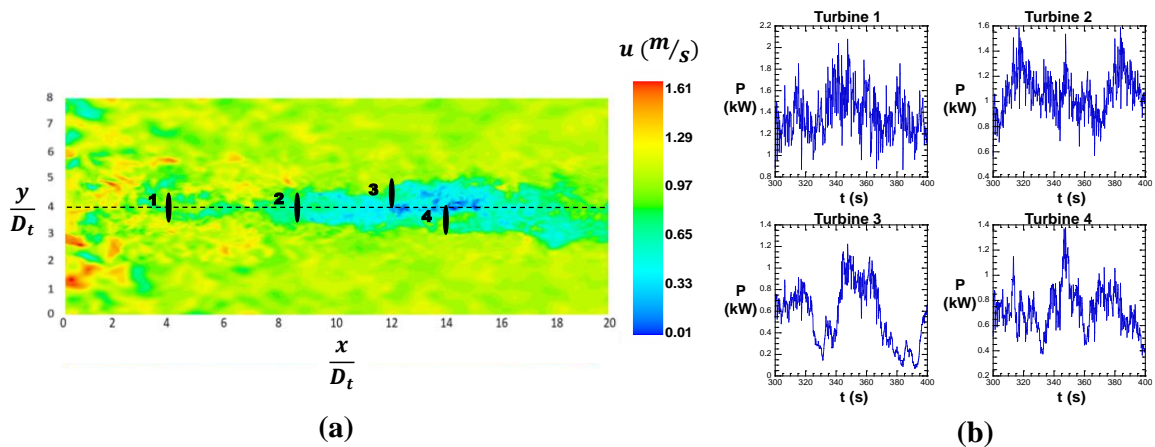


Figure 2.15: (a) Contours of instantaneous streamwise velocity from LES simulation of case 9 and (b) instantaneous turbine power as a function of time for turbines $1 - 4$ for case 9.
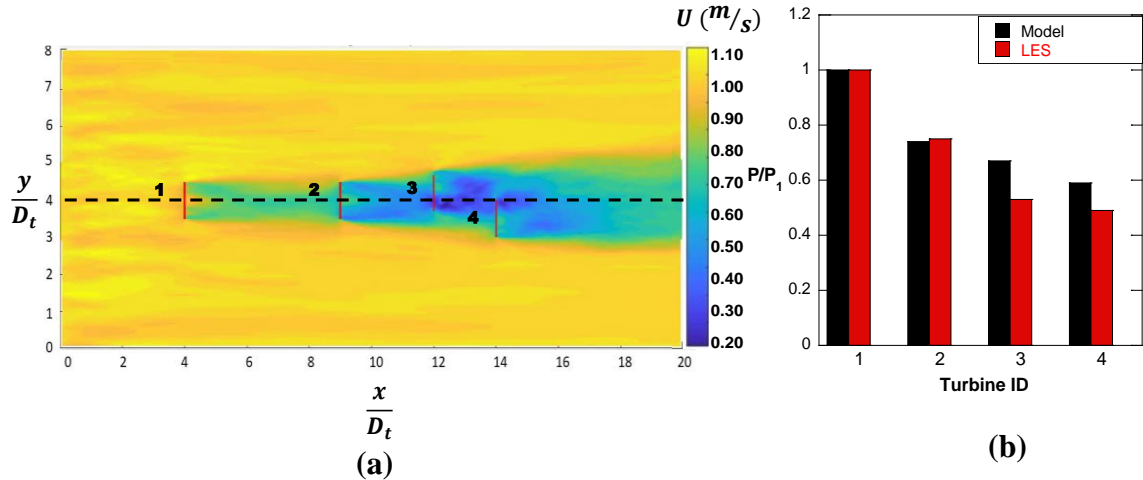
Figure 2.16: (a) Contours of time-averaged streamwise velocity, and (b) averaged relative power for each turbine from case 9 with turbulence intensity of 0.2 (model comparison with LES).

A more realistic configuration is investigated in case 10 (figure 2.17 (a)), and might result from an optimization of turbine locations in a tethered OCT farm [5]. An inlet turbulence intensity of $I_{t,0} = 0.2$ was used for this case, while the turbines were once again positioned on the same $z$-plane to ensure the presence of significant momentum shadowing. The total power output for the OCT farm from the model and LES was 10.57 and 10.13 kW respectively. The relative power of each turbine in the array is shown in figure 2.17 (b), and in good agreement with the corresponding model prediction with an rms error of 6.3 %. Finally, in fig. 2.18, we plot results from case 11, which had the turbines positioned at the same locations as case 10 but with a turbulence intensity of 0.05. Once again, the results for the relative power $P/P_1$ computed using velocities from the model eq. (2.1.24) are compared with the LES results, and show agreement with an rms error of 3.9 %.
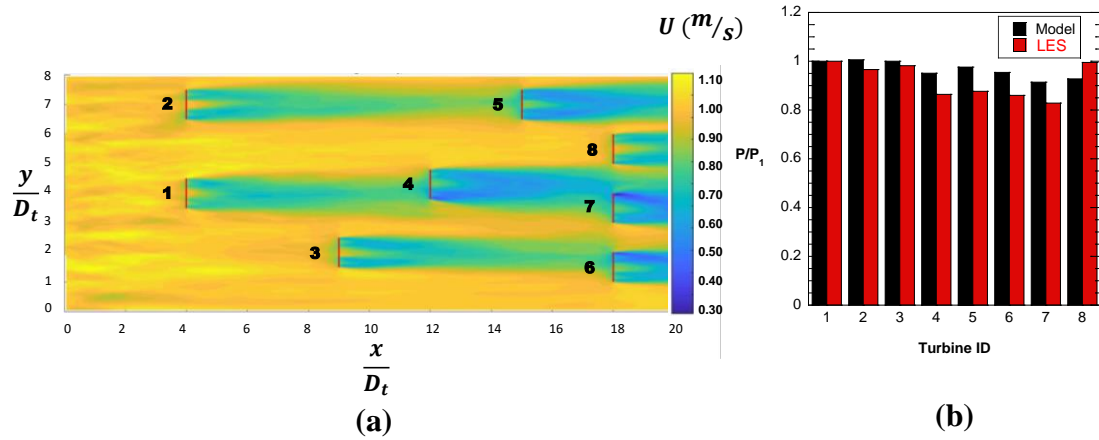
Figure 2.17: (a) Contours of time-averaged streamwise velocity, and (b) averaged relative power for each turbine from case 10 with turbulence intensity of 0.2 (model comparison with LES).
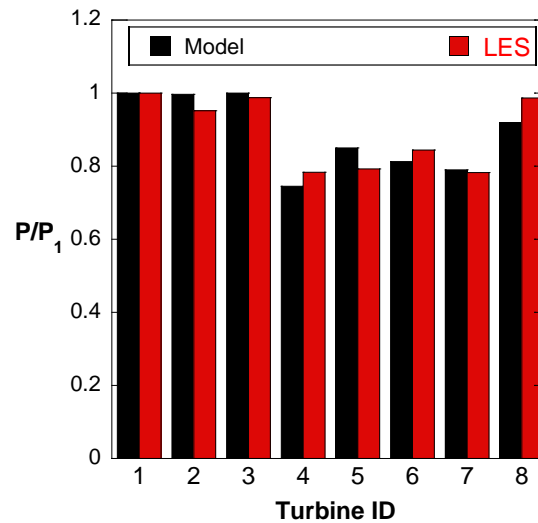


Figure 2.18: Averaged relative power for each turbine from case 11 with turbulence intensity of 0.05 (model comparison with LES).

*2.4.3. OCT array:*

Finally, we present LES results and model validation for a 4 x 4 square array of OCTs as distributed in figure 2.19 (a). The turbines were arrayed at a spacing of $6D_t$ in the $x$- and $y$- directions, and operate in an upstream turbulent inflow environment with $I_{t,0} = 0.2$. The

simulations were performed with the same effective resolution (zones/$D_t$) as the single-turbine simulations in § 2.3. Contours of the time-averaged streamwise velocity field are shown in fig. 2.19 (a), superposed on the turbine locations, where the turbines in the downstream rows exhibit shortened wake regions consistent with the higher turbulence environments in which they operate. The UWFLO model modified with our proposed expression for single-turbine wakes (eq. 2.1.24) was computed, with the turbulence intensities for the downstream turbines obtained by spatially averaging over a region of $2D_t$ before the turbine. In fig. 2.19 (b), we plot the time-averaged relative power ($P/P_1$) for all the turbines from the LES and the model calculations. The simulation results and model predictions for relative power are in good agreement, with an rms error of 2.7 %.



(a)

(b)
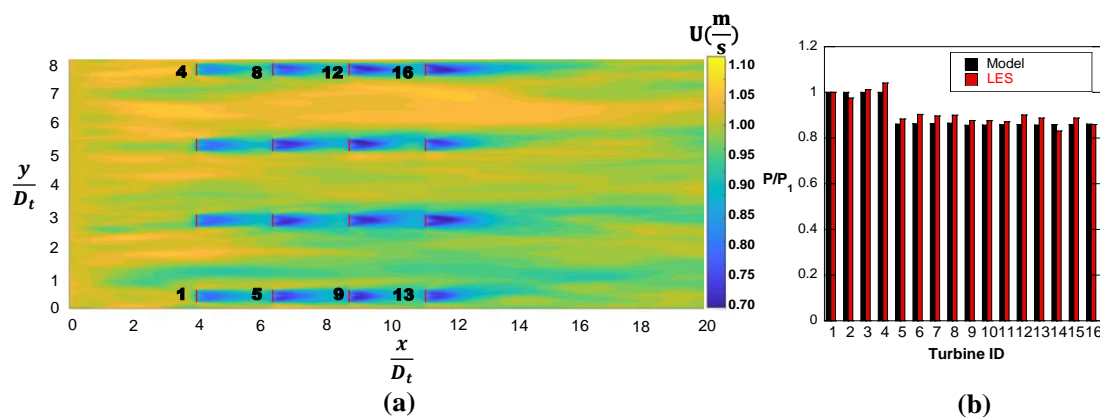
Figure 2.19: (a) Contours of time-averaged streamwise velocity, and (b) averaged relative power for each turbine from case 12 with turbulence intensity of 0.2 (model comparison with LES).

## 2.5 Summary

In this chapter, we have examined the behavior of the turbulent wakes emanating from ocean current turbines, both in single- and multi-turbine configurations. We focus on understanding the effect of ambient turbulence intensity on the development of the wake, and on the interaction between multiple OCT wakes. The study is relevant for informing

proposed deployment strategies of OCTs [2] that will involve 'flying' tethered devices moored to the ocean floor. Optimization strategies [5] will require the turbines be repositioned dynamically using tether payouts in response to the meandering of western boundary currents like the GS, leading to time-varying levels of ambient turbulence. As OCT locations are continuously modified to satisfy array optimization strategies [5], their exposure to turbulence levels will also vary significantly. Thus, in contrast to wind turbines, wake interaction models that underlie optimization strategies of OCTs must be capable of accounting for a wide range of ambient turbulence, ranging from the low turbulence levels of the ambient flow to large turbulence intensities when turbines are operating in the wake regions of other devices. In the former scenario, when turbulence levels are low, the near-wake region of OCTs will extend further due to the limited entrainment with the ambient flow. In this limit, as we have shown, several models developed for wind turbines that are valid in the limit of vanishing near-wake regions fail to produce accurate results.

To address the above issues, we have proposed a simple model that describes both the near- and far-wake regions behind an OCT device. The model assumes the Jensen [37] form in the far wake region, while the transition point at which the wake begins to recover is itself taken to depend on the turbulence intensity of the flow. While the properties and operating conditions of the turbine will certainly play a role in the structure of the near-wake through the development and breakdown of tip-vortices, these effects will be considered in subsequent articles. We find by comparing with 3D LES at different turbulence intensities, that the proposed model accurately describes this complex wake behavior. The simulations were driven by a synthetic, inlet turbulent flow field designed to match the spectral

characteristics of recent ADCP measurements made in the GS [4]. As the turbulence intensity in the upstream flow was increased, wake recovery was enhanced resulting in shorter transition distances, a trend that is captured by the proposed simple expression for $x_0$. The model is then implemented in the recently proposed UWFLO [16] framework for arrays of OCTs, that incorporates the partial momentum shadowing of upstream and downstream turbines through a geometric factor. The modified UWFLO model is validated using LES data from several configurations including turbine tandems, staggered arrangements of OCTs and OCT arrays with a constant pitch.

We expect the proposed framework can be used to predict total OCT farm power production, and suitable for real-time array optimization strategies [5]. The turbulence intensity approaching any turbine in the array can be computed from the expression $I_t = \sqrt{I_{t,0}^2 + I_+^2}$ suggested by [46, 48, 51]. The model framework, while designed with OCT operation in mind, can be readily applied to address wake interaction in wind farm arrays. In contrast to recently published models, our wake structure model requires only one constant to be determined from fitting to empirical data. We have further shown our model produces a constant mass flow rate in the far wake, while the average velocity in the near wake is obtained from momentum balance with the turbine thrust. Finally, we defer the investigation of the wake structures, resulting directly from properties of a specific turbine blade design or its operating conditions, to future studies.

CHAPTER 3: PERFORMANCE OF 3D ARRAYS OF RECONFIGURABLE OCEAN
CURRENT TURBINES IN NON-UNIFORM FLOW FIELDS

Although OCTs and wind turbines operate in a non-uniform inlet flow, the vast majority

of studies have assumed the inlet velocity to the turbines to be uniform. In the case of

OCTs, the non-uniformity in the upstream flow may stem either from background shear or

from the wakes of upstream turbines. Typically, the background shear is a rather weak

effect, while the latter creates strong, local regions of shear velocities. In this chapter, we

develop a reduced-order wake interaction model to describe the performance of an array

of OCTs operating in a spatially non-uniform inlet flow field spanning both the weak and

strong shear regimes, and validate the model with detailed numerical simulations. The

shear-modified wake interaction model presented here is general, and can be applied to

both MHK and wind energy applications, and can accommodate different functional forms

describing the shear profile. However, the special case of linear functions for the shear

profile are considered in this chapter.

The proposed model accounts for the effects of the local shear profile of turbine wakes,

specifically the extents of the near- and far-wake regions. To accomplish this, we have

extended the non-uniform wake velocity model of Chamorro and Arndt [66] to the case

with multiple turbines arrayed in an arbitrary arrangement, by integrating it with the

UWFLO model of Chowdhury et al. [16] described in chapter 3.2.2. The model was

validated with data from RANS simulations, where the turbulence was modeled using the

$k - \omega$ turbulence closure [67], while the turbines were represented as porous disks through

an Actuator Disk Model (ADM). A parametric variation spanning different non-

dimensional shear rates and turbine induction factors was also carried out, representing a broad range of conditions for model validation

## 3.1 Background

OCTs, which will be deployed in the deep waters of the GS [4], will have to be tethered to the ocean floor. The use of tethered systems in deep waters allows the OCTs to adjust their vertical positions through the adjustment of tether lengths, and their horizontal (longitudinal and lateral) positions via control surfaces [5, 6]. Recent ADCP velocity measurements in the GS have demonstrated the presence of mean flow shear of the streamwise velocity component in the cross-flow direction [2]. Yet, existing research has focused mainly on the modeling and optimization of array designs for towered turbines in shallow tidal environments, under uniform inlet flow fields [16]. In these earlier studies, the turbines were assumed to operate at similar hub heights, and often only a 2D layout was considered. The ability to optimally adjust the vertical, longitudinal, and lateral positions of turbines is important for harnessing the GS energy, as the GS has been observed to experience substantial spatiotemporal variability (through meandering, for example).

We briefly review earlier efforts at describing the performance of wind turbines operating in mean flow shear conditions. Note that since wind turbines operate within the atmospheric boundary layer, they are typically exposed to large values of shear-driven velocity gradients, which affect their power extraction. In Chamorro and Arndt [66], a reduced order model was proposed to predict the power of a single turbine operating in streamwise shear flow conditions. The authors of [66] performed a control volume analysis of a single turbine, and obtained expressions for the power coefficient in terms of the

induction factor and coefficients that capture the effects of velocity gradients. Draper et al. [68] extended the classical ADM for inviscid steady shear flow with uniform local resistance, and assumed that the lateral interaction inflow around the disc was small, while the resistance across the turbine was uniform. The power coefficients for wind turbines for both bounded and unbounded cases and for different shear rates were computed. West and Lele [69] investigated the momentum and mean kinetic energy budget for individual and wind farm turbines around an actuator disk, and derived analytic expressions for power and thrust coefficients that included the effect of non-uniform upstream profiles and boundary layer turbulence. Their results showed the Coriolis and Boussinesq coefficients recovered faster for wind turbine farms, than for isolated turbines due to the slower turbulent mixing rate in the wake and slower velocity deficit recovery observed in the latter case.

Kavari [70] investigated the effect of the shear profile across the wind turbine blades using the BEM approach, and compared the power and thrust coefficients across the blades. The main findings from that study were that the shear profile had little impact on aerodynamic parameters in the near-root region, while radial segments within 20%–80% of the blade length were the most affected. Jeong et al. [71] studied the effect of wind shear rate on aerodynamic and structural behaviors such as normal and tangential body forces, and showed fatigue loads and blade deflections occurred as a result of the sheared and turbulent flow conditions. These effects were found be more pronounced at lower wind speeds, where they were found to influence the aerodynamic and structural behaviors of the wind turbine blades.

The experimental studies of Smith et al. [72] showed that the presence of shear and turbulence in the upstream flow affect turbine power production. In the context of wind farms, experimental data points showed shear and turbulent effects were dominant during nighttime and daytime hours respectively. Vinod et al. [73] studied inflow variations in the form of freestream turbulence or non-homogeneity/shear effects, and found corresponding variations in power capture and wake characteristics. Comparison of CFD (RANS and LES) simulations with field data of a geometry-resolved, full-scale tidal turbine showed turbine wake development, propagation, and recovery may be affected by the sheared inflow [74]. In this chapter, a low-order model capable of capturing wake interactions in the presence of upstream shear has been developed, and validated with corresponding numerical simulations of turbine arrays. The modified wake interaction model is an extension to non-uniform flows of the UWFLO model of [16], and includes the effects of near- and far-wake effects as well as the mean flow shear.

## 3.2 Methodology

### 3.2.1. Wake Model for Non-uniform Inlet Velocity [66]

Our starting point for model development is the shear model of Chamorro and Arndt [66], which predicts the power of a single turbine in a non-uniform inlet velocity field, and was originally developed for wind turbines operating in the atmospheric boundary layer. A detailed description of the model is reproduced from [66] in the Appendix A.1, while we briefly review key features in this section. As discussed in chapter 2, uppercase variables indicate the results of a time averaging process, while an additional overbar will be used to represent spatial averaging, across the turbine span. Subscripts indicate the locations in Figure 3.1, where the spatial averaging is performed.

The Bernoulli equation is written between planes '0' and '$t^-$', and between '$t^-$' and '$x$' in Figure 3.1, where '$t$' indicates the turbine plane, and a linear momentum analysis is performed independently for each control volume. A generic function for the non-uniform inlet velocity $U_0(y) = U_{inlet}(y)$ is assumed at the entrance plane (0), while the corresponding area average is indicated with the overbar: $\overline{U_0} = \frac{1}{A_t}\int_0^{A_t} U_0 dA$. Corresponding averages representing the kinetic energy and the momentum fluxes cannot be similarly written with a simple area average, and require the introduction of correction factors $\Xi$ and $\Psi$: Here, $\Xi = \frac{1}{\overline{U}^3 A_t}\int_0^{A_t} U^3 dA$ is the Coriolis coefficient, and $\Psi = \frac{1}{\overline{U}^2 A_t}\int_0^{A_t} U^2 dA$ is the Boussinesq coefficient, so that $\Xi\frac{\overline{U}^2}{2}$ and $\dot{m}\Psi\overline{U}$ represent the average kinetic energy per unit mass, and momentum flux respectively.

From [66] and the summary presented in Appendix A.1, the wake velocity and power associated with a single turbine embedded in a non-uniform streamwise velocity profile respectively is given by

$$\overline{U}_x = \overline{U}_0\left(\frac{2\Psi}{\Xi}(1-a) - 1\right), \tag{3.2.1}$$

$$P = \frac{1}{2}\rho A_{t^-}\overline{U}_0^3 4\Psi(1-a)^2\left(1 + \frac{\Psi}{\Xi}(a-1)\right), \tag{3.2.2}$$

while the corresponding power coefficient is given by

$$C_P = 4\Psi(1-a)^2\left(1 + \frac{\Psi}{\Xi}(a-1)\right). \tag{3.2.3}$$

For uniform flow for a single turbine ($\Xi = \Psi = 1$), the standard result for power coefficient is recovered as

$$C_P = 4a(1-a)^2 \tag{3.2.4}$$

Applying the Betz criteria ($\frac{dC_P}{da} = 0$) [75], the maximum power coefficient for a single turbine under uniform flow is obtained from eq. (3.2.4) as $C_{P,max} = 0.59$ and occurs at $a = 1/3$. In the presence of shear, a similar analysis can be performed [66] for Eq. (3.2.3) leading to

$$\frac{dC_P}{da} = -4\Psi(1-a)\left(3\frac{\Psi}{\Xi}(a-1) + 2\right) = 0, \tag{3.2.5}$$

with a maximum power coefficient of a single turbine of $0.59 \times \frac{\Xi^2}{\Psi}$ occurring at $a = 1 - \frac{2\Xi}{3\Psi}$. For the weak shear conditions of the ocean, the power coefficient would be increased beyond the Betz limit by $\sim 1-2\%$, while for $\Xi = \Psi = 1$ we recover the results from uniform upstream flow.
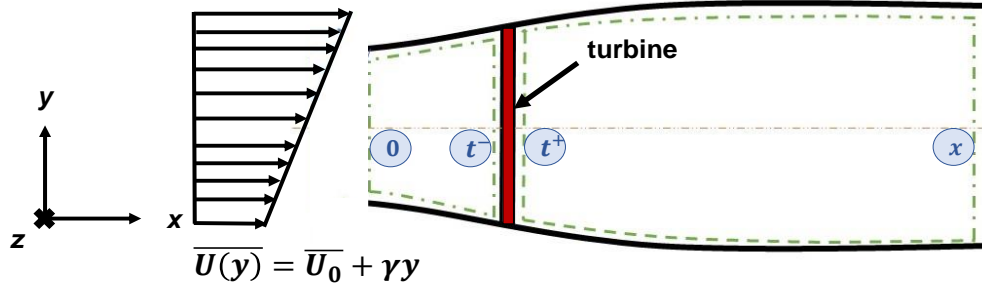


Figure 3.1: Representative section of a single turbine, operating in a non-uniform inlet velocity.

### 3.2.2. Implementation in the UWFLO Model

In this section, we extend the UWFLO model proposed in [16] to incorporate the shear effects on the total array flow field and power performance. The model given by Eq. (3.2.3) is valid for a single turbine operating in weak shear conditions, which are characterized by nearly constant values of $(\Xi, \Psi) \to 1$ (although our results show this assumption describes the strong shear limit with reasonable accuracy). We have extended the implementation of this model to the case of multiple turbines by combining it with the UWFLO model

developed by [16]. The UWFLO model computes the total power output of a farm by accounting for the momentum "shadowing" effect of upstream turbines on downstream devices. This is accomplished through an area overlap factor, which is used to weight the cumulative momentum removal effect of multiple overlapping wakes. If the assumption of $\Xi_1 \sim \Xi_4 \sim \Xi$, and $\Psi_1 \sim \Psi_4 \sim \Psi$ is made, the shadowing effect is not directly affected by the non-uniform velocity profiles, since the coefficients appear as weights in the momentum terms for each individual participating wake, and hence cancel out. Instead, Eq. (3.2.2) is used to compute the power of each turbine in the farm, but the incident velocity $\overline{U}_1$ (or in the general case, $\overline{U}_j$) is taken as the wake-interfered velocity from all the upstream turbines, computed according to the method outlined in the original UWFLO model. Finally, we note that in extending the UWFLO model to include the effects of shear described by Eq. (2.1.16), $\overline{U}_j$ has to be calculated locally for each turbine '$j$' as the $y$-average (across the turbine span) over the spatially varying shear profile. The solution for the streamwise velocities in the near- and far-wake regions is then given by Eq. (2.1.24).

In summary, there are three primary steps that must be carried out to implement the UWFLO model for non-uniform inlet flows: (1) include the near-wake region obtained by Eq. (2.1.24) in the description of the evolution of the mean streamwise velocity; (2) consider the mean local streamwise velocity profile approaching each turbine by spatially averaging in the $y$-direction, and across the turbine span; and (3) incorporate the effects of non-uniformities in the streamwise velocity profiles approaching each turbine by using the local values for $\Xi$ and $\Psi$ based on the upstream velocities for each turbine, in the expression for the power coefficient.

**3.3 Numerical Simulation Details**

The simulations reported in this chapter were performed using the STAR-CCM software, and employed the RANS methodology. The incompressible, 3D Navier-Stokes equations were solved using a finite-volume discretization and given by

$$\frac{\partial \bar{u}_i}{\partial x_i} = 0 \tag{3.3.1}$$

$$\rho \bar{u}_j \frac{\partial \bar{u}_i}{\partial x_j} = \rho \bar{f}_i + \frac{\partial}{\partial x_j} \left[ -\bar{p}\delta_{ij} + \mu \left( \frac{\partial \bar{u}_i}{\partial x_j} + \frac{\partial \bar{u}_j}{\partial x_i} \right) - \rho \overline{u_i' u_j'} \right]. \tag{3.3.2}$$

The unclosed Reynold stresses that appear in eq. (3.3.2) were solved using an SST $k - \omega$ [67] turbulence closure model, in which separate transport equations for turbulent kinetic energy ($k$), and specific dissipation rate ($\omega$) are evolved. The computation of the turbulent viscosity is modified to improve the turbulent shear stress term in the near-wall and far-field regions. A pressure outlet boundary condition was applied to the domain exit boundary, while an inlet velocity condition was enforced at the domain inlet, capable of accommodating different shear profiles. A prism layer mesh near the surface of the turbine was chosen to satisfy $\Delta \sim 2y^+$, where $y^+ \equiv \sqrt{\frac{yu_*}{v}}$, and $u_* = \sqrt{\frac{\tau_{y=0}}{\rho}}$ is the friction velocity and $\tau_{y=0}$ is the wall shear stress. A detailed grid convergence study was performed at several mesh sizes to determine the size of the converged mesh for use in the production simulations. The complete list of RANS simulations reported in this study is given in Table 3.1.

Table 3.1: Summary of RANS simulations of single-turbine and array configurations.

| Case number | Configuration | Shear profile | Non-dimensional shear rate |
|---|---|---|---|
| 1 | Single turbine | Linear | 0.01 |
| 2 | Single turbine | Linear | 1.0 |
| 3 | Two turbine tandem | Linear | 0.01 |
| 4 | OCT array (scattered) | Linear | 0.01 |
| 5 | OCT array (scattered) | Linear | 0.01 |
| 6 | OCT array (scattered) | Logarithmic | _ |

## 3.4 Single Turbine Operating in Non-uniform Flow

A non-uniform velocity profile was defined at the inlet boundary using the function $U(y) = U_0 + \gamma y$, where $U_0$ is the velocity at the turbine hub-height $y = 0$, and the parameter $\gamma = \frac{dU}{dy}$ is the shear rate in $s^{-1}$. The value of $\gamma = 0.001 \ s^{-1}$ was chosen so that the non-dimensional parameter $\gamma \frac{D_t}{U_0} = 0.01$ in our simulations matched the corresponding weak shear conditions for a typical turbine deployed in the ocean [2]. The purpose of the simulations presented in this section is to validate the single-turbine shear model of [66], which can then be used to interpret the array results.

Before presenting the simulation results, we briefly describe the methodology used to compute local spatial averages of the mean, streamwise velocity approaching each turbine, and corresponding local values of the Coriolis and Boussinesq coefficients for evaluating the model. The turbine area is divided into approximately rectangular strips (figure 3.2),

while the mean, streamwise velocity is averaged over each rectangular window to give the non-uniform velocity approaching each turbine $\overline{U(y)}$. Corresponding Coriolis and Boussinesq coefficients can be computed directly from integrating $\overline{U(y)}$ according to definition presented in § 3.2.1. To compute the total power generated by each turbine in a non-uniform flow, we first compute the power extracted from flow passing through each of the '$n$' rectangular area elements in figure 3.2. The power extracted from flow through each rectangular strip '$l$' is given by

$$P_l = \Delta p_l U_l A_l, \tag{3.3.3}$$

where $\Delta p_l$ is change of pressure across the area element '$l$', and $U_l$ is the streamwise velocity at that area element. The total power of the turbine is obtained from the summation:

$$P = \sum_{l=1}^{n} P_l \quad . \tag{3.3.4}$$
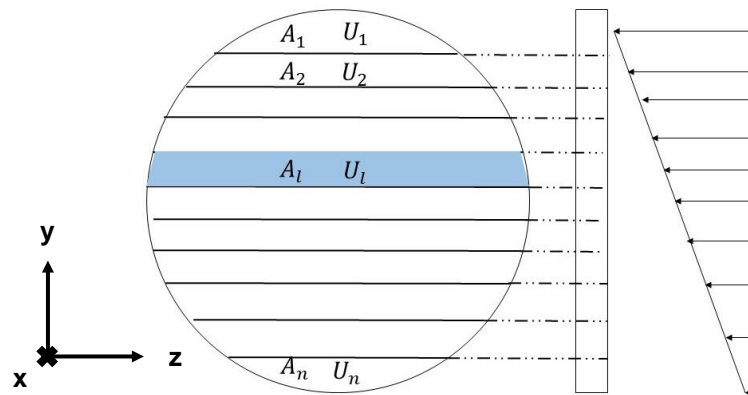


Figure 3.2: Discretization of turbine span into 'n' area elements for computing local averages of the mean streamwise velocity approaching a turbine.

Figure 3.3 is a plot of the power coefficient for a single turbine at different induction factors computed using the approach described above, and shows good agreement between the

model [Eq. (3.2.3)] and the RANS simulations. In Fig. 3.3, we also plot the $C_p$ curve for

the uniform inflow velocity case, given by Eq. 3.2.4. For this weak shear case ($\gamma\frac{D}{U_0} = 0.01$),

both Eqs. (3.2.3) and (3.2.4) for the non-uniform and uniform velocity results, are in good

agreement with the RANS data. Similarly, Fig. 3.4 is a plot of (Case 1) the local power

coefficient across the turbine for uniform velocity, and weak shear at an induction factor

of 0.4. The weak shear has little impact on local power coefficient near the root region,

while reaching maximum values near the hub height.
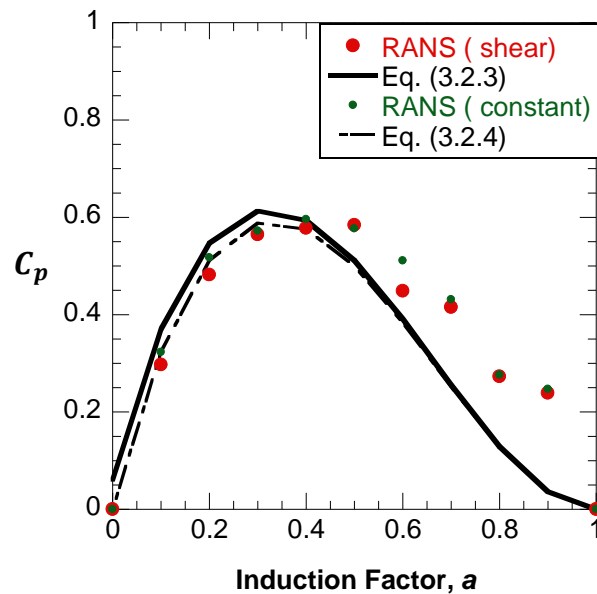
Figure 3.3: Plot of the power coefficient against the induction factor, for a single turbine operating in a weak shear environment ($\gamma\frac{D}{U_0} = 0.01$). Comparison of RANS simulations with the model from [66].
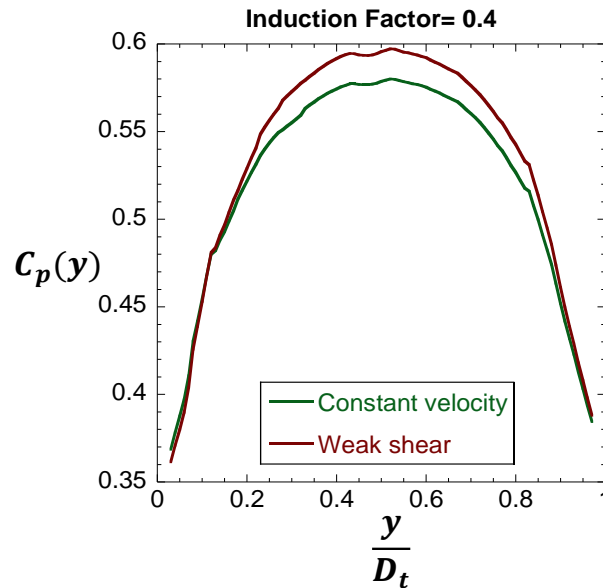
Figure 3.4: Variation of local power coefficient across the turbine for uniform velocity, and weak shear for Case 1.

### 3.4.1. Variation of Shear Rate and Extension to Strong Shear

RANS simulations in which the non-dimensional shear rate was varied to give $\gamma \frac{D}{U_0} = 0.01$, 0.05, 0.1, 0.5, and 1.0 were performed using STAR-CCM, and the results are compared with the non-uniform velocity model [66] described in § 3.2.1. We note that the $\gamma \frac{D}{U_0} \to 1$ limit represents strong shear typically observed in wind farms where the turbines operate in the strong vertical gradients of velocity found within the atmospheric boundary layer. Such strong shear conditions can also exist locally in OCT arrays, where a downstream turbine is operating in the wake of an upstream device.

The streamwise velocity contours from the simulations with strong shear (Case 2) across a single turbine is shown in Fig. 3.5, and shows significant asymmetry in the wake structure. Figure 3.6 is a plot of $C_p$ against the non-dimensional shear rate for a single turbine operating at an induction factor of 0.4. In this case, for the uniform velocity, Betz law predicts $C_{p,Betz} = 0.59$, and by increasing the shear rate both CFD and model both report

$C_p > C_{p,Betz}$ according to eqs. (3.2.3) and (3.2.5) and the accompanying analysis. For example, for $a = 0.4$ and under the strong shear conditions ($\gamma \frac{D_t}{U_0} = 1$), the mean flow velocity profiles correspond to $\Xi = 1.206$ and $\Psi = 1.069$. Then, using eq. (3.2.3) gives for $C_p = 0.72$ in agreement with Figure 3.6, and greater than $C_{p,Betz}$.
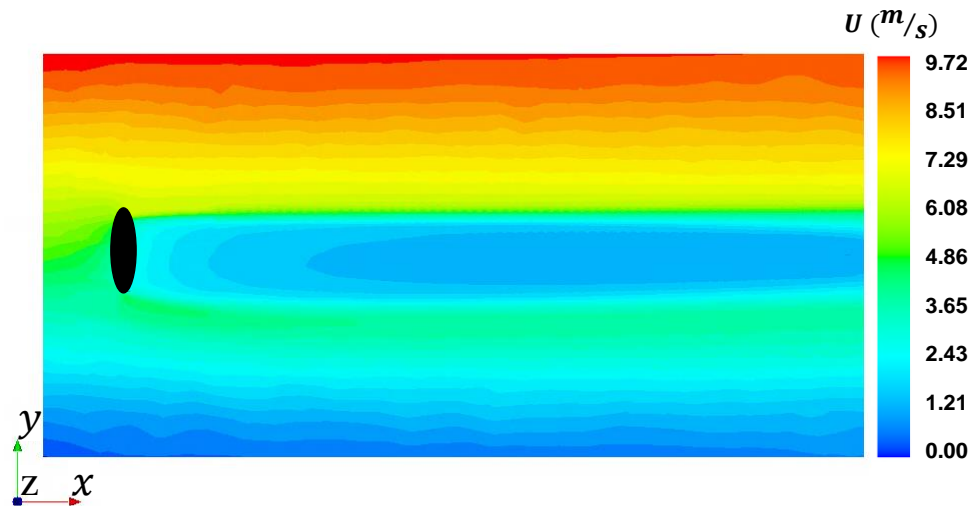


Figure 3.5: Contours of streamwise velocity from RANS simulation for $\gamma \frac{D}{U_0} = 1$ (Case 2).
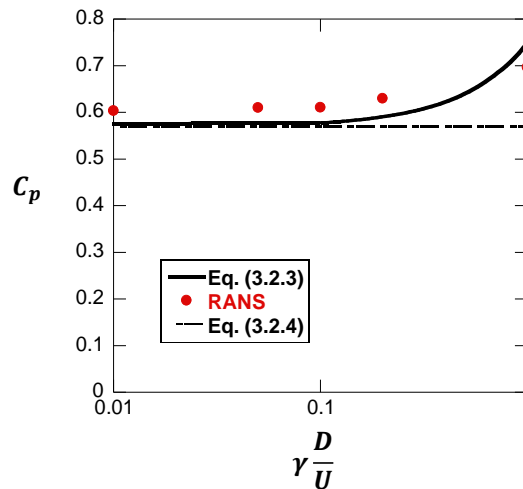


Figure 3.6: Variation of power coefficient with non-dimensional shear rate (a = 0.4) – comparison of RANS data with models for non-uniform and uniform velocities.

### 3.5 OCT Arrays Results

The OCT array modeling framework for shear inlet flow presented in § 3.2 is validated here against RANS data over different configurations and shear rates and profiles.

*3.5.1. Two Turbine Configuration*

The purpose of the simulation presented in this section is to isolate the wake interaction between a tandem pair of an upstream and downstream turbine aligned with the flow with a separation distance of $\frac{x_{12}}{D_t} = 10$, as shown in Fig. 3.7 (Case 3). Contours of the streamwise velocity ($U$) are presented in Fig. 3.7, and show significant wake recovery as the flow approaches the downstream turbine. The simulations were performed with a non-dimensional shear rate of $\gamma \frac{D}{U_0} = 0.01$, representing the weak shear limit. In this configuration, the local velocities averaged over the turbine span for both the upstream and downstream turbines are the same, since the turbines are aligned to the flow direction and at a separation distance where the flow has fully recovered. As a result, the modified UWFLO model is not used in the comparison with RANS data – instead, the shear flow model given in eq. (3.2.3) is used directly without accounting for upstream turbine overshadowing effects. Results from the RANS simulation are compared with streamwise velocity ($U$) scaled by the upstream velocity ($U_0$) computed by the model eq. (3.2.3), and show good agreement in Figure 3.8. In Figure 3.9, we compare the relative power extracted by each turbine in the tandem configuration computed using model eq. (3.2.3) and the corresponding RANS data. The relative powers from the shear model is in good agreement with the simulation results.
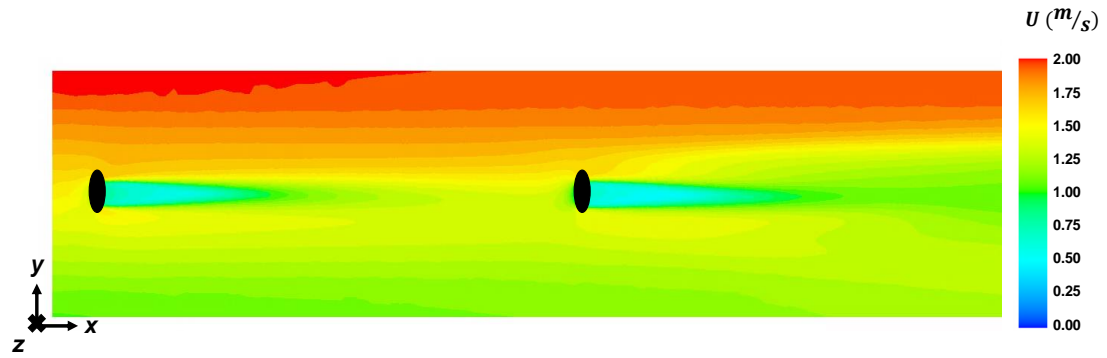
Figure 3.7: Contours of streamwise velocity associated with shear flow past two turbines in tandem (Case 3).
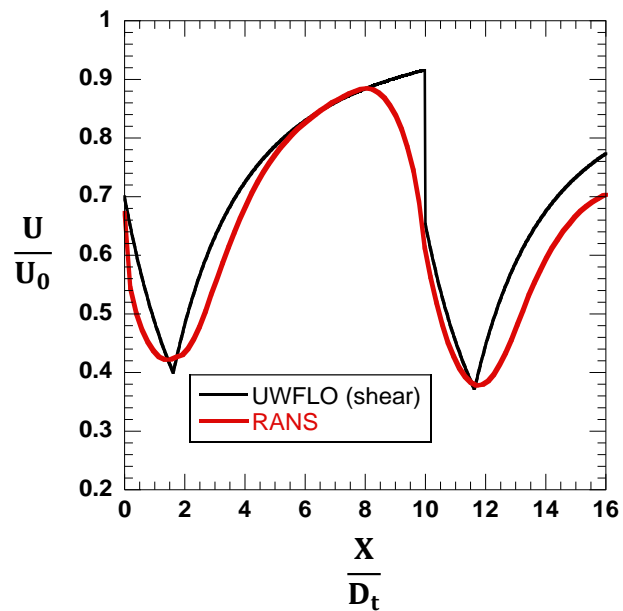


Figure 3.8: Comparison of $\frac{U}{U_0}$ vs. $\frac{x}{D_t}$ from RANS data and the model of [66] for shear flow past a turbine tandem (Case 3).
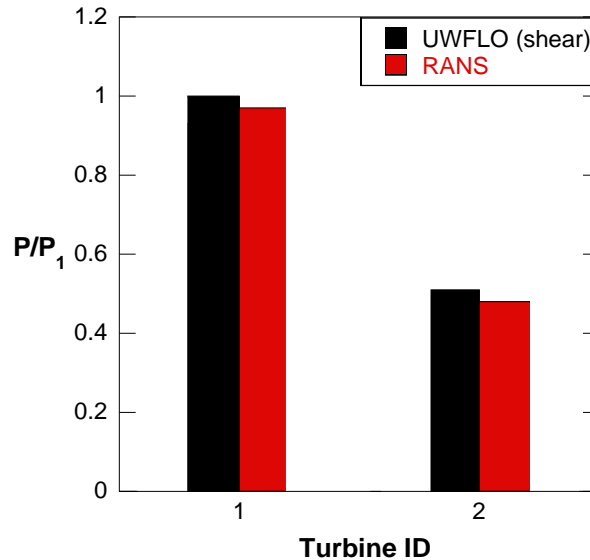
Figure 3.9: Relative power for each turbine in a tandem configuration of turbines in shear flow (Case 3) – RANS comparison with model eq. (3.2.3).

### 3.5.2 Multiple Turbine Arrays

In this section, the proposed analytic model for array power as a function of different shear profiles has been validated using RANS for different layouts and conditions. In Case 4, turbines were arrayed as shown in Fig. 3.10 (a), with the downstream turbines likely to experience significant wake-shadowing and near-wake effects, while exposed to a non-dimensional weak shear rate $\gamma\frac{D}{U_0} = 0.01$. The power output from each turbine in the simulation was computed using the modified UWFLO model (§ 3.2.2.), and compared with the model in Fig. 3.10(b). For each turbine, the local upstream velocity, along with the coefficients $\Xi$ and $\Psi$ were computed in a region $2D_t$ upstream of that device, and used in the model equations. For all turbines included in the simulation, the model prediction for power output is in good agreement with the simulation results to within an rms error of 4.8%.
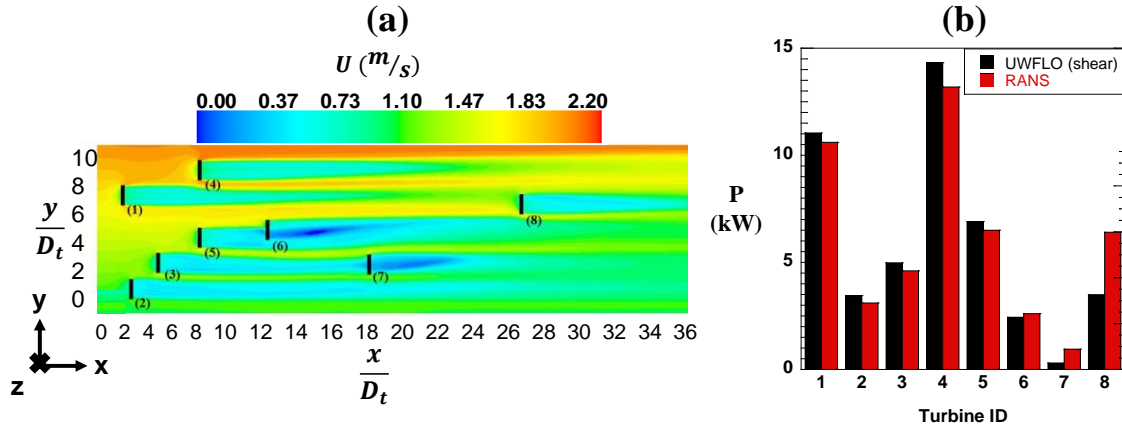
Figure 3.10: Contours of (a) streamwise velocity and (b) power for each turbine for Case 4, with a linear shear profile, showing comparison between modified UWFLO model and RANS data.

In Figure 3.11, results from the RANS simulations are compared with turbine power computed from the wake velocity predicted by UWFLO model with uniform inlet velocity. Results from the RANS simulations of the array configuration shown in Figure 3.12 (a) correspond to a linear inlet velocity profile with a non-dimensional shear rate $\gamma \frac{D}{U_0} = 0.01$ (Case 5). In figure 3.13, streamwise velocity contours from RANS calculations of the same configuration, but with a logarithmic inlet velocity profile (Case 6) are shown. The logarithmic profile for Case 6 was taken to be $U(y) = U_0 + \frac{u_*}{k}\ln(\frac{\frac{y}{D_t}}{y_0})$, with $U_0 = 1 \frac{m}{s}, \frac{u_*}{k} = 0.1 \frac{m}{s}$, and $y_0 = 0.00045$ to match the Coriolis and Boussinesq coefficients of the corresponding linear shear profile (Case 5). The modified UWFLO model with shear effects was once again computed with the local values of velocity, $\Xi$ and $\Psi$ obtained by spatially averaging over a window of dimension $2D_t$ ahead of the turbine. In Figure 3.12(b) and Figure 3.13(b), we plot the power for all the turbines in the array from the RANS and the model calculations. The simulation results and model predictions for turbine power are in good agreement, with an rms error of 7.3% and 2.8%, for the linear and logarithmic

shear profiles respectively. As shown in Figures 3.12 (b) and 3.13 (b), the functional form

of the shear profile affects average power generation. Both the model and simulation results

show differences in generated power between the linear and logarithmic shear profiles.
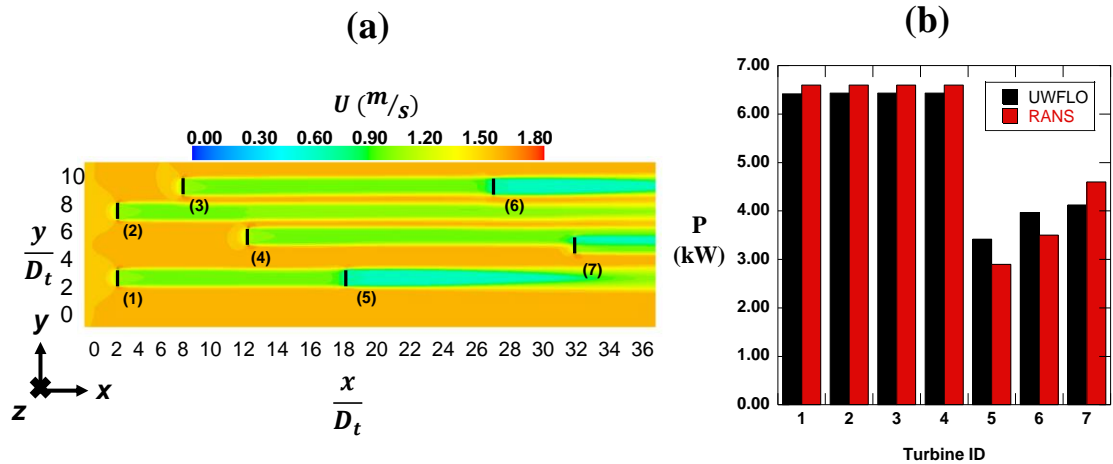


Figure 3.11: Contours of (a) streamwise velocity and (b) power for each turbine for uniform velocity.

**(a)** **(b)**
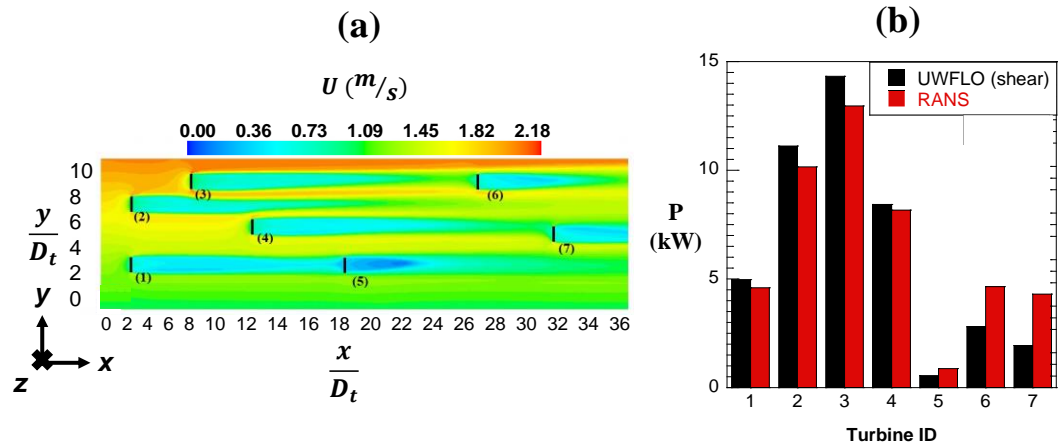


Figure 3.12: Contours of (a) streamwise velocity and (b) power for each turbine from the modified shear model and RANS: Results from Case 5 with linear shear profile.

**(a)** **(b)**
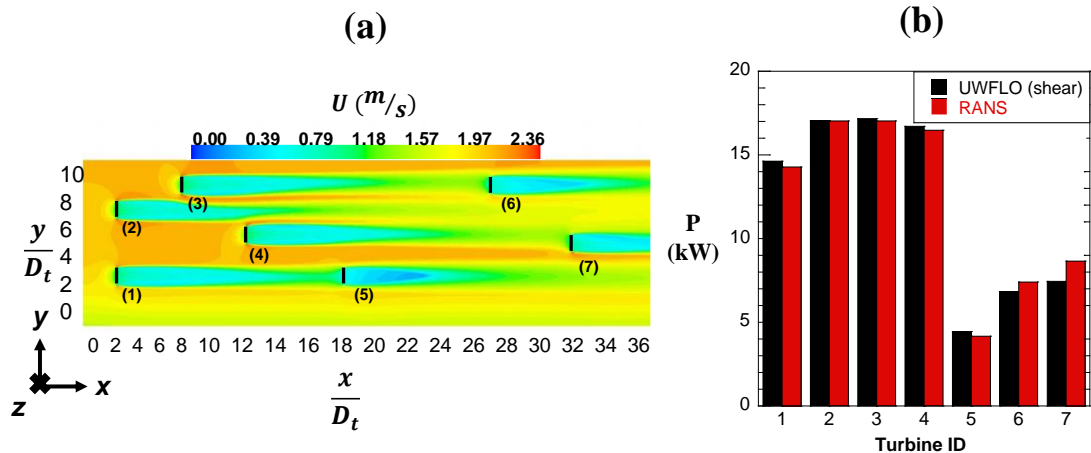


Figure 3.13: Contours of (a) streamwise velocity and (b) power for each turbine from the modified shear model and RANS: Results from case 6 with logarithmic shear profile.

## 3.6 Conclusion

In this chapter, we have investigated the behavior of single turbines and OCT arrays, when operating in an inlet shear flow. We have extended a recently developed low order model for a single-turbine in shear flow [66], to account for wake interactions occurring in an array of turbines, using the UWFLO [16] framework. The development of a low-order wake interaction model for non-uniform shear flow described here is expected to impact

the deployment and operational strategies of planned OCT arrays. The model was validated by comparing with RANS simulations of isolated turbines, and OCT arrays, and across a wide range of shear rates and shear profiles. Thus, the OCT array modeling framework is capable of handling both the weak and strong shear limits, as well as different functional forms for the shear profile.

The modified UWFLO model was also compared with RANS simulations of different OCT configurations including tandem and staggered configurations. Such models maybe used in accurate economic forecasting of the performance of planned OCT arrays, by modeling the effects of realistic flow conditions. Such improved predictive capabilities are essential to industry stakeholders in planning OCT array design and deployment, and will help spur investment in the blue economy. While the model has been applied in this work to OCT performance, the behavior of wind turbine arrays when operating in the shear flow conditions of the atmospheric boundary layer can also be described through the ability to account for different functional forms of the shear profile.

CHAPTER 4: CHARACTERIZING THE INTERACTION OF OCT ARRAY WAKE
TURBULENCE WITH THE BACKGROUND OCEAN STRATIFICATION

This chapter is aimed at addressing the effect of spatially localized turbulence generated

by an extensive array of OCTs on the background flow. Results from detailed LES

calculations are reported, while the simulations were based on an idealized representation

of the oceanic density stratification through the definition of a new unit problem. The

primary objectives of this study are to understand the transport of wake turbulence from

OCT arrays, and its effects on the background stratification.

**4.1 Background**

The GS plays a critical role in mediating the transport of essential nutrients from the

nutrient-dense deep ocean layer to the surface layers inhabited by Sargassum and

phytoplankton [76]. Turbulence generated by arrays of OCTs can impact the transport of

such nutrients, and influence the overall nutrient budget in adverse ways. By characterizing

the turbulent transport through the background stratification, our results can be used in

estimating the environmental impact of planned OCT arrays.

These results will also positively impact the skill of ocean general circulation models

(OGCMs) currently used in several modeling codes in two ways: (i) Code frameworks such

as ROMS [77] or HYCOM [26] employ the widely-used K-profile parametrization (KPP)

approach to describe downgradient transport of turbulence in the different ocean layers,

and to close the turbulence equations. The turbulent viscosity is thus taken to be a function

of $Ri$, although the precise functional form is uncertain [27]. Results from our simulations

at different $Ri$ and at scales currently inaccessible to OGCM codes could thus be used to

clarify this dependence and improve the accuracy of such codes. (ii) Similarly, the KPP

turbulence closures will need to be improved in response to the introduction of arrays of turbines. Currently, OGCMs are typically limited to a maximum spatial resolution of ~1 km, which is insufficient to capture the effects of the OCT arrays, which are likely to span a few hundred meters. We expect results from our simulations will be used to refine the KPP models to account for the generation (through subgrid production terms) and transport of the wake turbulence.

To address the above questions, we first performed a baseline simulation with no background stratification to establish a decay power law for turbulent intensity in the absence of any stratification. Building on the baseline case, simulations in which the gradient Richardson number was systematically varied were performed, and the corresponding growth/decay rate of the turbulent kinetic energy ($dk/dt$) was measured. A new unit problem was defined which ensured the Richardson number remained constant throughout the vertical extent of the computational domain, and did not introduce an additional length scale that could interact with the turbulence.

From our simulations with $Ri > 0.25$, we found the turbulent kinetic energy at the centerline decayed in the LES simulations. When $Ri < 0.25$, the LES simulations showed that perturbations grew, since they were amplified by shear to a greater extent than suppressed by buoyancy. This turbulence growth is divided in to two phases: an initial unstable phase, and a late-stage, stable phase that occurs as the turbulent mixing increased the local Richardson number past 1/4. Simple power law expressions for the evolution of the turbulent kinetic energy, and the corresponding spatial footprint of the turbulence as a function of the Richardson number was developed. To demonstrate the applicability of such power law expressions in determining the footprint of turbulence in the actual GS

environment, we applied the models to estimate the turbulence decay lengthscale at different $Ri$ based on data from GS observations.
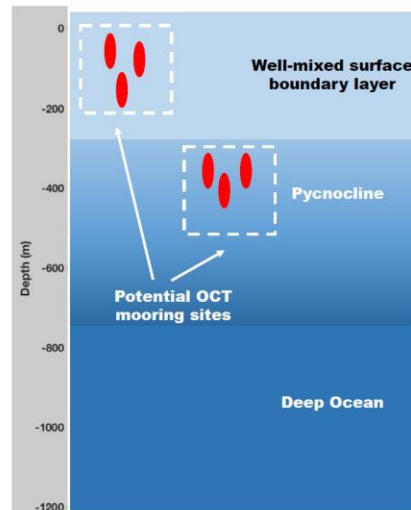


Figure 4.1: Schematic showing different ocean layers in design and planning of OCTs.

## 4.2 A New Unit Problem for Studying Stability of Stratified Flows

In an effort to improve on earlier studies of the stability of background stratification to turbulent perturbation, we have formulated a new unit problem where the $Ri$ number is uniformly constant throughout the vertical extent of the simulation domain. In earlier studies, the $Ri$ number itself could vary along the direction of gravity, thus introducing an artificial length scale that may interact with the turbulent length scales. In addition, such profiles can lead to a discrepancy between the gradient and bulk $Ri$ numbers, further complicating the analysis. To remedy this, the following approach is taken. An average velocity is defined using

$$U(y) = V tanh(\frac{y}{H}) \qquad (4.2.1)$$

The density profile required for a corresponding uniform $Ri$ number can be determined from

$$Ri = -\frac{g}{\rho(y)} \frac{d\rho(y)/dy}{\left(\frac{dU(y)}{dy}\right)^2} \qquad (4.2.2)$$

and integrating

$$\int_{\rho_0}^{\rho(y)} \frac{d\rho}{\rho} = -\frac{Ri}{g} \int_{-y_{limit}}^{y} \frac{dU(y)^2}{dy} \, dy \qquad (4.2.3)$$

to give for $Ri(y)$,

$$\rho(y) = \rho_0 exp\left\{-\frac{Ri}{g}\left(2 + \cosh\left(\frac{2y}{H}\right)\right) sech^2\left(\frac{y}{H}\right) tanh\left(\frac{y}{H}\right)\right\}_{-y_{limit}}^{y} \qquad (4.2.4)$$

In eqs. (4.2.1) – (4.2.4), $H$ represents a lengthscale associated with the stratification, while $\rho_0$ and $u_0$ are reference values of density and velocity at the lower boundary of the simulation domain $y_{limit}$. The above equation represents a new unit problem, where the stability of linear, nonlinear, and turbulent perturbations may be investigated. The stratification profiles from this problem formulation are shown in Fig. 4.2, and show a $Ri$ number that remains constant through the mixing layer. In our simulations investigating the parametric dependence on turbulent transport on the Richardson number, the idealized stratification profile developed here has been used. Power laws for turbulent transport deduced from such simulations were then applied to measured velocity and density stratification profiles from the GS current [4].

**(a)** **(b)** **(c)**
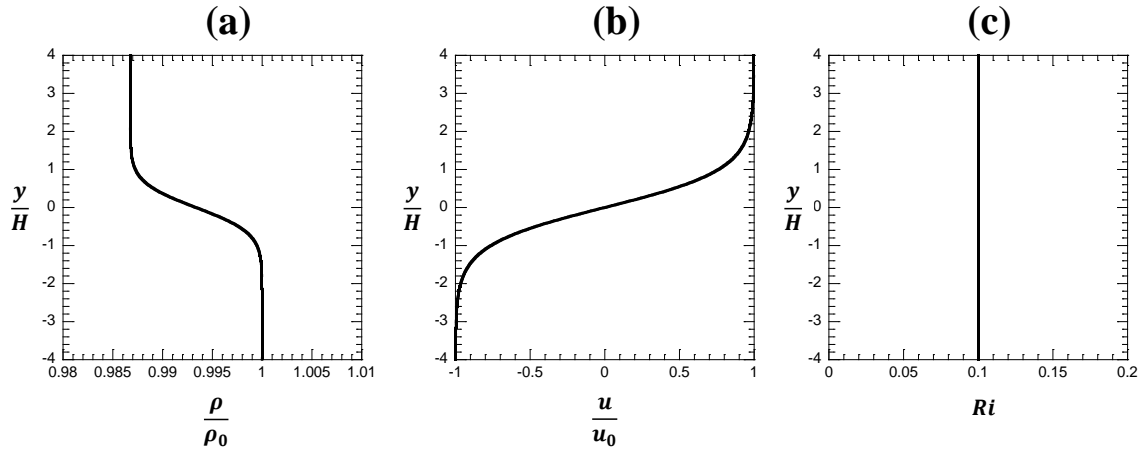
Figure 4.2: Background stratification profiles of (a) density, (b) averaged velocity, and (c) Ri number associated with the proposed unit problem.

## 4.3 Numerical Simulation Details

The above density and velocity profiles were used as background stratification profiles in LES performed using the STAR-CCM software. The 3D simulations were performed in a rectangular domain of dimensions (8H×8H×8H) (Fig. 4.3(a)), with mesh resolution ranging from $8 \times 10^6$ - $3.2 \times 10^7$ (Fig. 4.3(b)). The turbulent statistics from the simulations were averaged over a period covering 100 eddy turnover times, associated with the timescale $\frac{H}{U_0}$. Two types of velocity perturbations were superposed on the background flow: (i) a synthetic turbulence field satisfying measured ocean turbulence properties (spectra, anisotropy, and frequency ranges) generated using the approach given in [56]. The simulations were performed with periodic boundary conditions in the cross-stream ($y$-) directions, outflow conditions in the streamwise ($x$-) direction, while the top and bottom boundaries were treated as free-slip surfaces. The simulation domain along with boundary conditions are shown in fig.4.3(a), where the mean velocity and density profiles have been superposed.
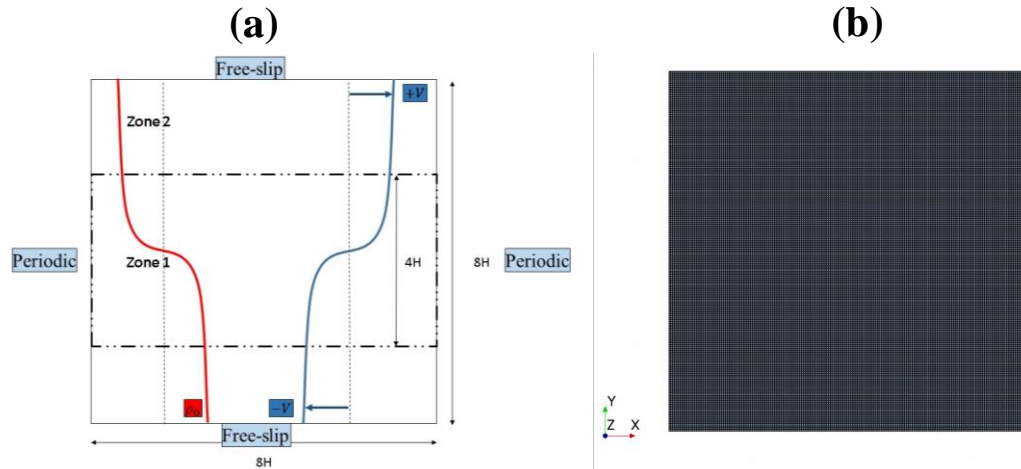
Figure 4.3: Simulation (a) domain and boundary conditions, and (b) mesh distribution.

We used the approach detailed in Appendix A.2, and adopted and modified from [56] in generating a detailed spatiotemporal flowfield representing the background ocean turbulence, which was then fed into the inlet boundary in our simulations. The properties of the turbulent flow field were defined to match the properties of GS observations of ocean turbulence [4], including the ambient turbulence intensity ($I_t$), minimum and maximum frequencies ($f_{min}$, $f_{max}$), the degree of anisotropy between velocity components, and mean flow speed $\overline{U}$. The following values for these parameters were assumed: $\overline{U} = 1$ m/s, $I_t =$ 10% (comparable with the values reported in the GS), $f_{min} = 0.01$ Hz, and $f_{max} =$ 10 Hz.

Mean shear and density profiles were defined as functions of the y-coordinate using the expressions developed in § 4.2.2, while the turbulent region was confined to the middle section ($y \leq |H|$). The ocean density gradient was specified through a temperature gradient in the simulations, using a typical seawater equation of state, and as a polynomial in temperatures. Turbulent perturbations representing broadband flow were generated using the methodology described in the appendix A.2, and imposed on the background

stratification. Several cases were studied to investigate the evolution of the turbulent perturbations, while the complete list of LES simulations is given in Table 4.1.

Table 4.1: Summary of LES simulations of turbulence propagation through the ocean stratification.

| Case number | Configuration | $Ri$ |
|:---:|:---:|:---:|
| 1 | No stratification | — |
| 2 | Stable stratification | $Ri > 0.25$ |
| 3 | Unstable stratification | $Ri < 0.25$ |
| 4 | GS observation | $0 < Ri < 1000$ |

## 4.4 Results

### 4.4.1. Simulations with zero stratification

These simulations were performed to establish a baseline, and to develop a power law for the decay of turbulence intensity in the absence of any stratification. The simulations also serve to quantify the extent of physical and numerical dissipation associated with the LES sub-grid model. In Fig. 4.4, the decay of centerline kinetic energy is plotted against time non-dimensionalized $(\frac{t}{l/u})$, where $t$ (s) is the real-time, $l$ (m) is the length scale of turbulence, and $u$ (m/s) is the turbulent velocity of simulations, by a turbulent eddy turnover time as defined by the initial conditions. The turbulent kinetic energy was computed from the averaging over a time series spanning $100\tau$. We fit a generic decay power law to this data to characterize the 'footprint' of turbulence in a zero-stratification layer, by fitting the simulation data to

$$\frac{ke(\tau)}{ke(0)} = B(\tau - \tau_0)^n \tag{4.4.1}$$

where $\tau_0$ represents a virtual origin effect that might depend on the initial conditions associated with the turbulent state at $\tau = 0$ (not explored here), and $n$ is the power law exponent. We find from simulation data, $B$= 32, $n$ = 1.6, and $\tau_0$ = –5.5 consistent with expected behavior for decaying turbulence [78]. Based on this power law, the extent of a turbulent footprint in an unstratified flow can be estimated as the distance over which the initial turbulent kinetic energy will decay to 1% of its original amplitude ($ke(0)$). Applying the criterion based on eq. (4.4.1) to the results from this simulation, the turbulent footprint in the absence of stratification was estimated as ~149$l$, where $l$ is an initial turbulent length scale characteristic of the initial conditions. In practice, $l$ could range from the diameter of a single turbine (~ 50 m) to the wake length scale for an array of turbines (~500–1000 m).
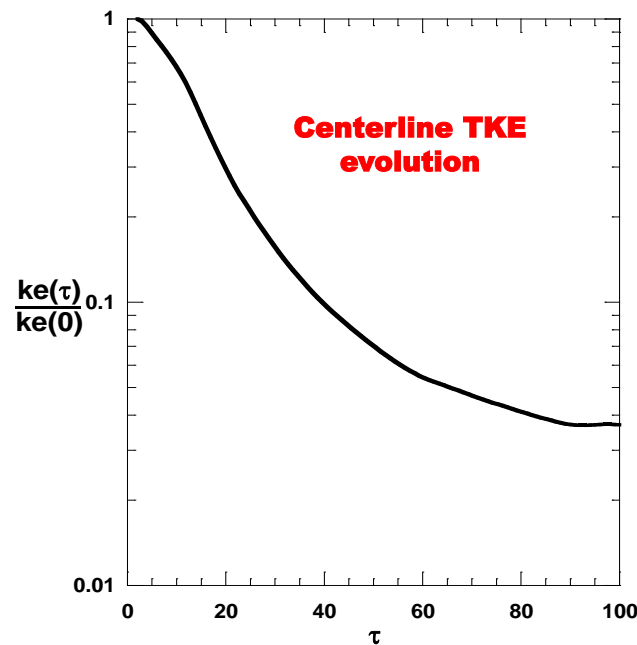


Figure 4.4: Evolution of centerline turbulent kinetic energy for baseline simulation (Case 1) with no shear or stratification.

*4.4.2. Stratified Flow (Ri > 0.25)*

For $Ri > 0.25$, we find the turbulent kinetic energy at the centerline decayed in the LES simulations, as shown in Fig. 4.5 ($Ri = 1$) and Fig. 4.6 ($Ri = 2$). Fitting the data to the above power law, we found $B = 9.1$, $n = -2.2$ and $\tau_0 = -0.7$ for $Ri = 1$. When the simulations were repeated for $Ri = 2$ a similar qualitative behavior was observed, while the decay coefficients were determined to be $B = 7.1$, $n = -2.01$ and $\tau_0 = -0.6$. These coefficients were found to depend weakly on the $Ri$, and this dependence was included in our model as a fitting coefficient. Based on this power law, a turbulent footprint can be estimated as the distance over which the initial turbulent kinetic energy will decay to 1% of its original amplitude. For this case, the footprint was estimated as ~$21l$, consistent with a faster decay for the stratified case.
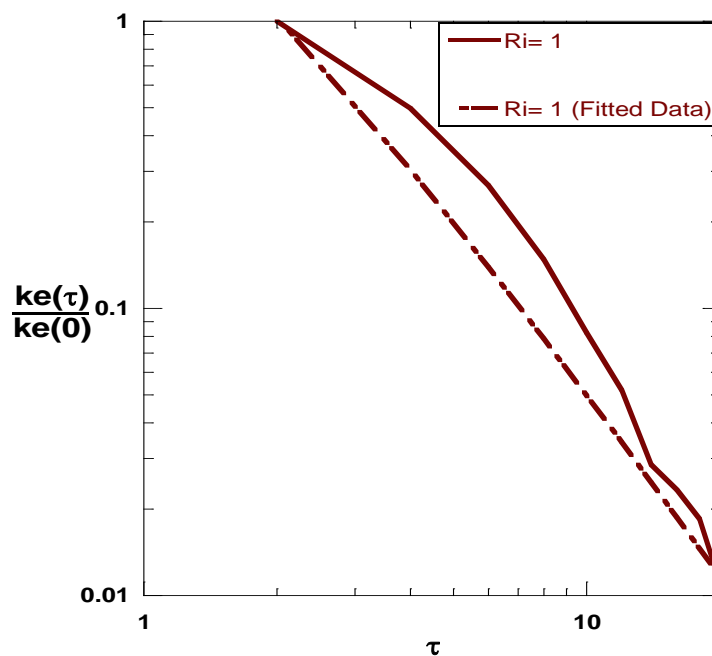


Figure 4.5: Results from stably stratified simulation (Ri = 1) (Case 2) showing decay of centerline kinetic energy from LES and model fit to eq. (4.4.1).
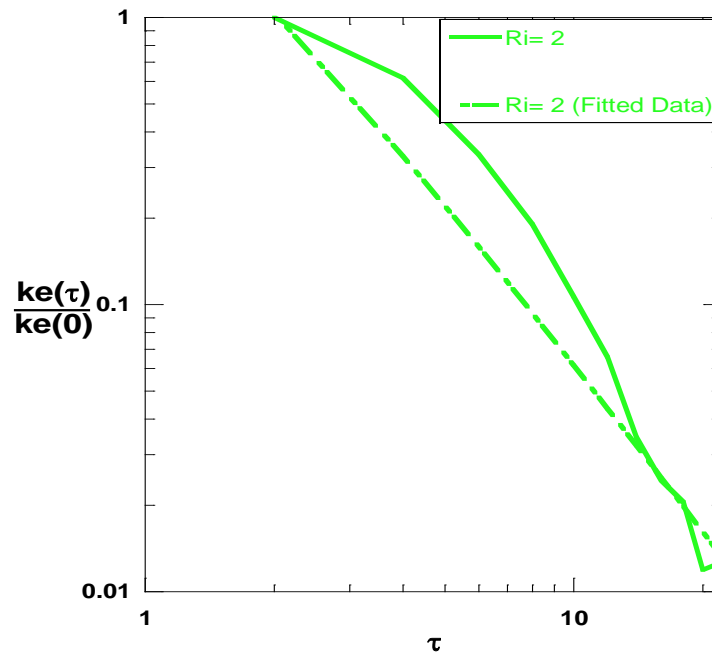
Figure 4.6: Results from stably stratified simulation (Ri = 2) (Case 2) showing decay of centerline kinetic energy from LES and model fit to eq. (4.4.1).

*4.4.3. Stratified Flow (Ri < 0.25)*

When $Ri < 0.25$, we found from the LES simulations that perturbations grew, as they were amplified by shear more than they were suppressed by buoyancy. However, the flow dynamics is complex, where the unstable growth lasts only until centerline perturbations reach the edge of the mixing layer. This is evident in the evolution of the centerline $Ri$ number, shown in Fig. 4.7 (b). Even for an initial $Ri < 0.25$ configuration, the mixing due to turbulence results in a homogenization within the mixing layer gradually increasing the $Ri$ number until it reaches a stable value of $Ri > 0.25$. Thus, even for an initially unstable configuration in which the mixing layer depth is finite, the mixing due to shear-driven turbulence will homogenize the layer in finite time, resulting in self-stabilization. However, for an infinite stratification layer, we expect the mixing layer will continue to remain

unstable. In fig. 4.7, we also plot the evolution of the turbulent kinetic energy for the marginally stable case ($Ri = 0.25$), where the kinetic energy exhibits an oscillatory behavior likely due to the presence of internal waves.
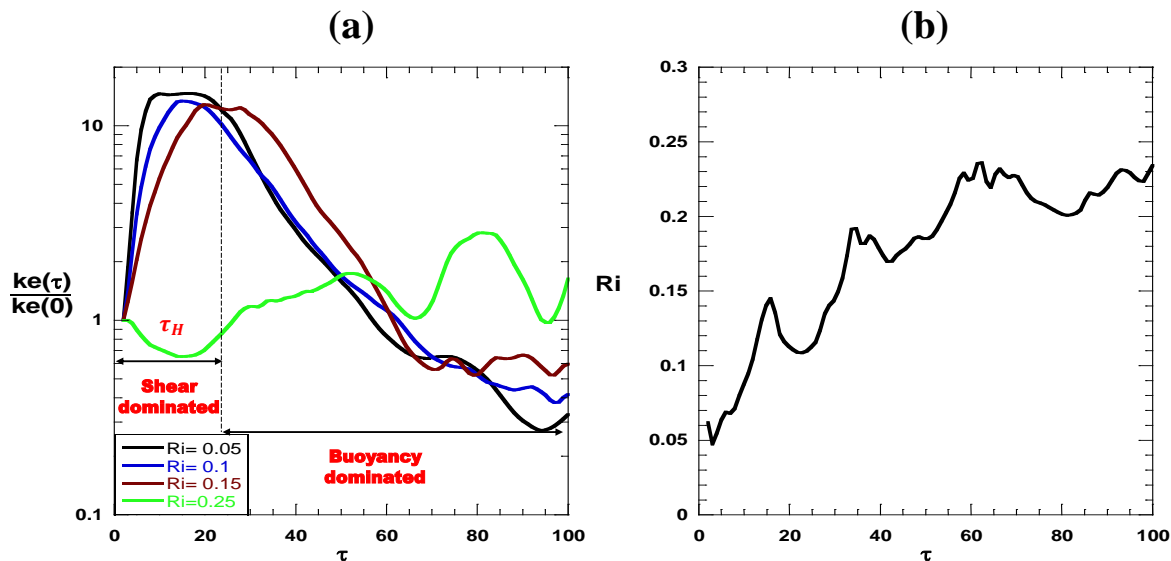


Figure 4.7: Evolution of (a) centerline kinetic energy for different Ri < 0.25, and (b) evolution of centerline Ri number for simulation with $Ri_0 = 0.05$ (Case 3).

Thus, for an unstable, finite stratification layer, turbulence growth may be divided in to two phases as shown in figure 4.7 (a): an initial unstable phase that lasts for $\tau_H$, and a final stable phase after the turbulent mixing has increased the $Ri$ number past 1/4. During the initial unstable phase, shear is dominant and amplifies the turbulent kinetic energy thus contributing to the turbulent production terms. However, the increased turbulence also mixes fluid packets that previously existed at different layers of stratification, thus effectively increasing the Richardson number. Thus, a second phase of kinetic energy evolution is observed, which is dominated by buoyancy stratification.

Based on these findings, an estimate for the footprint of turbulence case be modeled from modifying eq. (4.4.1) for any value of initial Richardson number. When $Ri > 0.25$, eq.

(4.4.1) is used as the decay law. Applying the criterion of centerline TKE decaying to 1 % of its initial value, eq. (4.4.1) can be rewritten as

$$\tau_{1\%} = \tau_0 + \left(\frac{0.01}{B}\right)^{1/n},$$ 
(4.4.2)

where as before the coefficients were determined from fitting to LES data. Then, applying the Taylor hypothesis to eq. (4.4.2), the spatial footprint of turbulence can be written as

$$\frac{x_{1\%}}{l} = \frac{V}{u'}\left\{\tau_0 + \left(\frac{0.01}{B}\right)^{1/n}\right\},$$ 
(4.4.3)

where $\tau_0$, $B$, and $n$ were taken as functions of the Richardson number, and the functional form was obtained from fitting to simulation data. When $Ri < 0.25$, the initial shear-dominated phase over a duration of $\tau_H$ must be included so that the corresponding equation for the decay length is given by

$$\frac{x_{1\%}}{l} = \frac{V}{u'}\left\{\tau_H + \tau_0 + \left(\frac{0.01}{B}\right)^{1/n}\right\},$$ 
(4.4.4)

where $\tau_0$, $\tau_H$, $B$, and $n$ were taken to be functions of $Ri$ and obtained from fitting to the simulations.

### 4.4.4. Estimating the Footprint of Turbulence from GS Observations

In this section, we demonstrate how the models developed based on LES data can be applied to observational measurements of the ocean stratification, to estimate the potential footprint of a single turbine, or an array of OCTs. The observational data were obtained from [4], and included mean density and velocity profiles as functions of the vertical coordinates. The data is gathered for 3-year-and-9-month time series of currents, salinity, and temperature measurements from a mooring that contains a 150-kHz and 130-kHz at depths of 40 and 75 m below the surface. The calculated shear squared and density profiles

along the Cape Hatteras Transect and accompanying buoyancy frequencies at each ADCP and CTD cast measurements obtained. From the velocity and density data, the local Richardson number was computed along with the model coefficients $\tau_0$, $B$, and $n$ which are functions of $Ri$. By applying the models to the observational data, estimates of the 1% footprint were obtained as shown in Figs. 4.8 and 4.9. When the local Richardson number was larger than 0.25 indicating a stable region, we applied the simple form of the model eq. (4.4.3). In contrast, when the local Richardson number was initially below the stability threshold of 0.25, the modified equation (4.4.4) accounting for both the shear- and buoyancy-dominated phases of the flow was applied.
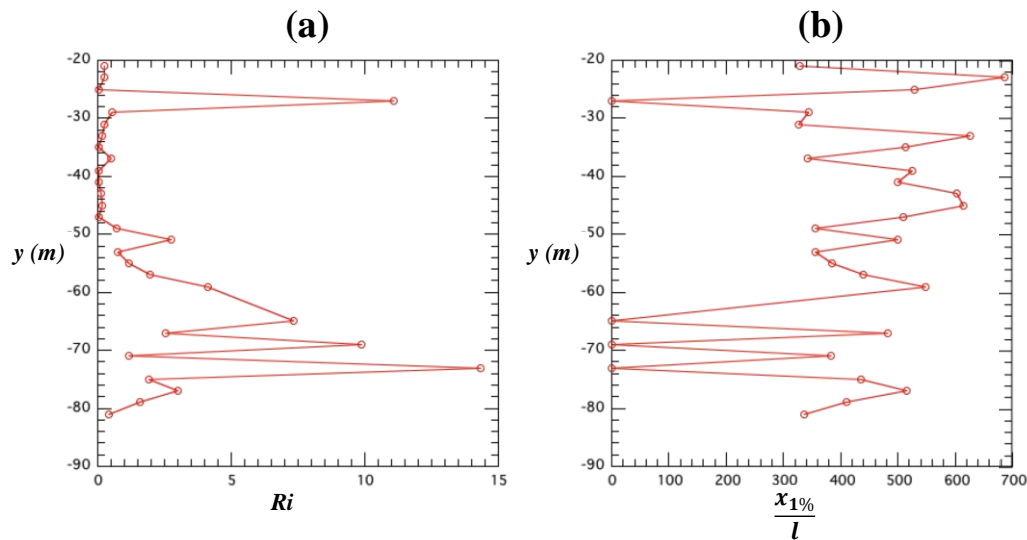


Figure 4.8: Estimation of turbulence decay length for measured GS data (station 53, 150 KHz) (Case 4).

**(a)** **(b)**
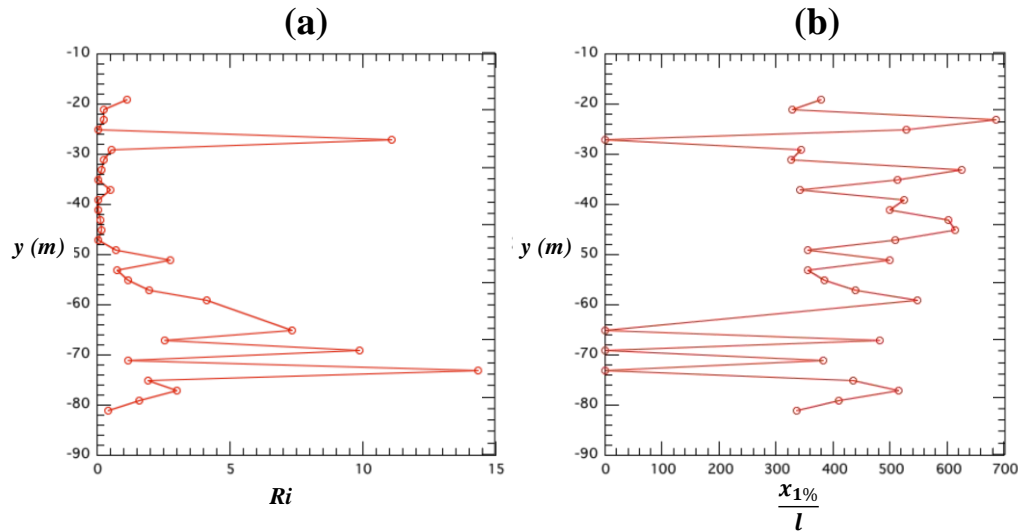


Figure 4.9: Estimation of turbulence decay length for measured GS data (station 53, 300 KHz) (Case 4).

## 4.5 Conclusion

In this chapter, we studied the interaction of OCT array wake turbulence with the background ocean stratification. A novel stratification profile is developed and employed in the LES simulations, to evaluate the effect of localized wake turbulence released into the flow. These simulations show the relationship between the threshold value of the background $Ri$ and the growth/decay rate of the turbulent kinetic energy. Based on findings from the simulations, we have developed a simple set of power law expressions that can be used to estimate the turbulent footprint of OCT arrays. For $Ri > 0.25$, the evolution of kinetic energy is given by a power-law Eq. (4.4.1), where the coefficients were obtained by fitting to simulation data, and as a function of $Ri$.

When $Ri < 0.25$, the evolution of kinetic energy is more complicated, and the total decay time comprises time spent in the initial growth phase and the asymptotic decay phase. The growth phase time is obtained that by tracking a fluid parcel as it travels from the centerline to the edge of the mixing layer. This is the time taken for the turbulence to mix and

homogenize the layer depth. However, this mixing results in the gradient Richardson number reaching a stable value at the end of the process. Thus, a second phase is observed during which the turbulence decays gradually under the effects of stable stratification. The power law expressions developed for the $Ri > 0.25$ was modified to account for this two-stage behavior. The three major findings of this study are summarized below:

1. A new unit problem for studying stability of stratified flows was developed. The problem formulation ensures the $Ri$ number is constant in the direction of gravity. Hence, the problem is free of additional length-scales that may arise from the variation in the $Ri$ number, and interact with the turbulent length-scales. In addition, the formulation ensures the bulk and gradient $Ri$ numbers are the same throughout.

2. Using LES simulations, the stability of the above stratification to turbulent perturbations was investigated. Simple power law expressions were developed to describe the evolution of the turbulent footprint from a localized source such as an OCT array at different $Ri$ numbers.

3. The models were applied to actual GS observational data to develop a practical estimate of the decay length of OCT array wakes.

## CHAPTER 5: INTERNAL WAVE GENERATION FROM OCEAN CURRENT TURBINE OPERATION CONCLUSIONS

The main goal of this chapter is to address the impact of internal waves generated by OCTs or an array of such devices on energy extraction, and on the background ocean mixing and transport processes. Using LES simulations, we have investigated for different values of the Richardson and Reynolds numbers, the dynamic processes involved in the formation of internal waves from submerged OCT systems such as tethered turbines, the properties of such waves, and their eventual fate. Our investigation also included the effects of the ambient turbulent intensity ($I_t$) [4] on internal waves from OCTs operating in a stratified environment. The results show that internal waves are formed when the turbulent wakes from submerged objects such as OCTs collapse under the stable density stratification. The resulting waves propagate in multiple directions, interacting nonlinearly with the background stratification and mean flow, thereby altering the transport of momentum and energy fluxes. The results are of significance, since such changes to the transport processes occurring in the ocean will affect mixing of nutrients, and sediment resuspension. In addition, OCT-generated internal waves will transport significant energy fluxes over large distances and produce substantial turbulent mixing when they break.

### 5.1 Background

Internal waves from submerged objects have been investigated in the context of naval submarine detection [31-33], wind farms [34, 35], atmospheric wakes of mountains [79] ('mountain waves'), and wastewater discharge in the ocean [80]. Much of the theoretical work was based on moving point source models developed by Miles [81] and Lighthill [82]

capable of predicting the phase line geometry of IGWs. Gilreath and Brandt [31] performed early experiments of a sphere towed in a water tank, which revealed the formation of deterministic (Lee), transient, and random (turbulence-generated) waves. Bonneton, Chomaz and Hopfinger [32] employed laser fluorescence diagnostic techniques to determine the transition between the deterministic Lee waves and the random turbulence-generated waves as occurring around $Fr = \frac{U}{NR_t} \sim 4$ , where $U$, $N$ and $R_t$ representing the mean flow velocity, buoyancy frequency and the radius of the turbine respectively. Abdilghanie and Diamessis [33] performed detailed numerical simulations of a towed sphere and found the properties of the wake-induced internal waves to depend on both the Reynolds number and the $Fr$.

Gravity waves from wind farm operation in the stable atmospheric stratification were investigated using numerical simulations by Allaerts and Meyers [33]. The authors of that study found the flow blockage presented by the wind farm to the upstream flow, resulted in an upward displacement of the atmospheric boundary layer and the excitation of gravity waves. The internal waves were then found to radiate upstream, where the associated pressure gradients decelerated the mean flow, adversely affecting the energy extraction and wind farm efficiency. Keeler et al. [80] used variations in sea surface brightness captured by satellite images to connect a sequence of observed internal wave phenomena to municipal wastewater discharged into the ocean several kilometers away. The impact of the dissipation and mixing due to the eventual wave breaking originating from a point source of turbulence was determined to be significant. Collectively, these earlier studies suggest the effect of internal wave generation, propagation, and saturation/breaking could

be significant, even in the instance when such waves were generated by highly localized sources.

The primary goal of this chapter is to develop a base of understanding of the effect of internal gravity waves emanating from OCT wakes on energy extraction and background ocean transport. This has been achieved through the following objectives: We use high-resolution LES numerical simulations to (i) characterize the properties of point source waves from OCTs, including their direction of propagation, and dominant frequency; and to (ii) understand the interaction of such point source waves with the background flow.

## 5.2 Characterization of OCT Internal Waves

Since the internal waves generated by OCTs originate from the collapse of the highly turbulent wakes in a stable stratification, they are expected to be random and hence cannot be described by simplified linear analysis. Thus, our strategy is to employ fully nonlinear, 3D numerical simulations to investigate the properties of the OCT-generated wavefield, and use insights from the simulations to identify dominant modes, which may guide mitigation strategies. The properties of point source waves from OCT operation were investigated using a series of baseline LES simulations.

Figure 5.1 shows the schematic of the formation of gravity waves as the turbulent wake behind OCTs collapses under the influence of background stable stratification. As upstream flow passes the turbine, a turbulent wake dominated by tip- and wake vortices is generated. In the absence of stratification, the wake turbulence will be dissipated over some length scale as shown in Chapter 2. However, when a stable stratification is present, a fluid packet displaced from its equilibrium position by a turbulent perturbation, will be returned to its original position leading to an oscillatory behavior. The oscillations of the fluid packet

will generate and propagate internal waves away from that point. A schematic of this process is shown in Figure 5.1.
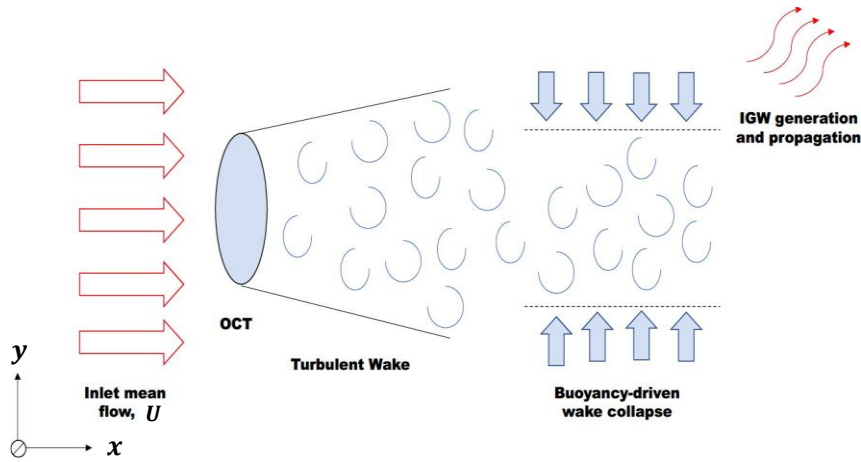


Figure 5.1: Schematic showing sequence of events leading to random IGW generation from OCTs in stable stratification.

## 5.3 Numerical Simulations

The simulations were performed using the STAR-CCM software, and using LES in a rectangular domain. A simulation domain size of $24D_t \times 24D_t \times 8D_t$ was used, with inlet (specified velocity) and outflow (zero gradient) boundary conditions specified along the streamwise direction. The top and bottom boundaries were treated as free-slip surfaces, while the spanwise boundaries were specified to be periodic. To prevent spurious reflections of the gravity waves from the boundaries of the computational domain, a viscous damping layer was used adjoining all outflow boundaries [83]. The damping layer was defined as a region of high viscosity to dissipate outgoing waves, with a thickness of $2D_t$. Within the damping layer, the viscous coefficient increases smoothly with distance [83, 84]. The turbine in our LES calculations was located at a distance of $8D_t$ from the top surface (as shown in Figure 5.2), to ensure gravity waves, including long-wavelength modes, evolve unimpeded by wall effects.

The LES simulations used a subgrid viscosity represented using a Smagorinsky [53] model, with standard values for the coefficients. The effect of the turbine rotor was captured using a BEM [39]. The variable density corresponding to a desired density stratification required for simulating internal wave fields was set up by defining two fluids with different densities, so that the field density at any point within the stratified layer can be obtained as a linear combination of the fluid mass fractions ($\rho(y) = \rho_H w_H + \rho_L w_L$, where H and L are the heavy and light fluids respectively, and $w_H = \frac{y - y_H}{y_L - y_H}$, and $w_L = 1 - w_H$) By adjusting the mass fraction of the fluids, the buoyancy frequency associated with the inlet profile may also be varied. Simulations with both tanh and piecewise linear profiles for the streamwise velocity were used, while the density profile was taken to be piecewise linear. The stratification associated with the density and velocity profiles were such that they were similar to the observed $Ri$ values [4] in the pycnocline region of the ocean. In Table 5.1, a summary of the LES simulations discussed in this chapter is given.
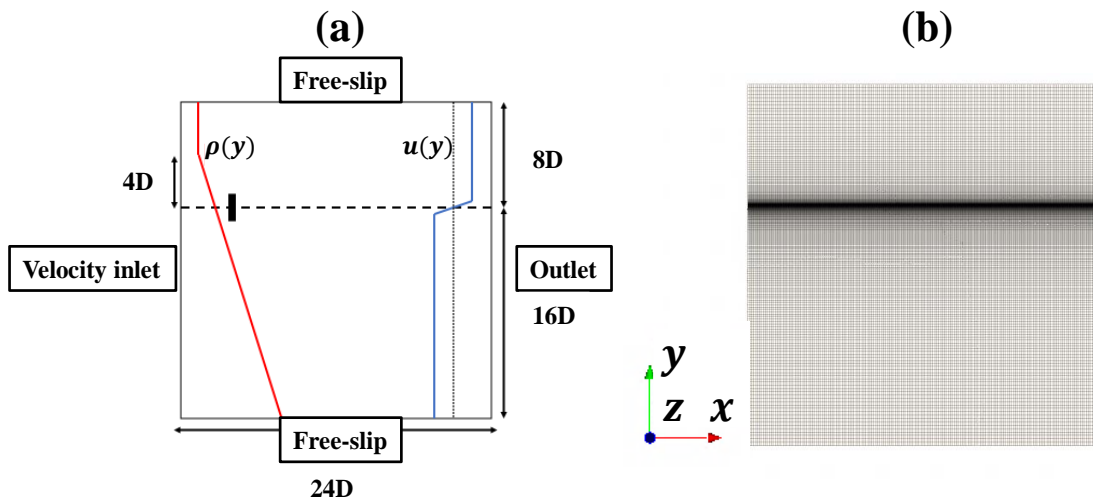


Figure 5.2: (a) Simulation domain showing boundary conditions, stratification profiles and turbine location and (b) adaptive mesh used for LES.

Table 5.1: Summary of LES simulations to investigate Internal Gravity Wave.

| Case number | $I_t$ | $Ri$ | $Re$ | Velocity profile |
|---|---|---|---|---|
| 1 | 0.1 | 1 | 100 | tanh |
| 2 | 0.02 | 1 | 100 | tanh |
| 3 | 0.1 | 1 | 10000 | Piecewise linear |
| 4 | 0.1 | 0.25 | 10000 | Piecewise linear |
| 5 | 0.1 | 0.05 | 10000 | Piecewise linear |

## 5.4. Simulation Results

### 5.4.1. Effect of Ambient Turbulence on the Formation of IGWs

The simulations were run for two different values of ambient turbulent intensities, and $Ri$ = 1 to capture the time-evolution of OCT-generated IGWs. Figure 5.3 shows contours of vertical velocity gradient $dv/dy$ for times 100, 200, and 300 seconds, and for $I_t$ = 10% (top row) and 2% (bottom row), respectively. From linear theory [85], the amplitude of the dominant mode associated with an IGW field can be written as

$$A_{\omega_{max}} \sim dv/dy \qquad (5.2.1)$$

where $A_{\omega_{max}}$ refers to the amplitude of the displaced isopycnal corresponding to the dominant mode $\omega_{max}$, and $dv/dy$ is gradient of vertical velocity. Invoking continuity for incompressible flows, we can further write $\frac{dv}{dy} = \nabla_H . V$, where $\nabla_H$ denotes the horizontal divergence and $V$ is the velocity vector. Thus, the stratified turbulent wake emanating from a single turbine (or some other perturbation source) can be analyzed for internal wave characteristics by plotting the $\frac{dv}{dy}$ field [29]. As seen in Figure 5.3, at the larger levels of

ambient turbulence intensity, IGW generation is enhanced, as seen by the more intense

levels of *dv/dy* and greater propagation distances. For instance, at $t = 100$ s, we see the

increased turbulence in the free-stream seeds the formation of stronger IGWs near the

turbine. These perturbations propagate away from the turbine source, at phase angles that

are dependent on the turbulence intensities, with slightly larger phase angles observed for

the more turbulent cases.

In Figure 5.4, we plot the evolution of the shear layer vorticity thickness $\delta w = 1/(d\mathrm{U}/d\mathrm{y})$

computed at the central vertical plane. The vorticity thickness is a standard measure

typically used to capture the thickness of a turbulent shear layer. The growth rates during

the initial stages appear independent of the turbulence intensity, a result that is expected

since the early time evolution is dominated by the linear Kelvin-Helmholtz instability.

Later, the growth of the shear layer as depicted by the vorticity thickness shows a strong

dependence on the turbulent perturbations to the flow. For larger turbulence intensities, the

IGWs are of stronger magnitude and hence transport more momentum, thereby increasing

the shear layer thickness.
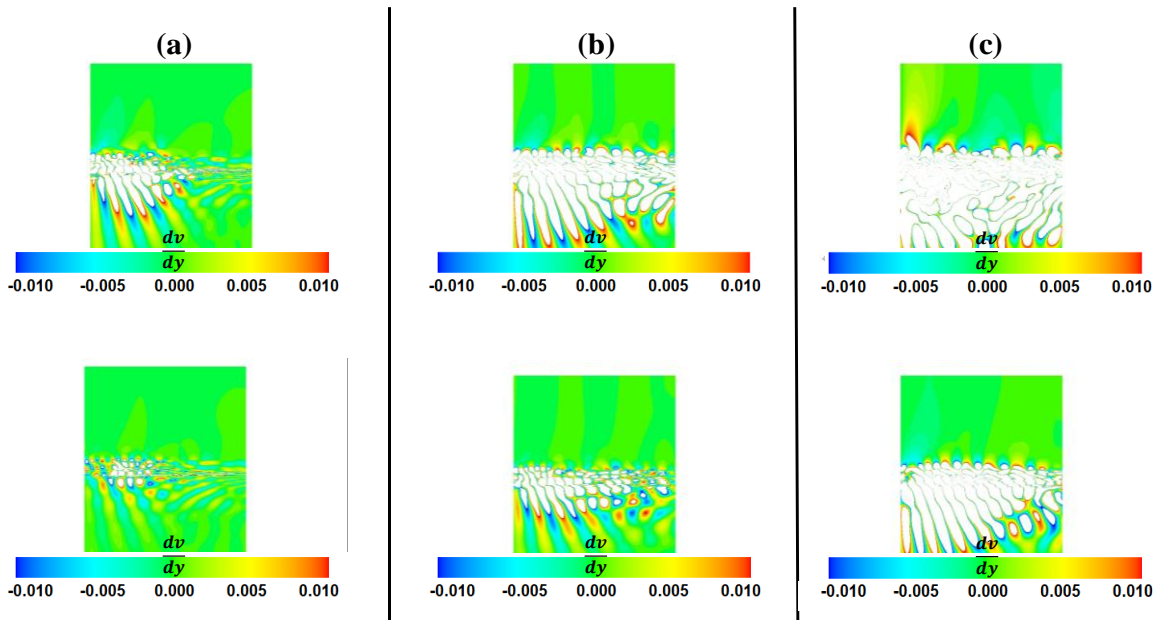
Figure 5.3: Contours of dv/dy in the x–y for different ambient turbulent intensities and at different times: (a) 100 s; (b) 200 s; and (c) 300 s for $I_t = 10\%$ (top row) and 2% (bottom row).
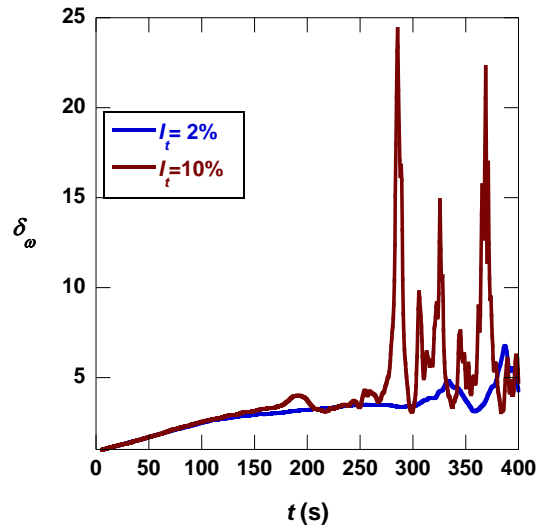


Figure 5.4: Vorticity thickness computed from simulations with turbulent intensities of 2% and 10%.

In our simulations, we also compute the principal direction of radiation of the IGWs using the phase angle $\theta = cos - 1(w/N)$ from the buoyancy frequency $N$ and the dominant frequency $w$. For the simulations shown in Figures 5.3 and 5.4, the phase angle $(\theta \sim 35)$

was found to be only weakly dependent of the turbulent intensity of 10% and 2%. Thus, increasing the turbulence intensity seeds the IGW generation with stronger (and more nonlinear) perturbations, but does not modify the dominant mode. Further investigation is required to similarly study the influence of the initial spectral content of the turbulent perturbations on the most dangerous mode of the IGW field.

In Figures 5.15(a) and (b), we show the time evolution of the average momentum fluxes at different vertical planes corresponding to $y = 0, -D_t, -3D_t$, and $-16D_t$ for Cases 1 and 2. In these plots, the transverse momentum flux $\overline{u'v'}$ represents transport of $u$-momentum by the vertical velocity $v$ which is associated with the IGW activity, and is scaled by $\frac{1}{2}U_0^2$, where $U_0$ is the inlet velocity the kinetic energy of the mean flow. The transport of momentum flux away from its source can significantly upset the momentum transport budget of the ocean. As observed in Figure 5.5, significant transport of the momentum flux away from the source occurs at the larger values of turbulence intensity through the internal wave propagation process. In addition, these figures show the attenuation of the momentum transport from the IGWs at greater distances from the wake source.
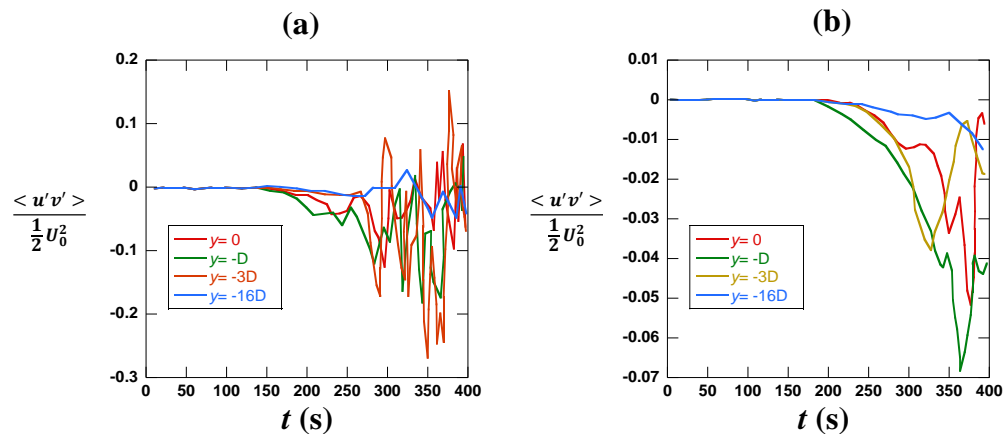


Figure 5.5: Momentum flux transported at different vertical planes for (a) $I_t = 10\%$, and (b) $I_t = 2\%$.

*5.4.2. Effect of the Richardson and Reynolds Numbers*

In this section, we consider the effect of the Reynolds ($Re = U_0 D_t / v$) and $Ri$ numbers, by varying the values of the viscosity and the buoyancy frequency. The Reynolds number in Case 3 was 100 times larger than that for Case 1. By increasing the $Re$, the IGW propagation continues over greater distances with lesser viscous dissipation as shown in Figure 5.6.

The simulations were also repeated for different values of the $Ri$ number, and the results are summarized in Figures 5.6 and 5.7. For $Ri = 0.25$, the IGW propagation is shown in Figure 5.7 and the dominant mode obtained from the phase angle satisfies corresponding linear theory [86]. The IGW formation and propagation are significantly suppressed for $Ri = 0.05$ due to the weaker stratification, as shown in Figure 5.8. At lower Richardson numbers below the critical value, shear dominates over buoyancy, so that local perturbations are amplified by the shear and do not propagate as waves.
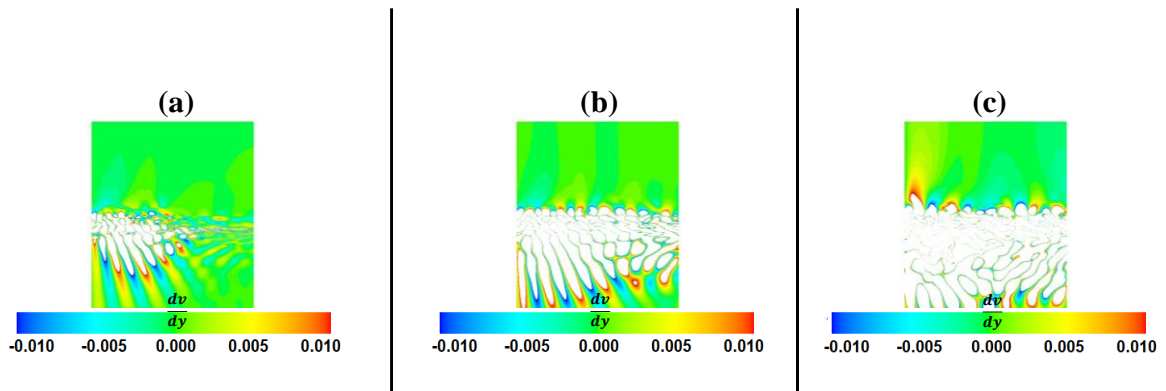


Figure 5.6: Contours of dv/dy from Case 3 at t = 100 (a), 200 (b) and 300 (c).
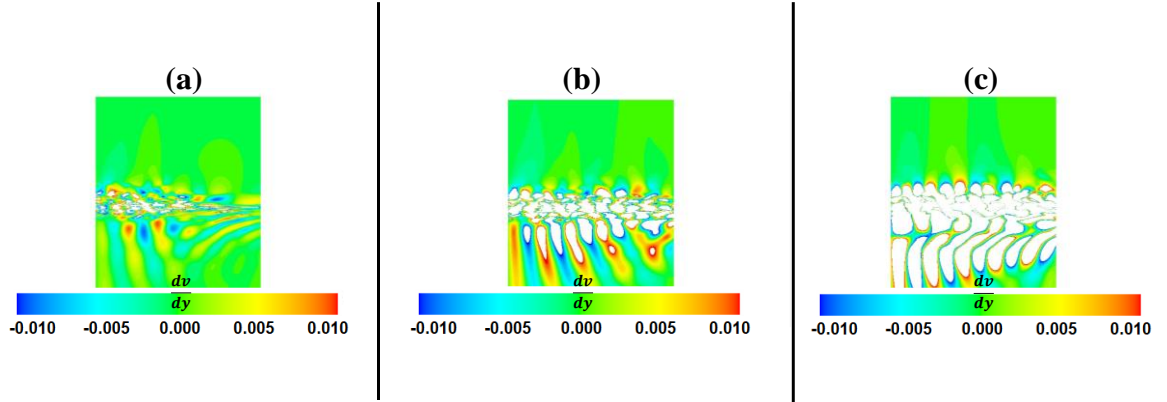
Figure 5.7: Contours of *dv/dy* in the *x–y* plane for Ri = 0.25 at t = 100 (a), 200 (b) and 300 (c).
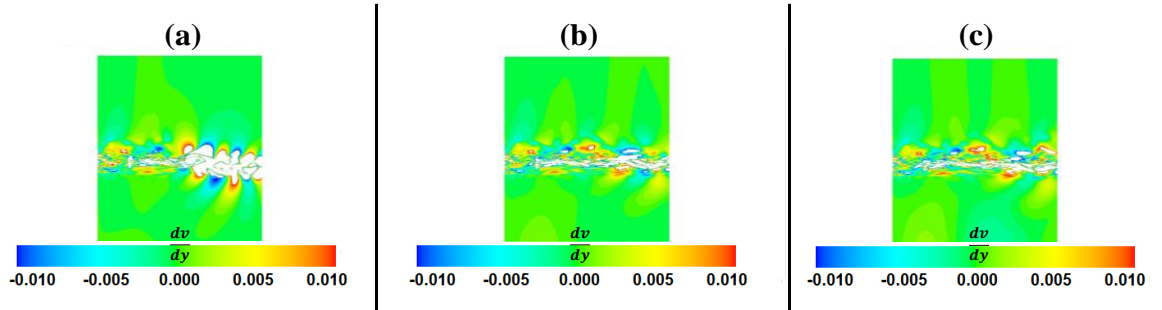


Figure 5.8: Contours of dv/dy in the x–y plane for Ri = 0.05 at t = 100 (a), 200 (b) and

300 (c).

In Figure 5.9(a), we plot contours of *dv/dy* from the LES simulations, and include the phase angle, which may be determined from $\theta = cos^{-1}\left(\frac{w}{N}\right)$: the dominant frequency $w$ was

obtained from analyzing the $\frac{dv}{dy}$ field. In Figure 5.9 (b), the phase angle is plotted at different

*Ri* numbers. At the lowest *Ri* (weak stable stratification), $\theta \sim \frac{\pi}{2}$, indicating very weak IGW

activity, so that the internal waves are stabilized quickly and predominantly propagate in

the streamwise direction. At stronger stratifications, the direction of propagation becomes

gradually vertical representing significant transport of fluxes away from the source, and

hence could affect other OCTs if operating in an array, or interfere the ocean transport and

mixing process. This is also captured in Figure 5.10, which shows the fluctuating transverse momentum flux $\langle u'v' \rangle$ at different $Ri$ numbers (stratifications), and scaled by the kinetic energy per unit mass of the mean flow. At low $Ri = 0.05$, the weak stratification implies the transverse momentum flux is insignificant, particularly at large transverse distances from the turbine. As the stratification is increased, the amplitude of oscillations of the momentum flux in the transverse direction is systematically increased, as seen in Figure 5.10. In addition, the oscillations are persistent at larger transverse distances away from the turbine, in the higher stratification simulations. The rms fluctuations of the scaled momentum fluxes are 0.00026, 0.00234 and 0.00617 for $Ri = 0.05$, 0.25 and 1 respectively. Finally, the imprint of the dominant mode is clearly seen in the oscillations of the transverse momentum flux in these figures.

**(a)**

**(b)**
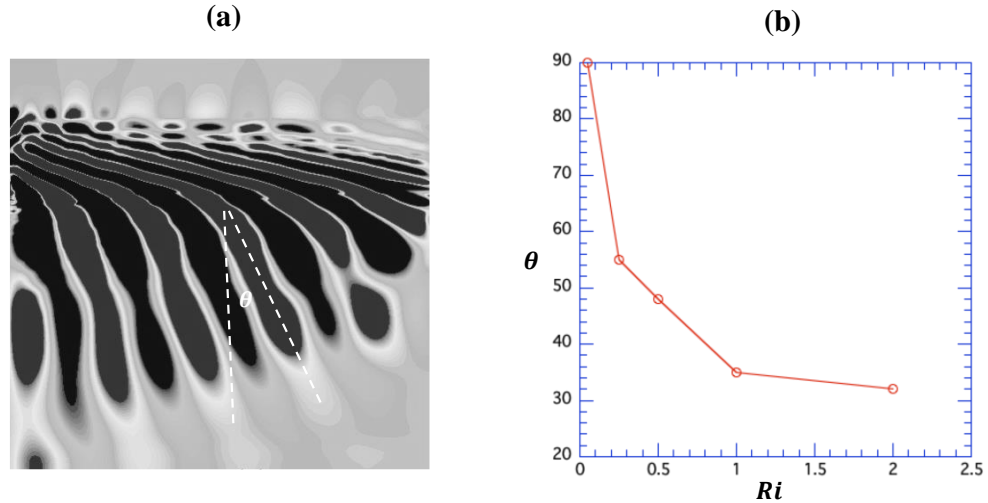


Figure 5.9: (a) Contours of dv/dy in the x–y plane used to compute direction of propagation of IGWs; and (b) the angle of propagation of IGWs as a function of Ri number.

**(a)**

**(b)**

**(c)**
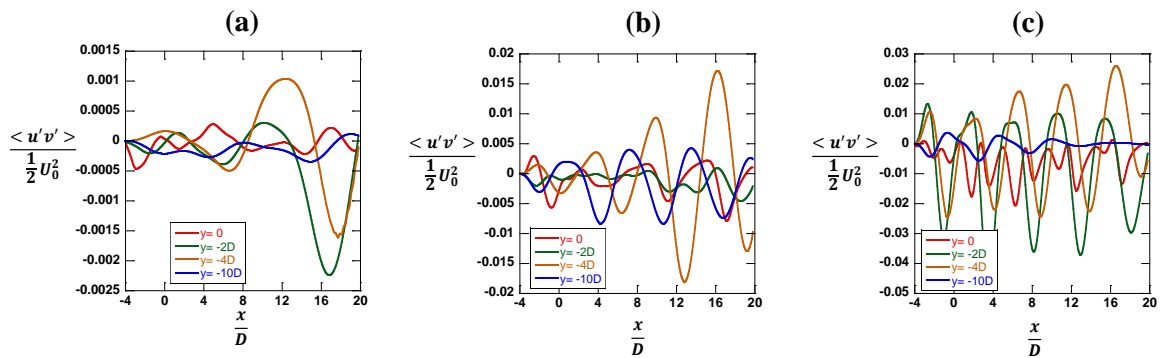


Figure 5.10: Scaled transverse momentum flux at different transverse distances from the turbine; (a) Ri = 0.05, (b) Ri = 0.25, and (c) Ri = 1.

Figure 5.11 shows the energy flux transported by the point source waves for different strengths of the background stratification, where $U_C$ is the time-averaged velocity at the centerline, at different vertical distances from the centerline. The energy fluxes are computed as the correlation of pressure and vertical velocity fluctuations and scaled by the centerline mean flow kinetic energy. We see that the scaled energy fluxes are increased by increasing the *Ri* number, as internal waves strengthen with stratification and transport

energy away from the source. The rms fluctuations of the scaled energy fluxes are 0.00142, 0.07932 and 0.61878 for Ri = 0.61878, 0.25 and 1 respectively.
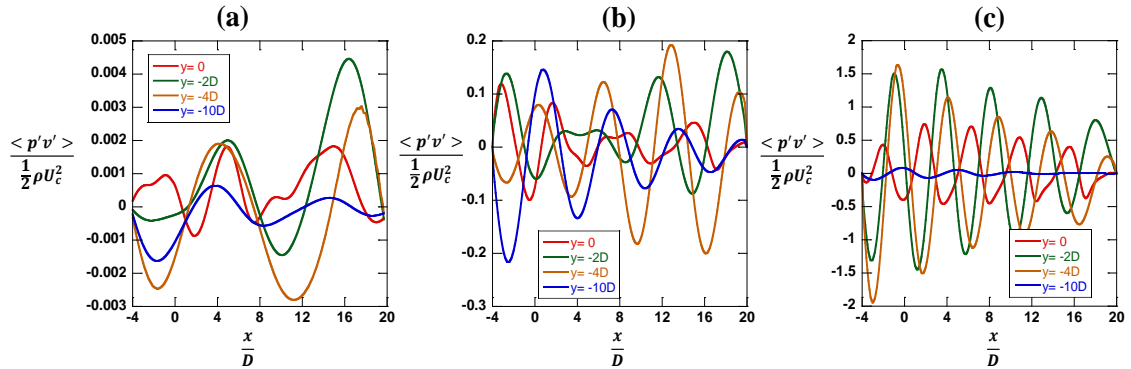


Figure 5.11: Scaled energy flux at different transverse distances from the turbine; (a) Ri = 0.05, (b) Ri = 0.25, and (c) Ri = 1.

A related quantity of interest is the effect of internal waves on turbulent kinetic energy. In Figure 5.12 the kinetic energy per unit mass $k$ associated with turbulent velocities is plotted, where $k = \frac{1}{2}(u'^2 + v'^2 + w'^2)$. We plot $(\frac{k}{0.5U_0^2})$ scaled by the mean kinetic energy that is available in the streamwise flow. For the case with no stratification (Figure 5.12(a)), only kinetic energy variations on the centerline are found, where the kinetic energy initially decreases until it reaches the turbine at $x/D = 0$. For $x/D > 0$, the turbine adds significant turbulent kinetic energy, which is then strengthened by the shear flow. Away from the centerline (Figure 5.12(a)), there is no turbulent kinetic energy due to the absence of internal waves.

Figure 5.12(b) shows the turbulent kinetic energy for a case with a density gradient corresponding to $Ri = 1$. Significant levels of turbulent kinetic energy are observed at the vertical locations away from the centerline, until it dissipates at $\frac{y}{D_t} \sim -16$. Once again, the turbulent kinetic energy is modulated by the dominant mode associated with the internal waves.
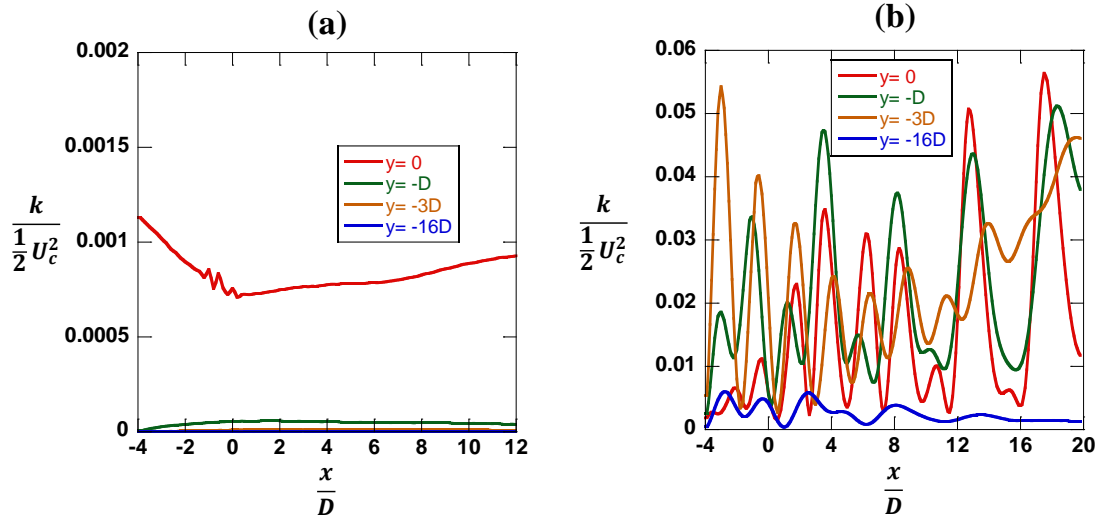
Figure 5.12: Scaled transverse turbulent energy flux at different transverse distances from the turbine; (a) no stratification, and (b) Ri = 1.

Internal waves affect the fluctuation velocity quantities related to turbulence, but they also affect the mean velocity field, which could have significant implications for power extraction of neighboring turbines. Figure 5.13 shows the mean streamwise velocity scaled by inlet velocity for three different stratifications. A momentum deficit downstream of the turbine is observed in the baseline case with no stratification, while increasing the Richardson number results in oscillatory behavior consistent with internal wave propagation. At the same time, the mean flow velocity at higher Richardson numbers is decreased relative to the inlet velocity since internal waves transport momentum away from the wake. Thus, downstream turbines will be operating in a lower velocity environment, and will have less power available to them.
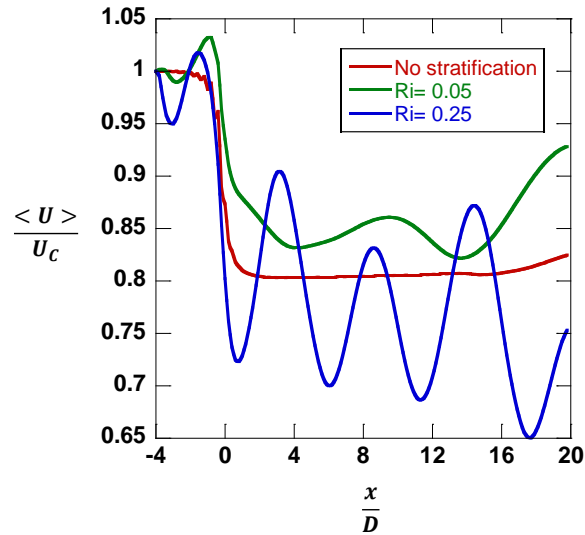
Figure 5.13: Average velocity along the streamwise coordinate for different Richardson numbers.

## 5.5 Summary

In this chapter, we have investigated the effect of free-stream turbulence on the generation of internal gravity waves from OCT operation. Our LES simulations reveal that greater levels of free-stream turbulence (and possibly wake turbulence) lead to stronger IGWs, by seeding the wake flow with larger-amplitude perturbations. The simulations were also used to investigate the effects of flow Reynolds numbers and the Richardson number. Different density profiles were investigated, while turbines in the LES simulations were modeled using BEM model. At larger Reynolds numbers, the IGWs propagated greater distances with lesser amplitude attenuation due to greater flow instability and lower levels of dissipation. The results showed the critical bulk $Ri$ threshold for the formation of the IGWs is 0.25. For $Ri < 0.25$, the IGW generation was largely suppressed, as expected. We find that as the Richardson number is increased, there is greater transport due to IGWs in the vertical direction, as seen in the decreasing phase angle, and increasing transverse momentum flux. A significant result is that internal waves affect both the turbulent and

mean flow quantities. Thus, in our simulations, the mean flow downstream of the turbine was decreased due to momentum removal by the internal waves, suggesting downstream turbines will have less power available to them if IGWs are present in the flow. These results will be useful in identifying zones of operation (based on modeled stratification), where IGW generation from OCTs may be suppressed.

## CHAPTER 6: CONCLUSIONS

Detailed numerical simulations and theoretical models have been developed to describe the two-way interactions between proposed ocean current turbine systems and the background oceanic flowfield. OCTs are capable of extracting energy from western boundary currents such as the Gulf Stream, which represent a perennial resource with stable current speeds in the range 1.5 – 3 m/s. However, for OCTs to be deployed at scale, uncertainties around the potential LCOE for typical operating conditions, and the environmental impact on the resource must be resolved. To address the former, the effect of spatio-temporal variations of the background flowfield on the performance of OCTs must be considered. In this work, we have addressed two specific aspects of this problem, namely the impact of upstream turbulence and spatial non-uniformities on the properties of the OCT wake. We have also investigated, using the above methodologies, the corresponding impact of OCT operation on the flowfield. The wake turbulence of an isolated OCT or an OCT farm can be dispersed and transported through the background stratification, and we have studied this problem using LES. Similarly, the turbulent wake can seed internal wave activity, which can significantly affect the ocean's momentum and energy transport budget, as IGWs radiate great distances from their point of origin.

Unlike wind turbines which typically operate in highly turbulent environments, OCTs will be exposed to a wide range of upstream turbulence intensities. The background ocean flow typically represents a low turbulence intensity flow, so that OCT wakes will recover slowly due to the diminished cross-wake entrainment. At the same time, turbines operating in the wakes of other devices will operate in a high-turbulence environment. Thus, low order models for use in LCOE calculations and in real-time optimization of individual device

locations within an OCT array, must be capable of accurately describing wake behavior and turbine performance over this wide range of turbulence intensities.

At low value of turbulence intensities, turbine wakes exhibit an extended near-wake region, and a gradual recovery to the recovery region. We proposed a simple, Jensen-type wake model that accounts for both the near- and far-wake regions, while the transition location and wake growth rate retain a dependence on the turbulence intensity. This simple model accurately describes wake behavior over a wide range of $I_t$, as demonstrated through comparison with our LES data. We then implement this wake model in a UWFLO framework, which describes the wake behavior of each turbine within an OCT farm, through the consistent accounting of momentum shadowing effects between upstream and downstream devices. The combined model was validated with LES simulations of multiple turbines at different configurations and upstream turbulence intensities and found to be in good agreement.

To address the issue of spatial non-uniformities in the upstream flow, in the form of shear associated with the mean streamwise velocity, the low-order shear model of [16] was extended here to multiple turbines through the UWFLO framework. The single turbine model was derived from rewriting the Bernoulli equation for flow with a mean velocity gradient [66], through the introduction of Coriolis and Boussinesq coefficients, which represent the momentum and energy fluxes for these conditions. Modified expressions for the wake velocity distribution and the turbine coefficient of power were derived in [66], and compared here with results from RANS simulations over a wide range of non-dimensional shear rates. The model for a single-turbine wake in shear flow, was implemented in the UWFLO [16] framework to capture corresponding wake interaction

effects. The resulting modeling framework for shear effects on multiple OCTs was validated with RANS data from simulations capturing different turbine configurations and non-dimensional shear rates.

In Chapter 4, we investigated the evolution of turbulence generated by a single turbine, or an OCT farm as it is transported through the background velocity and density stratification. Previous studies have indicated that linear perturbations to a stratified field are stable for $Ri > 0.25$ [85], while some ambiguity exists in the stability threshold for nonlinear and turbulent flow perturbations. To investigate this issue, we defined a new density/velocity profile that ensures a constant value of $Ri$ in the direction of gravity. This constitutes a new unit problem, and ensures the initial stratification profile does not itself introduce a lengthscale that might interact with the characteristic turbulent lengthscales. Furthermore, both the local gradient Richardson number and the global Richardson number are the same for the stratification profiles used in our study.

The evolution of turbulent perturbations was first studied in a baseline case, with no stratification to characterize the dissipation-driven decay of turbulent kinetic energy. A power law behavior was attributed to the turbulence decay, with the coefficients and exponents serving to characterize the extent of both physical and numerical dissipation in the LES simulations. The power law is instructive, since it can be used to estimate the time required for the TKE to dissipate to 1 % of its initial value, as a characteristic decay time. Using Taylor's hypothesis and the mean convective velocity, the time to decay can be converted to a corresponding lengthscale associated with the decay process, and referred as the spatial footprint of turbulence in our study.

This approach was then extended to the stratified case, where the Richardson number was systematically varied in our simulations. We found that for $Ri > 0.25$, perturbations were indeed stabilized and the spatial footprint of turbulence decay was estimated in terms of a characteristic lengthscale such as a turbine diameter or a lengthscale associated with an OCT farm. When $Ri < 0.25$, a more complex behavior was observed, and involved an initial shear-dominated unstable phase, followed by a stable phase. This is attributed to the mixing from turbulence growth, which served to re-homogenize the mixing layer and increasing the $Ri$ beyond the stability threshold. The power law described earlier was modified to incorporate this two-stage behavior for $Ri < 0.25$ conditions. Finally, to provide an estimate of the actual impact of OCT turbulence for realistic conditions, the power laws were applied to GS data from [4].

The turbulence from OCT wakes can also trigger the formation and propagation of internal gravity waves in a stratified layer satisfying $Ri < 0.25$. Such IGWs can propagate at a phase angle, resulting in transport of significant momentum and energy flux into the background flow. Typically, IGWs generated in the ocean stratified layers propagate over great distances (~km), and contribute significantly to the transport budget. When IGWs from a local source such as OCT operation interact with internal tides, nonlinear interactions can occur leading to wave-breaking and dissipation, thus upsetting the nutrient balance.

From our detailed LES simulations, we found that IGWs can indeed form from OCT operation, and radiate away from the source. The process is dependent on the background Richardson number, and observed to occur when $Ri > 0.25$, a condition that is satisfied through most of the ocean depth. We found IGW transport involves transfer of significant

amounts of momentum flux away from the point of generation. Furthermore, IGWs can also decrease the freestream mean velocities, thereby negatively impacting the performance of downstream devices (it is also possible that IGWs can radiate upstream, where they would affect the performance of upstream devices, although this effect was not observed in our simulations).

REFERENCES

[1]     J. A. Clarke, G. Connor, A. D. Grant, and C. M. Johnstone, "Design and testing of a contra-rotating tidal current turbine," *Proceedings of the Institution of Mechanical Engineers, Part A: Journal of Power and Energy,* vol. 221, no. 2, pp. 171−179, 2007.

[2]     J. M. Bane, R. He, M. Muglia, C. F. Lowcher, Y. Gong, and S. M. Haines, "Marine hydrokinetic energy from western boundary currents," *Annual Review of Marine Science,* vol. 9, no. 1, pp. 105−123, 2017.

[3]     X. Yang, K. A. Haas, and H. M. Fritz, "Theoretical assessment of ocean current energy potential for the Gulf Stream system," *Marine Technology Society Journal,* vol. 47, no. 4, pp. 101–112, 2013.

[4]     M. Muglia, H. Seim, and P. Taylor, "Gulf Stream marine hydrokinetic energy off Cape Hatteras, North Carolina," *Marine Technology Society Journal,* vol. 54, no. 6, pp. 24−36, 2020.

[5]     A. Baheri, P. Ramaprabhu, and C. Vermillion, "Iterative 3D layout optimization and parametric trade study for a reconfigurable ocean current turbine array using Bayesian Optimization," *Renewable Energy,* vol. 127, pp. 1052–1063, 2018.

[6]     J. Deese, P. Razi, M. Muglia, P. Ramaprabhu, and C. Vermillion, "Fused closed-loop flight dynamics and wake interaction modeling of tethered energy systems," in *ASME 2018 Dynamic Systems and Control Conference*, 2018, vol. 2.

[7]     L. P. Chamorro, D. R. Troolin, S.-J. Lee, R. E. A. Arndt, and F. Sotiropoulos, "Three-dimensional flow visualization in the wake of a miniature axial-flow

hydrokinetic turbine," *Experiments in Fluids,* journal article vol. 54, no. 2, pp. 1459, 2013.

[8]     P. Mycek, B. Gaurier, G. Germain, G. Pinon, and E. Rivoalen, "Experimental study of the turbulence intensity effects on marine current turbines behaviour. Part I: One single turbine," *Renewable Energy,* vol. 66, pp. 729−746, 2014.

[9]     T. Ishihara and Y. Fujino, "Development of a new wake model based on a wind tunnel experiment," *Global wind power,* 2004.

[10]    Y.-T. Wu and F. Porté-Agel, "Atmospheric turbulence rffects on eind-turbine eakes: an LES study," *Energies,* vol. 5, no. 12, pp. 5340−5362, 2012.

[11]    R. Metoyer, P. Chatterjee, K. Elfering, M. Bryant, K. Granlund, and A. Mazzoleni, "Modeling, simulation, and equilibrium analysis of tethered coaxial dual-rotor ocean current turbines," *Energy Conversion and Management,* vol. 243, pp. 113929, 2021.

[12]    R. Metoyer, P. Chatterjee, K. Elfering, M. Bryant, K. Granlund, and A. Mazzoleni, "Experimental analysis of dual coaxial turbines in skew," *Ocean Engineering,* vol. 215, pp. 107877, 2020.

[13]    A. Siddiqui, P. Ramaprabhu, J. Deese, and C. Vermillion, "Flight Dynamics and Control of a Farm of Tethered Energy Systems in a Turbulent Field," in *ASME 2019 Dynamic Systems and Control Conference*, 2019, vol. 2.

[14]    J. Reed, M. Cobb, J. Daniels, A. Siddiqui, M. Muglia, and C. Vermillion, "Hierarchical Control Design and Performance Assessment of an Ocean Kite in a Turbulent Flow Environment," *IFAC-PapersOnLine,* vol. 53, no. 2, pp. 12726-12732, 2020.

[15]    J. H. VanZwieten, P. Pyakurel, T. Ngo, C. Sultan, and N. I. J. I. j. o. m. e. Xiros, "An assessment of using variable blade pitch for moored ocean current turbine flight control," *International Journal of Marine Energy,* vol. 13, pp. 16–26, 2016.

[16]    S. Chowdhury, J. Zhang, A. Messac, and L. Castillo, "Unrestricted wind farm layout optimization (UWFLO): Investigating key factors influencing the maximum power generation," *Renewable Energy,* vol. 38, no. 1, pp. 16–30, 2012.

[17]    R. E. Todd, "High-frequency internal waves and thick bottom mixed layers observed by gliders in the Gulf Stream," *Geophysical Research Letters,* vol. 44, no. 12, pp. 6316−6325, 2017.

[18]    J. W. Miles, "On the stability of heterogeneous shear flows," *Journal of Fluid Mechanics,* vol. 10, no. 4, pp. 496–508, 1961.

[19]    S. A. Mack and H. C. Schoeberlein, "Richardson Number and Ocean Mixing: Towed Chain Observations," *Journal of Physical Oceanography,* vol. 34, no. 4, pp. 736–754, 2004.

[20]    H. D. I. Abarbanel, D. D. Holm, J. E. Marsden, and T. Ratiu, "Richardson number criterion for the nonlinear stability of three-dimensional stratified flow," *Physical Review Letters,* vol. 52, no. 26, pp. 2352−2355, 1984.

[21]    T. Nagai, A. Tandon, E. Kunze, and A. Mahadevan, "Spontaneous Generation of Near-Inertial Waves by the Kuroshio Front," *Journal of Physical Oceanography,* vol. 45, no. 9, pp. 2381−2406, 2015.

[22]    H. J. S. Fernando, "Turbulent mixing in stratified fluids," *Annual Review of Fluid Mechanics,* vol. 23, no. 1, pp. 455−493, 1991.

[23]     J. N. Moum, D. R. Caldwell, and C. A. Paulson, "Mixing in the equatorial surface layer and thermocline," *Journal of Geophysical Research: Oceans,* vol. 94, no. C2, pp. 2005–2022, 1989.

[24]     E. J. Strang and H. J. S. Fernando, "Entrainment and mixing in stratified shear flows," *Journal of Fluid Mechanics,* vol. 428, pp. 349−386, 2001.

[25]     H. T. Pham, S. Sarkar, and K. B. Winters, "Intermittent patches of turbulence in a stratified medium with stable shear," *Journal of Turbulence,* vol. 13, no. 2, pp. 1, 2012.

[26]     R. Bleck and D. B. Boudra, "Initial Testing of a Numerical Ocean Circulation Model Using a Hybrid (Quasi-Isopycnic) Vertical Coordinate," *Journal of Physical Oceanography,* vol. 11, no. 6, pp. 755–770, 1981.

[27]     E. D. Zaron and J. N. Moum, "A new look at Richardson number mixing schemes for equatorial ocean modeling," *Journal of Physical Oceanography,* vol. 39, no. 10, pp. 2652–2664, 2009.

[28]     B. D. Mater and S. K. Venayagamoorthy, "A unifying framework for parameterizing stably stratified shear-flow turbulence," *Physics of Fluids,* vol. 26, no. 3, pp. 036601, 2014.

[29]     C. Garrett and W. Munk, "Internal waves in the ocean," *Annual Review of Fluid Mechanics,* vol. 11, no. 1, pp. 339−369, 1979.

[30]     H. Van Haren and L. Gostiaux, "Energy release through internal wave breaking," *Oceanography,* vol. 25, no. 2, pp. 124−131, 2012.

[31]     H. Gilreath and A. Brandt, "Experiments on the generation of internal waves in a stratified fluid," *AIAA journal,* vol. 23, no. 5, pp. 693–700, 1985.

[32]    P. Bonneton, J. Chomaz, and E. Hopfinger, "Internal waves produced by the turbulent wake of a sphere moving horizontally in a stratified fluid," *Journal of Fluid Mechanics,* vol. 254, pp. 23–40, 1993.

[33]    A. M. Abdilghanie and P. J. Diamessis, "The internal gravity wave field emitted by a stably stratified turbulent wake," *Journal of Fluid Mechanics,* vol. 720, pp. 104−139, 2013.

[34]    D. Allaerts and J. Meyers, "Boundary-layer development and gravity waves in conventionally neutral wind farms," *Journal of Fluid Mechanics,* vol. 814, pp. 95−130, 2017.

[35]    D. Allaerts and J. Meyers, "Gravity waves and wind-farm efficiency in neutral and stable conditions," *Boundary-layer Meteorology,* vol. 166, no. 2, pp. 269−299, 2018.

[36]    P. Razi, P. Ramaprabhu, and C. Vermillion, "The performance of ocean current turbine arrays operating in a shear flow," presented at the Bulletin of the American Physical Society, 2018.

[37]    N. O. Jensen, "A note on wind generator interaction," Risø National Laboratory, Roskilde, Report 87-550-0971-9, 1983.

[38]    S. Frandsen *et al.*, "Analytical modelling of wind speed deficit in large offshore wind farms," *Wind Energy,* vol. 9, no. 1, pp. 39−53, 2006.

[39]    M. O. Hansen, *Aerodynamics of wind turbines*. Routledge, 2015.

[40]    R. J. Barthelmie and L. Jensen, "Evaluation of wind farm efficiency and wind turbine wakes at the Nysted offshore wind farm," *Wind Energy,* vol. 13, no. 6, pp. 573−586, 2010.

[41] R. J. Barthelmie, S. T. Frandsen, M. Nielsen, S. Pryor, P. E. Rethore, and H. E. Jørgensen, "Modelling and measurements of power losses and turbulence intensity in wind turbine wakes at Middelgrunden offshore wind farm," *Wind Energy,* vol. 10, no. 6, pp. 517−528, 2007.

[42] M. Bastankhah and F. Porté-Agel, "A new analytical model for wind-turbine wakes," *Renewable Energy,* vol. 70, pp. 116−123, 2014.

[43] A. Niayifar and F. J. E. Porté-Agel, "Analytical modeling of wind farms: A new approach for power prediction," *Energies,* vol. 9, no. 9, pp. 741, 2016.

[44] F. Carbajo Fuertes, C. D. Markfort, and F. Porté-Agel, "Wind turbine wake characterization with nacelle-mounted wind lidars for analytical wake model validation," *Remote Sensing,* vol. 10, no. 5, pp. 668, 2018.

[45] T. Ishihara and G.-W. Qian, "A new Gaussian-based analytical wake model for wind turbines considering ambient turbulence intensities and thrust coefficient effects," *Journal of Wind Engineering and Industrial Aerodynamics,* vol. 177, pp. 275−292, 2018.

[46] X. Gao, H. Yang, and L. Lu, "Optimization of wind turbine layout position in a wind farm using a newly-developed two-dimensional wake model," *Applied Energy,* vol. 174, pp. 192–200, 2016.

[47] I. Katic, J. Højstrup, and N. O. Jensen, "A Simple Model for Cluster Efficiency," presented at the European wind energy association conference and exhibition, 1986.

[48] A. Crespo, J. Hernández, and S. Frandsen, "Survey of modelling methods for wind turbine wakes and wind farms," *Wind Energy,* vol. 2, no. 1, pp. 1−24, 1999.

[49]    T. Blackmore, W. M. J. Batten, and A. S. Bahaj, "Influence of turbulence on the wake of a marine current turbine simulator," *Proceedings of the Royal Society A: Mathematical, Physical and Engineering Sciences,* vol. 470, no. 2170, pp. 20140331, 2014.

[50]    L. Tian, W. Zhu, W. Shen, N. Zhao, and Z. Shen, "Development and validation of a new two-dimensional wake model for wind turbine wakes," *Journal of Wind Engineering and Industrial Aerodynamics,* vol. 137, pp. 90–99, 2015.

[51]    L. P. Chamorro and F. Porté-Agel, "A wind tunnel investigation of wind turbine wakes: Boundary-layer turbulence effects," *Boundary-Layer Meteorology,* journal article vol. 132, no. 1, pp. 129–149, 2009.

[52]    U. Hassan, "A wind tunnel investigation of the wake structure within small wind turbine farms," Harwell Laboratory, Energy Technology Support Unit, 1993.

[53]    J. Smagorinsky, "General circulation experiments with the primitive equations: I. The basic experiment," *Monthly weather review,* vol. 91, no. 3, pp. 99−164, 1963.

[54]    T. Stallard, T. Feng, and P. K. Stansby, "Experimental study of the mean wake of a tidal stream rotor in a shallow turbulent flow," *Journal of Fluids and Structures,* vol. 54, pp. 235−246, 2015.

[55]    P. S. Veers, "Three-dimensional wind simulation," Sandia National Labs, 1988.

[56]    P. Pyakurel, J. H. VanZwieten, M. Dhanak, and N. I. Xiros, "Numerical modeling of turbulence and its effect on ocean current turbines," *International Journal of Marine Energy,* vol. 17, pp. 84–97, 2017.

[57]    J. F. Ainslie, "Calculating the flowfield in the wake of wind turbines," *Journal of Wind Engineering and Industrial Aerodynamics,* vol. 27, no. 1, pp. 213–224, 1988.

[58]    J. Jeong and F. Hussain, "On the identification of a vortex," *Journal of Fluid Mechanics,* vol. 285, pp. 69–94, 1995.

[59]    L. E. Myers and A. S. Bahaj, "An experimental investigation simulating flow effects in first generation marine current energy converter arrays," *Renewable Energy,* vol. 37, no. 1, pp. 28–36, 2012.

[60]    P. E. J. Vermeulen, "An experimental analysis of wind turbine wakes," in *3rd International Symposium on Wind Energy Systems*, 1980, pp. 431–450.

[61]    E. Machefaux *et al.*, "An experimental and numerical study of the atmospheric stability impact on wind turbine wakes," *Wind energy,* vol. 19, no. 10, pp. 1785−1805, 2016.

[62]    F. Porté-Agel, M. Bastankhah, and S. Shamsoddin, "Wind-Turbine and Wind-Farm Flows: A Review," *Boundary-Layer Meteorology,* no. 174, pp. 1–59, 2019.

[63]    T. Stallard, R. Collings, T. Feng, and J. Whelan, "Interactions between tidal turbine wakes: experimental study of a group of three-bladed rotors," *Philosophical Transactions of the Royal Society A: Mathematical, Physical and Engineering Sciences,* vol. 371, no. 1985, pp. 20120159, 2013.

[64]    V. S. Neary, B. Gunawan, C. Hill, and L. P. Chamorro, "Near and far field flow disturbances induced by model hydrokinetic turbine: ADV and ADP comparison," *Renewable Energy,* vol. 60, pp. 1–6, 2013.

[65]    S. J. Andersen, J. N. Sørensen, S. Ivanell, and R. F. Mikkelsen, "Comparison of Engineering Wake Models with CFD Simulations," *Journal of Physics: Conference Series,* vol. 524, pp. 012161, 2014.

[66]   L. P. Chamorro and R. A Arndt, "Non-uniform velocity distribution effect on the Betz–Joukowsky limit," *Wind Energy,* vol. 16, no. 2, pp. 279–282, 2013.

[67]   D. C. Wilcox, "Reassessment of the scale-determining equation for advanced turbulence models," *AIAA,* vol. 26, no. 11, pp. 1299–1310, 1988.

[68]   S. Draper, T. Nishino, T. A. A. Adcock, and P. H. Taylor, "Performance of an ideal turbine in an inviscid shear flow," *Journal of Fluid Mechanics,* vol. 796, pp. 86–112, 2016.

[69]   J. R. West and S. K. Lele, "Wind turbine performance in very large wind farms: Betz analysis revisited," *Energies,* vol. 13, no. 5, pp. 1078, 2020.

[70]   G. Kavari, M. Tahani, and M. Mirhosseini, "Wind shear effect on aerodynamic performance and energy production of horizontal axis wind turbines with developing blade element momentum theory," *Journal of Cleaner Production,* vol. 219, pp. 368–376, 2019.

[71]   M.-S. Jeong, S.-W. Kim, I. Lee, and S.-J. Yoo, "Wake impacts on aerodynamic and aeroelastic behaviors of a horizontal axis wind turbine blade for sheared and turbulent flow conditions," *Journal of Fluids and Structures,* vol. 50, pp. 66–78, 2014.

[72]   J. C. Smith, R. Carriveau, and D. S.-K. Ting, "Turbine power production sensitivity to coastal sheared and turbulent inflows," *Wind Engineering,* vol. 39, no. 2, pp. 183–191, 2015.

[73]   A. Vinod, C. Han, and A. Banerjee, "Tidal turbine performance and near-wake characteristics in a sheared turbulent inflow," *Renewable Energy,* vol. 175, pp. 840–852, 2021.

[74] U. Ahmed, D. D. Apsley, I. Afgan, T. Stallard, and P. K. Stansby, "Fluctuating loads on a tidal turbine due to velocity shear and turbulence: Comparison of CFD with field data," *Renewable Energy,* vol. 112, pp. 235–246, 2017.

[75] A. Betz, "Das maximum der theoretisch möglichen ausnutzung des windes durch windmotoren," *Zeitschrift fur das Gesamte Turbinenwesten,* vol. 20, 1920.

[76] L. Dubbs, A. G. Keeler, and T. J. T. E. J. O'Meara, "Permitting, risk and marine hydrokinetic energy development," *The Electricity Journal,* vol. 26, no. 10, pp. 64-74, 2013.

[77] Y. Song and D. Haidvogel, "A semi-implicit ocean circulation model using a generalized topography-following coordinate system," *Journal of Computational Physics,* vol. 115, no. 1, pp. 228–244, 1994.

[78] W. K. George, "The decay of homogeneous isotropic turbulence," *Physics of Fluids A: Fluid Dynamics,* vol. 4, no. 7, pp. 1492–1509, 1992.

[79] R. Rotunno, V. Grubišić, and P. Smolarkiewicz, "Vorticity and potential vorticity in mountain wakes," *Journal of the Atmospheric Sciences,* vol. 56, no. 16, pp. 2796–2810, 1999.

[80] R. N. Keeler, V. G. Bondur, and C. H. Gibson, "Optical satellite imagery detection of internal wave effects from a submerged turbulent outfall in the stratified ocean," *Geophysical Research Letters,* vol. 32, no. 12, 2005.

[81] J. W. Miles, "Internal waves generated by a horizontally moving source," *Geophysical Fluid Dynamics,* vol. 2, no. 1, pp. 63–87, 1971.

[82] M. J. Lighthill and J. Lighthill, *Waves in fluids*. Cambridge University Press, 2001.

[83]    D. R. Durran, *Numerical Methods for Wave Equations in Geophysical Fluid Dynamics*. Springer Science & Business Media, 2013.

[84]    A. Abdilghanie, "A Numerical Investigation Of Turbulence-Driven And Forced Generation Of Internal Gravitywaves In Stratified Mid-Water," 2011.

[85]    P. Hazel, "Numerical studies of the stability of inviscid stratified shear flows," *Journal of Fluid Mechanics,* vol. 51, no. 1, pp. 39–61, 1972.

[86]    H. T. Pham, S. Sarkar, and K. A. Brucker, "Dynamics of a stratified shear layer above a region of uniform stratification," *Journal of fluid mechanics,* vol. 630, pp. 191–223, 2009.

[87]    B. R. Sutherland, "Dynamic excitation of internal gravity waves in the equatorial oceans," *Journal of Physical Oceanography,* vol. 26, no. 11, pp. 2398–2419, 1996.

## APPENDIX A.1: NON-UNIFORM INLET VELOCITY MODEL

A detailed presentation of the shear model of [66] is presented here. The Bernoulli equation is applied first between sections $(0)$ and $(t^-)$, and then between $(t^+)$ and $(x)$ (Fig. 3.1) to give

$$\frac{\bar{p}_0}{\rho} + \Xi_0 \frac{\bar{U}_0^2}{2} = \frac{\bar{p}_{t^-}}{\rho} + \Xi_{t^-} \frac{\bar{U}_{t^-}^2}{2}, \tag{A.1.1}$$

$$\frac{\bar{p}_{t^+}}{\rho} + \Xi_{t^+} \frac{\bar{U}_{t^+}^2}{2} = \frac{\bar{p}_x}{\rho} + \Xi_x \frac{\bar{U}_x^2}{2}. \tag{A.1.2}$$

The thrust $T$ produced by the turbine is given by

$$T = \dot{m}(\Psi_0 \bar{U}_0 - \Psi_x \bar{U}_x), \tag{A.1.3}$$

where $\dot{m}$ is the mass flux, and the pressure difference between $(0)$ and $(x)$ is neglected. The thrust is also independently obtained from

$$T = A_{t^-}(p_{t^-} - p_{t^+}). \tag{A.1.4}$$

For this simple case, we can assume $\bar{U}_{t^-} \sim \bar{U}_{t^+}$, $p_0 \sim p_{t^+} \sim p_\infty$ and $\Xi_{t^-} \sim \Xi_{t^+}$ [66]. Using these assumptions, and combining Eqs. (A.1.1) and (A.1.2), we can write

$$p_{t^-} - p_{t^+} = \frac{1}{2}\rho(\Xi_0 \bar{U}_0^2 - \Xi_x \bar{U}_x^2), \tag{A.1.5}$$

which, when substituted into Eq. (A.1.4) gives for the turbine thrust,

$$T = \frac{1}{2}\rho A_{t^-}(\Xi_0 \bar{U}_0^2 - \Xi_x \bar{U}_x^2). \tag{A.1.6}$$

From combining Eqs. (A.1.3) and (A.1.6) with the definition for $\dot{m}$, an expression for $\bar{U}_{t^-}$ is obtained:

$$\bar{U}_{t^-} = \frac{1}{2}\frac{\Xi_0 \bar{U}_0^2 - \Xi_x \bar{U}_x^2}{(\Psi \bar{U}_0 - \Psi \bar{U}_x)} \tag{A.1.7}$$

For *weak shear*, the additional assumption $\Xi_0 \sim \Xi_x \sim \Xi$, and $\Psi_0 \sim \Psi_x \sim \Psi$ is then made (in the current study, we have also used data from strong shear conditions to verify the validity of the above assumption). Then, Eq. (A.1.7) simplifies to

$$\bar{U}_{t^-} = \frac{\Xi}{\Psi} \frac{\bar{U}_0 + \bar{U}_x}{2}. \tag{A.1.8}$$

Defining the induction factor $a = 1 - \frac{\bar{U}_{t^-}}{\bar{U}_0}$, results in

$$\bar{U}_{t^-} = \bar{U}_0(1 - a), \tag{A.1.9}$$

while combining eqs. (A.1.8) and (A.1.9) gives for the downstream velocity $\bar{U}_x$,

$$\bar{U}_x = \bar{U}_0 \left( \frac{2\Psi}{\Xi} (1 - a) - 1 \right). \tag{A.1.10}$$

Finally, the turbine power is calculated as $P = T\bar{U}_{t^-}$, where $T$ is taken from Eq. (A.1.6), and $\bar{U}_x$ is obtained from Eq. (A.1.10). Making these substitutions gives the following expression for the power of a single turbine embedded in a shear velocity profile:

$$P = \frac{1}{2} \rho A_{t^-} \bar{U}_0^3 4\Psi(1 - a)^2 \left( 1 + \frac{\Psi}{\Xi}(a - 1) \right), \tag{A.1.11}$$

while the corresponding power coefficient is given by

$$C_P = 4\Psi(1 - a)^2 \left( 1 + \frac{\Psi}{\Xi}(a - 1) \right). \tag{A.1.12}$$

APPENDIX A.2: NUMERICAL MODELING OF TURBULENT FLOWFIELD

The methodology described here to generate a coherent turbulent flow field follows [56] and [55]. A power spectral density (PSD) consistent with Kolmogorov's –5/3rd scaling was assumed for the inertial scales, and taken as a starting point for all three velocity fluctuations. Thus, for the $m^{th}$ direction, a spectral amplitude of $A_m$ was taken (and related to the turbulent intensity), and the PSD is written as

$$G^m(f) = A_m f^{-\frac{5}{3}} \qquad (A.2.1)$$

The amplitude $A_m$ is determined by assuming values of standard deviation in each of the directions based on a given turbulence intensity, and requiring

$$\sigma_m^2 = \int_{f_{min}}^{f_{max}} G^m df \qquad (A.2.2)$$

For the model, we take the standard deviations in each direction as

$$\sigma_v = P\sigma_u \qquad (A.2.3)$$

$$\sigma_w = Q\sigma_u \qquad (A.2.4)$$

$$\sigma_u = \frac{I_t \overline{U}}{\sqrt{1 + P^2 + Q^2}} \qquad (A.2.5)$$

with $I_t$, $\overline{U}$ taken as mentioned earlier, and $P = Q = 1$. Turbulent intensity in each direction is given by

$$I_{t_m} = \frac{\sigma_m}{|\overline{\overline{U}}|}. \qquad (A.2.6)$$

Combining Eqs. (A.2.1)–(A.2.6), the following expressions for the PSD function and its amplitude can be obtained

$$G^m = \frac{2\bar{U}^2 I_{t_m}^2}{3\left[\frac{1}{f_{min}^{2/3}} - \frac{1}{f_{max}^{2/3}}\right]} f^{-5/3} \qquad (A.2.7)$$

$$A_m = \frac{2\bar{U}^2 I_{t_m}^2}{3\left[\frac{1}{f_{min}^{2/3}} - \frac{1}{f_{max}^{2/3}}\right]} \qquad (A.2.8)$$

A spatial correlation on the inlet plane for each velocity component is introduced in the form of a coherence function, which is defined as

$$coh_{ij}(f) = \exp\left(-\frac{\xi \Delta r_{ij} f}{\bar{U}}\right) \qquad (A.2.9)$$

where $\Delta r_{ij}$ is the distance between any two mesh points '$i$' and '$j$' on the inlet plane, and $\xi$ is a constant that determines the coherence length scale. The cross-spectral density between nodes '$i$' and '$j$' is then written as:

$$S_{ij}^m(f) = 2coh_{ij}(f)A_m f^{-5/3} df \qquad (A.2.10)$$

where we assume a frequency increment $df = f_{min}/10$. The velocity component in the $m$-direction is given at a point '$j$' and as a function of time, in terms of the equation,

$$m_j(t) = \sum_{k=1}^{N} |m_{kj}^*| \sin(2\pi f_k^* t + \theta_{kj}^R) \qquad (A.2.11)$$

where $\theta_{kj}^R$ is a randomized phase angle, and $N$ represents the number of steps in the discrete frequency space.

APPENDIX A.3: VALIDATION OF LES SIMULATIONS

In this Appendix, we describe our validation of LES simulations of IGW generation using STAR-CCM, by comparing with results from the DNS simulations of [86], for the specific case of a stratified shear layer above a region of uniform stratification. LES were performed to investigate the behavior of IGWs in a background density and velocity (shear) stratification as defined in [86]. We have also explored the effect of different values of the Richardson number $Ri$ on the generation of the IGWs. Internal gravity waves were found to radiate downward from the center of the shear layer, and propagate within the stratification layer. The results show that the angle between the phase lines and the vertical increased with $Ri$, in agreement with linear theory.

*A.3.1. Numerical Simulation Details*

The problem definition closely follows the details provided in [86], and briefly reviewed here. The simulation domain had dimensions of $51.6 \times 17.2 \times 96.5$ (m), with a uniform mesh density in horizontal directions. In the vertical direction ($y$–), a higher mesh density was used within the region containing the shear layer (Figure A.1), while gradually decreasing away from this region. Periodic boundary conditions were used in the streamwise and spanwise directions, while the vertical boundaries were treated as symmetry planes.
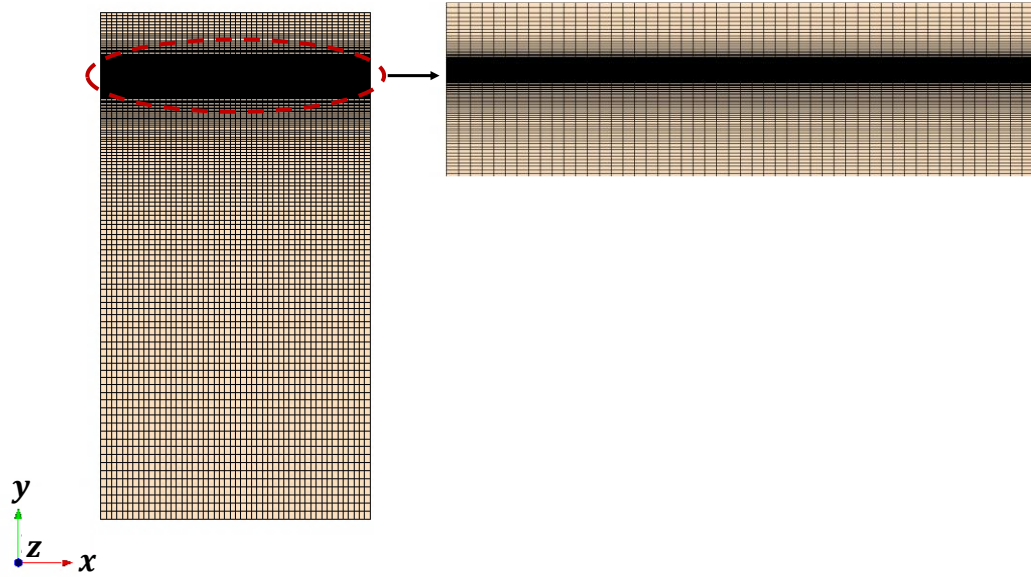
Figure A.3.1: Schematic of the simulation domain and mesh used in the validation case study.

The streamwise velocity was defined as a hyperbolic tangent profile function of the vertical direction ($y$), and expressed as $U_0 = \left(-\frac{\Delta U}{2}\right) \tanh(2y/\delta)$, where $\delta$ is the vorticity thickness and $\Delta U$ is the shear velocity scale. The density profiles were defined as distinct piecewise-linear functions above and below the shear layer: Thus, we take $\rho(y) = \rho_a + Ri_a \frac{\rho}{g} \left(\frac{du}{dy}\right)^2$ for $y > -2.5\delta$, and $\rho(y) = \rho_b + Ri_b \frac{\rho}{g} \left(\frac{du}{dy}\right)^2$ for $y < -2.5\delta$, where $\rho_a$ and $\rho_b$ are the densities at $y = 12.5$ m, and $y = -2.5\delta$ respectively, corresponding to the definition used in [86], and similar to the pycnocline region of the ocean. In Figure A.2, the density and velocity profiles corresponding to a moderate stratification $Ri = 0.05$ above the shear layer ($y < -2.5\delta$), and $Ri = 0.25$ below the shear layer are shown.
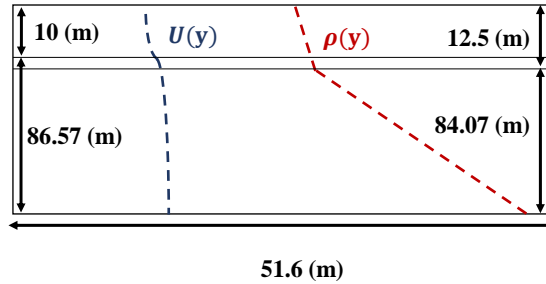
Figure A.3.2: Density profiles corresponding to a Ri number of 0.25.

*A.3.2. Simulation Results*

The simulations were performed for different values of the *Ri* number (0.1, 0.25, 1), and the results are presented in this section along with a comparison with the DNS of [86]. Based on linear theory [85, 87], internal gravity waves will propagate if the magnitude of the buoyancy frequency is greater than the dominant frequency ($w < N$). The direction of dominant waves is then given by the phase angle, which is obtained from $\theta = cos^{-1}(\frac{w}{N})$ using linear theory [85, 87]. To visualize the IGW field, we plot contours of $\partial v/\partial y$ in the *x–y* plane in Figure A.3 at a time of 80 s, and corresponding to *Ri* values of 0.1, 0.25, and 1. For $Ri = 0.1$, the IGW field is suppressed (Figure A.3 (a)) by the presence of the weak density stratification. As *Ri* is increased beyond the critical value for stability (0.25), the phase angle of the dominant wave increases (Figures A.3 (b) – (c)). Note that the phase angle is defined from the vertical, and was observed in our simulations to be $\theta \sim 35$ and 59 degrees corresponding to $Ri = 0.25$ and 1 respectively. These results are in good agreement with the DNS simulations of [86] for the same conditions, which reported phase angles of $\theta = 31$ and $\theta = 65$ for $Ri = 0.25$ and 1 respectively. The phase angle can also be estimated from linear theory, which gives $\theta = 31$ and $\theta = 65$ corresponding to $Ri = 0.25$ and 1 respectively.
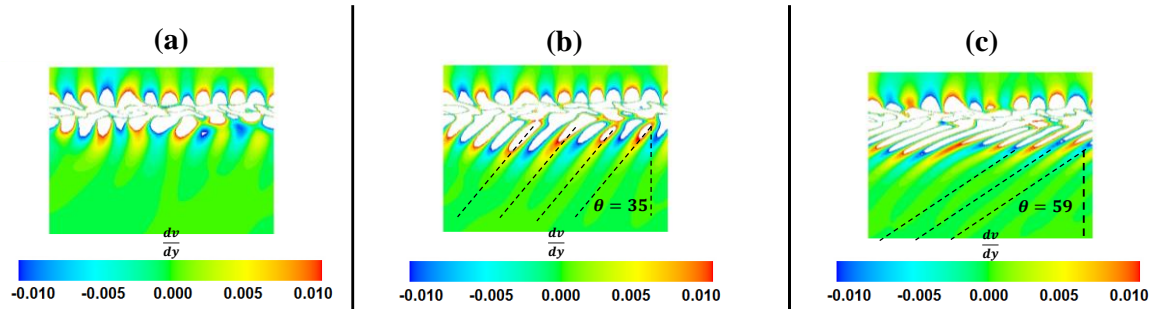
Figure A.3.3: Contours of $\partial v/\partial y$ in the x–y plane at a time 80 s for Ri = 0.1 (a), 0.25 (b) and 1 (c).

The wavelength of the most unstable mode in the IGW wave packet can be obtained in our simulations as the peak of the power spectra of the vertical velocity. In Figure A.4(a), the spanwise-averaged vertical velocity at the center plane of the shear layer is plotted as a function of the streamwise coordinate at a time of 50 s. The corresponding power spectra was computed and plotted in Figure A.4 (b), and shows a dominant peak at a wavelength of $\lambda_{max} = \frac{2\pi}{k} \sim 7.4m$ in agreement with [86]. The DNS simulations of [86] shows the dominant peak at wavelength of $\lambda_{max} = 7.4 \pm 0.5$ m. The presence of the dominant wavelength is also verified visually through contours of the spanwise vorticity at t = 50 s. As plotted in Figure A.5, the spanwise vorticity field shows a clear signature of a dominant mode corresponding to $\lambda_{max}$.

**(a)**

**(b)**
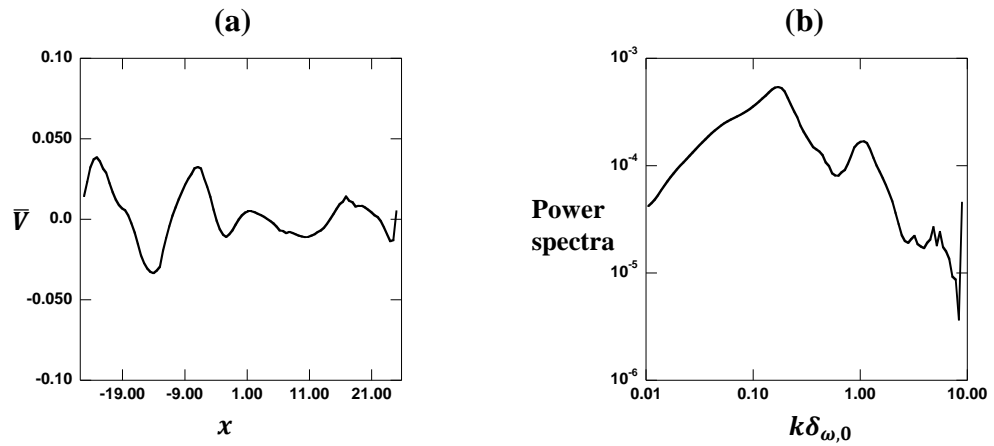


Figure A.3.4: (a) x-profiles of vertical velocity and (b) power spectra of vertical velocity computed at t = 50 s, and from simulation with Ri = 0.25.

**51.6 (m)**

**7.4 (m)**
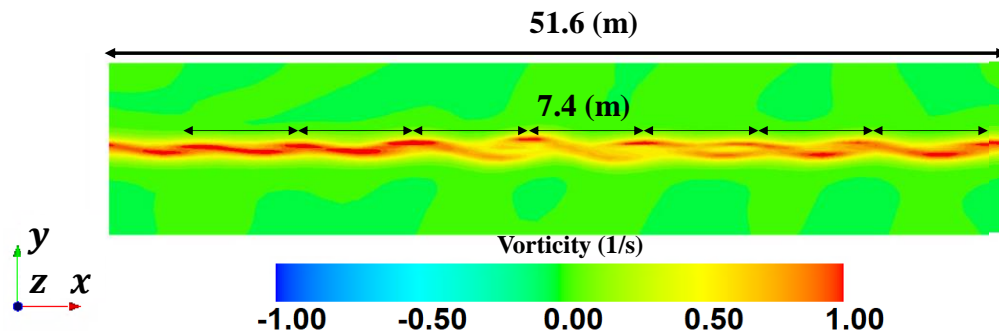


Figure A.3.5: Spanwise vorticity in x–y plane from simulation with Ri number = 0.25.